Rotational motion of externally driven anisotropic particles in complex fluids

齊藤, 圭太

PhD Dissertation

Rotational motion of externally driven anisotropic particles in complex fluids

KYUSHU
UNIVERSITY

Department of Physics, Kyushu University
SAITO Keita

February 29th, 2024

Abstract

Soft matter is a broad class of materials that are characterized by softness of their responses to external perturbation. Examples include colloids, polymers, liquid crystals and biological materials. A key character of soft matter is that its constituent units are large compared to the size of atoms and molecules. Due to this character, soft matter exhibits a large response to even small stimuli. Technological developments make it possible to fabricate self-propelled particles (active particles), which enable to locally drive soft matter. Since the motion of an active particle can be controlled by an external field, the active particle could control local force to drive soft matter into non-equilibrium. Active soft matter has the potential for novel materials. Further, the system is a simple model for understanding biological microswimmers because these swimmers swim in complex fluids such as polymer solutions or crowded environments. Although motion of active particles in complex fluids is a critical issue, researches on active particles in complex fluids and artificially activated complex fluids are limited. The purpose of this study is to systematically understand the motion of active particles in viscous or viscoelastic fluids. We used two types of active particles to achieve this purpose: rotating particles and translating particles.

Optically driven LC droplets are used as rotating particles because their fabrication and size control are easy. Efficient driving is important because viscosity of complex fluids is relatively high. The driving mechanism and its energy efficiency are investigated using nematic liquid crystal (NLC) and cholesteric LC (ChLC) droplets. For NLC droplets, waveplate effect and the light-scattering process are the main contributions to their rotation. In the case of ChLC droplets, transmissions and Bragg reflections due to the helical structure co-occur. Therefore, light angular momentum is transferred to the ChLC droplet via waveplate effect and Bragg reflection. An NLC droplet with bipolar structure has the highest energy transfer efficiency among droplets studied in our work.

Next, the rotational frequency of the droplet and the flow field around the droplet are studied using the efficient droplets (bipolar droplets). In water, the flow field induced by the droplet rotation is in good agreement with the theoretical flow where solid-particle and no-slip boundary conditions are assumed. However, the induced flow velocity in the viscous glycerol solution is lower than the theoretical value. This

suggests that the above assumptions (the solid particle and no-slip boundary conditions) may have been violated. We tested whether the fluidization effect or slip at the droplet surface is dominant. The results indicated that the slip at the droplet surface is the major contribution to the reduction of the induced flow field. We considered the alignment of LC molecules at the droplet surface or intermolecular interactions at the interface affect the slip. As an application of the droplets, we construct a micro-viscometer. Subsequently, the hydrodynamic interaction between two rotating droplets in viscous fluids is studied.

A Janus particle is used as a translating particle because its motion can be controlled by an external field and its orientation is detectable due to the asymmetric visualization. The motion of an electrically driven Janus particle has been studied in semidilute polymer solutions. At small self-propulsion velocity, the rotation of the Janus particle was diffusive, and its rotational diffusion coefficient increased as the velocity increased. The Janus particle with velocity above a critical velocity exhibited a circular orbit, and its angular frequency increased as the velocity increased. Since the rotation was always diffusive regardless of the velocity in water, the enhancement of the rotation was due to the viscoelastic properties of the solution. Our experimental observation can be explained by time-delayed elastic force, which is due to viscoelastic property of polymer solution. Further, two characteristic time scales are important for the transition to rotational motion: the relaxation time of the polymer network and the timescale of the Janus particle motion.

Finally, we summarize our own study and discuss future perspectives for motion of active particles in complex fluids. Our findings will inspire the investigation into transport phenomena induced by active particles in complex fluids.

Contents

Chapter 1

Introducrion

1.1 Soft matter and active particles

Soft matter is a broad class of materials that are characterized by softness of their responses to the external perturbation [1]. Examples include a wide range of materials such as colloids, polymers, liquid crystals and biological materials [2] as shown in Fig. 1.1. Elucidating and controlling the properties of soft matter is important not only for scientific but also for technological aspects. We will briefly introduce liquid crystals and polymers, which are closely related to this thesis.

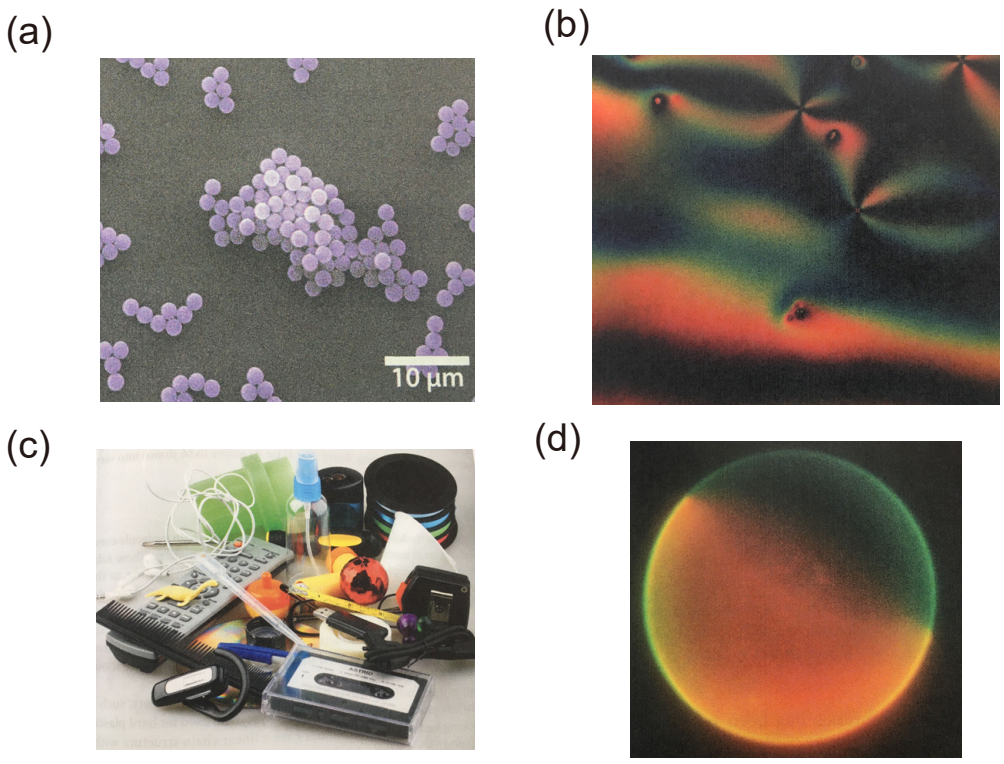

Figure 1.1. Examples of soft matter: (a) colloids, (b) liquid crystal, (c) products made of polymers and (d) a vesicle composed of a single bilayer. THe images were adapted from [2].

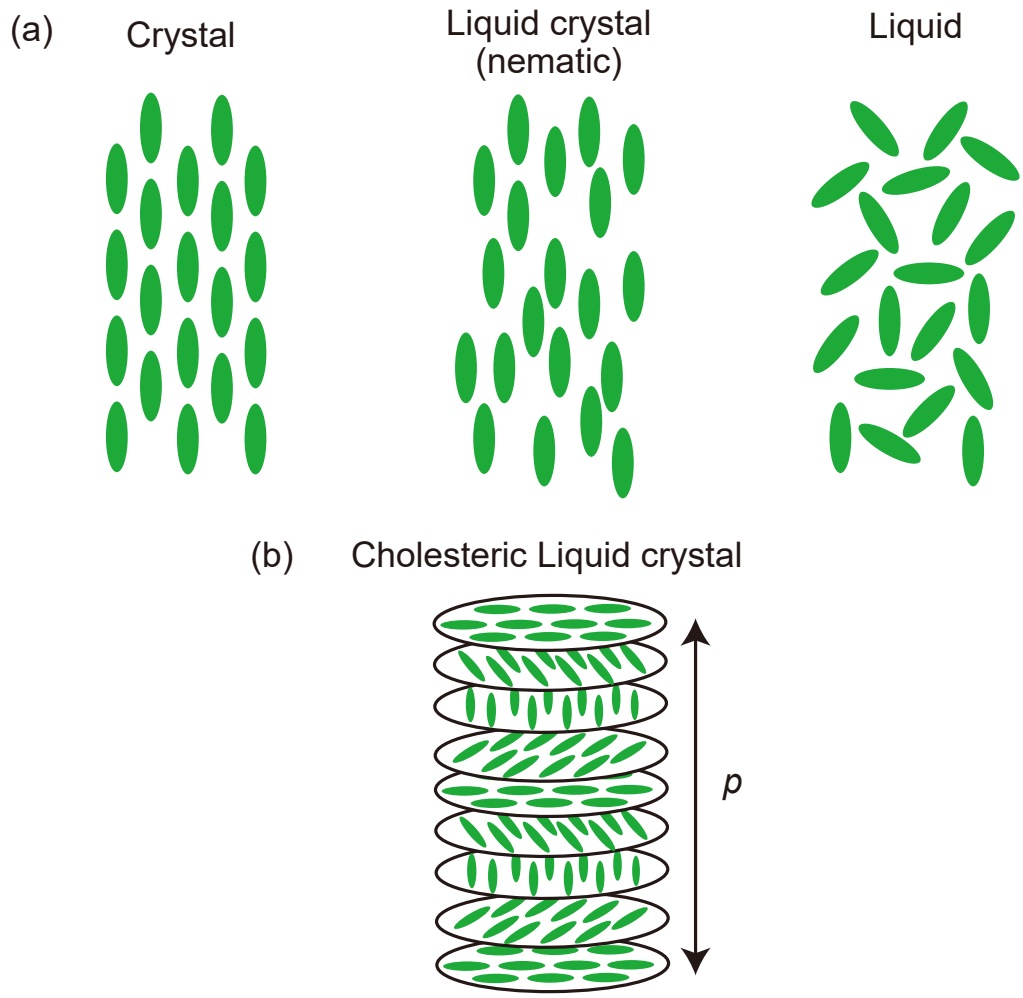

Figure 1.2. Phases of a liquid crystal (LC) material. (a) Schematic of crystalline (left), LC (middle) and liquid (right) phases. The illustrated LC phase is a nematic phase with orientational order and no long-range positional order. (b) Schematic of a cholesteric LC (ChLC) phase. p represents the pitch of ChLC.

1.2 Liquid crystal

Liquid crystal (LC) is an intermediate phase between crystalline and liquid phases. LC materials are usually composed of anisotropic (rod-like, disc-like, etc.) molecules. We consider the material composed of rod-shaped molecules. When the molecules

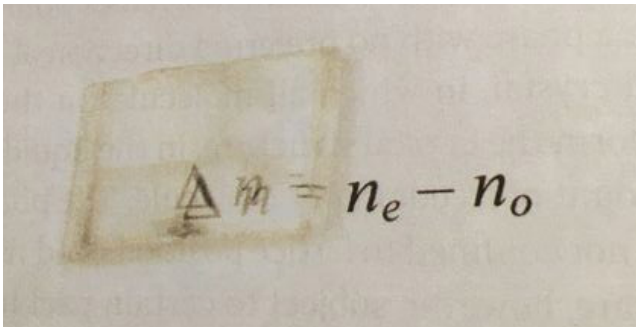

Figure 1.3. Double refraction in a calcite crystal due to birefringence. The image was adapted from [2]

align regularly on their positions and orient in the same direction, this phase is called crystalline phase as shown in the left side of Fig. 1.2(a). On the other hand, when the position and orientation of the molecules are random as shown in the right side of Fig. 1.2(a), the phase is called liquid phase. An LC phase exists between crystalline and liquid phase as shown in the middle of Fig. 1.2(a). There are various LC phases, which are characterized by order and symmetry of LC molecules. Typical LC phase is nematic phase, where the LC molecules in bulk have preferred direction of orientation but no positional order, corresponding to the middle of Fig. 1.2(a). Cholesteric liquid crystal (ChLC), also known as a chiral nematic liquid crystal, is an LC phase characterized by a helical structure with pitch p as shown in Fig. 1.2(b).

The orientational order gives the LC materials dielectric and optical anisotropies. Due to the anisotropy, the optical path length inside an LC material depends on the oscillatory direction of an electric field. Consequently, the refractive index depends on the direction of the oscillation. This property is known as birefringence as shown in Fig. 1.3. Further, a ChLC material has ability to selectively reflect circularly polarized light due to the helical structure, and p determines wavelength of the reflected light (Bragg reflection).

Since dielectric anisotropy enable the control of the orientation of LC molecules, the optical properties of the LC material can be controlled by the electric field. This property is used for electro-optic devices such as liquid-crystal displays [2].

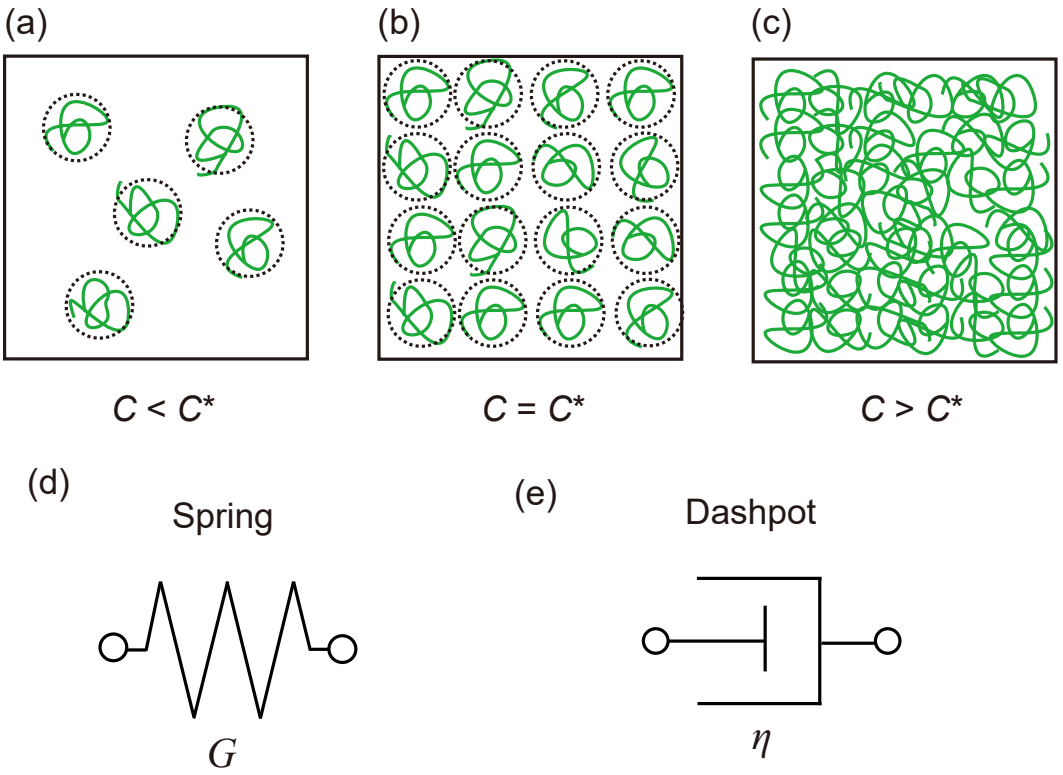

Figure 1.4. Polymer solutions and their mechanical models. (a, b, c) Polymer solutions in (a) the dilute $c < c^*$, (b) the overlap $c = c^*$ and (c) semidilute $c > c^*$ concentration. (d, e) Basic model for mechanical response of polymer solutions: (d) spring and (e) dashpot.

1.3 Polymer

A polymer is a long-chain molecule composed of a large number of repeated subunits called a monomer. The conformation of a polymer dispersed in good solvent can be considered as a globule (globule approximation). Mechanical property of a polymer solution depends on the polymer concentration c [2, 3]. In a dilute polymer solution, the individual polymer molecules do not interact with each other as shown in Fig. 1.4(a). The polymer solution behaves as viscous fluids. Polymers start to overlap spatially over $c = c^*$, and they entangle and form networks at $c > nc^*$ $(5 < n < 10)$ as shown in Figs. 1.4(b) and (c). c^* is called the overlap concentration. Due to the entangled network, the polymer solution at $c > nc^*$ $(5 < n < 10)$ has viscoelastic property. Mechanical response of the solution can be expressed by combinations of

spring and dashpot elements where the spring and dashpot describe elastic and viscous responses, respectively, as shown in Figs. 1.4(d) and (e). For the elastic body, the relationship between the stress σ and the strain γ is described by the Hooke's law,

$$\sigma = G\gamma, \tag{1.1}$$

where G is the elastic constant. For Newtonian fluids, the relationship between σ and γ is expressed by the Newton's law,

$$\sigma = \eta \frac{d\gamma}{dt}, \tag{1.2}$$

where η is the viscosity of the solution.

The Maxwell model is a simple viscoelastic model composed of a series of dashpot and spring, which has an elastic modulus at short time and viscous relaxation at long times [4]. Such behavior can be observed in chemically and physically uncrosslinked polymer solution exhibiting linear viscoelasticity [5]. On the other hand, semidilute polymer solution follows a Jeffrey fluid model. The Jeffrey model is composed of a series of dashpot and Kelvin-Voigt element (elastic spring in parallel with viscous dashpot). The Jeffrey model describes creep mechanisms during constant stress and viscous relaxation [5].

1.4 Characteristics of soft matter

A key characteristic of soft matter is that its constituent unit is large compared to the size of an atom and a molecule. Polymer is composed of thousands or millions of atoms. Although LC molecules are not large, LC molecules collectively move as a group when an external field is applied. Due to this characteristic, soft matter exhibits a large response to even small stimuli. In solid materials, applied force is proportional to strain of the material, but in soft materials such as rubber, the relationship between applied force and resulting strain is often non-linear. This indicates that the response to small forces play an important role in properties of soft matter. Indeed, localized non-thermal force induced by biomolecules affects viscosity in a cell [6]. The viscosity in a living cell becomes lower compared with that of the cell extract. This phenomenon indicates that localized non-thermal force is critical for the properties of active soft matter. Control of the non-thermal force is important to understand its effect.

1.5 Self-propelled particle

Technological developments in microfabrication and micromanipulation have enabled a wide range of experiments on the microscale. This development makes it possible to fabricate self-propelled particles (active particles). An active micro particle is a microscopic entity that has the ability to take energy from its environment and drive itself. There are several active particles such as Janus particles [1, 10], Marangoni droplets [11, 12], Quincke rollers [13] and birefringence objects [9, 14] as shown in Figs. 1.5(a)-(d). Since the motion of the active particle can be controlled by an external field, the active particle could be controllable local force. We briefly explain representative active particles: Janus particles, Marangoni droplets, Quincke rollers and birefringent particles.

Janus particle

A Janus particle is usually a microscopic particle with two different hemispheres or regions [1, 10]. The term "Janus" refers to the Roman god with two faces, symbolizing duality. There are many combinations of surface materials ranging from metal (e.g., Pt, Cr, Au) to dielectric (e.g., silica and polystyrene) [10]. Since the driving

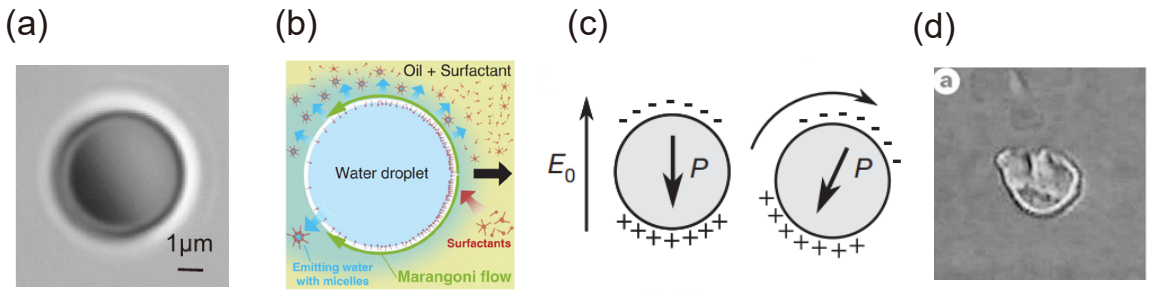

Figure 1.5. Self-propelled particles. (a) The microscopic image of the Janus particle: the half-coated silica particle with chromium. (b) Schematic of a Marangoni droplet: the water droplet in the surfactant solution [7]. (c) Schematic of Quincke rollers: the poly(methyl methacrylate) colloid dispersed in an AOT/hexadecane solution under a DC electric field E_0 [8]. Surrounding ions induce antiparallel polarization P to E_0. (d) The birefringent particle: calcite trapped by circularly polarized light [9].

mechanism of a Janus particle depends on the material combination, we can choose a suitable driving method according to the situation. In many cases, its translational motion can be controlled. The driving methods are explained in Section 3.2.

Marangoni droplet

A Marangoni droplet is a moving droplet due to Marangoni effect, where the droplet is usually immersed in a surfactant solution [11, 12]. Marangoni effect refers to a phenomenon in fluids where a gradient of surface tension induces flow. Asymmetric adsorption of surfactant molecules induces a gradient of surface tension. Dissolution of molecules inside the droplet induces depletion of empty micelles at the rear side of the droplet as shown in Fig. 1.5(b). Due to the depletion, the gradient of the surfactant molecules along the droplet is maintained, and the droplets self-propel. Velocity of the droplet depends on its size and concentration of surfactant [11, 12]. Further, an LC droplet also exhibits self-propulsion, and the droplet shows various motion (random, helical, straight and Brownian motion) depending on its size and phase [15].

Quincke roller

A Quincke roller is a dielectric rolling colloid driven by an electric field [13, 16]. A dielectric colloid is immersed in a conducting fluid where the relaxation time of ions is slower than that of the polarization of the colloid. When an electric field is applied, the colloid is polarized at first, and consequently, the surrounding ions are attracted to the surface of the polarized colloid. This results in antiparallel polarization as shown in Fig. 1.5(c). This configuration is unstable, and small perturbation induces rotation of the colloid, which is called Quincke effect. Above a certain threshold voltage, the continuous rotation maintains. When the colloid settles to the bottom, its rotation leads to translational motion, and the velocity can be controlled by an applied electric field [16].

Birefringent particle

There are several birefringent objects such as vaterite, calcite and LC droplets. In a birefringent particle, optical path length inside the particle depends on the oscillation direction of an electric field. Polarization of light changes by passing through the

birefringent particle. Since polarization of light relates to the angular momentum, the change of the polarization induces the transfer of angular momentum to the object. The mechanism of the rotaion is explainde in Section 3.2.

1.6 Active particles in soft matter

Active particles enable the local driving of soft matter. This system has the potential for novel materials. Furthermore, the system is a model system for understanding biological microswimmers such as bacteria and microorganisms because these swimmers swim in complex fluids such as polymer solutions or crowded environments. From the above perspective, it is important to understand the behavior of active particles in complex fluids. Some researches on active particles in complex fluids report characteristic motion in dense binary colloidal suspensions[17] and semidilute polymer solutions [18].

Dense binary colloidal suspensions

J. R. Gomez, *et al.* [17] found enhancement of rotational diffusion coefficient of an active particle (Janus particle) in dense binary inactive colloidal suspensions. Figures 1.6(a), (b) and (c) show the trajectories of a Janus particle (blue lines) and its instantaneous orientation (red arrows). In Figs. 1.6(a) and (b), the area fraction of the particle φ is the same, but propulsion velocity v is different (a: $\varphi = 0.730$ and $v = 0$ µm/s, b: $\varphi = 0.730$ and $v = 1.0$ µm/s). Particle orientation in Fig. 1.6(b) frequently changes compared with that in Fig. 1.6(a), which indicates that translational motion promotes rotation of the particle. This trend is confirmed in mean-squared angular displacement $\langle \Delta\theta^2 \rangle$ of the particle as shown in Fig. 1.6(d) and (e). $\langle \Delta\theta^2 \rangle$ for the active particle with $v \neq 0$ (Fig. 1.6(d)) is greater than that for a passive particle with $v = 0$ (Fig. 1.6(e)) in each φ. On the other hand, in Figs. 1.6(b) and (c), only φ is different (b: $\varphi = 0.730$, c: $\varphi = 0.776$). The active particle in Fig. 1.6(c) rotates more intensely than the particle in Fig. 1.6(b). Increasing φ promotes rotational motion as long as φ does not exceed the glass transition point as shown in Fig. 1.6(d). The origin of the rotation is explained as the phenomenological model; Translational motion of the active particle perturbs the surrounding fluid. When the relaxation time of the perturbation field is longer or comparable with the timescale of the ac-

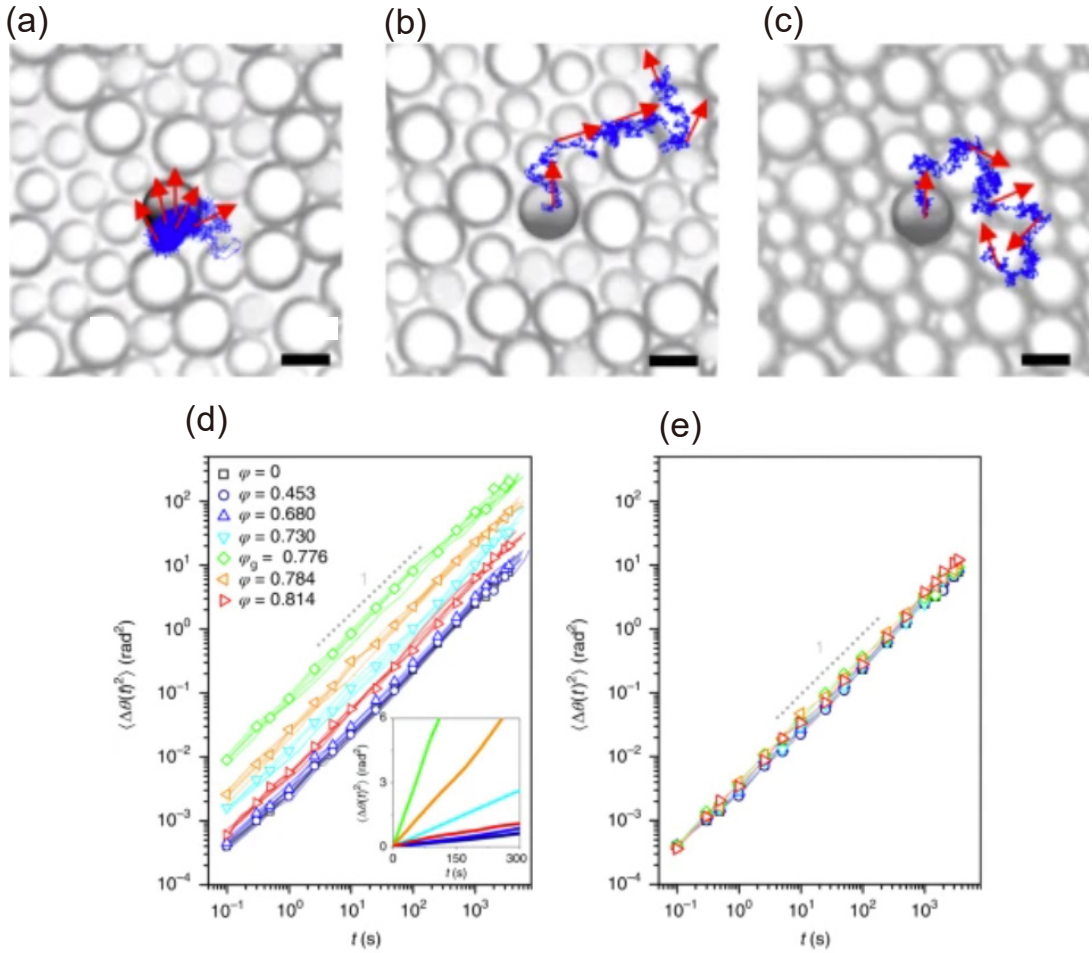

Figure 1.6. Rotation of a Janus particle in dense binary colloidal suspension [17]. (a-c) Trajectories for 500 s with positions and orientations indicated as blue lines and red arrows for different area fraction of colloids φ: (a) $\varphi = 0.730$, $v = 0$ µm/s, (b) $\varphi = 0.730$, $v = 1.0$ µm/s and (c) $\varphi = 0.776$, $v = 0$ µm/s. (d, e) Mean square angular displacement $< \Delta\theta^2 >$ of the active (d) and passive (e) Janus particles at different φ.

tive particle motion, the active particle interacts with the flow field perturbated by itself. Due to the interaction, the rotational motion becomes enhanced. Increasing φ and v correspond to increasing the relaxation time and strength of the perturbation, respectively.

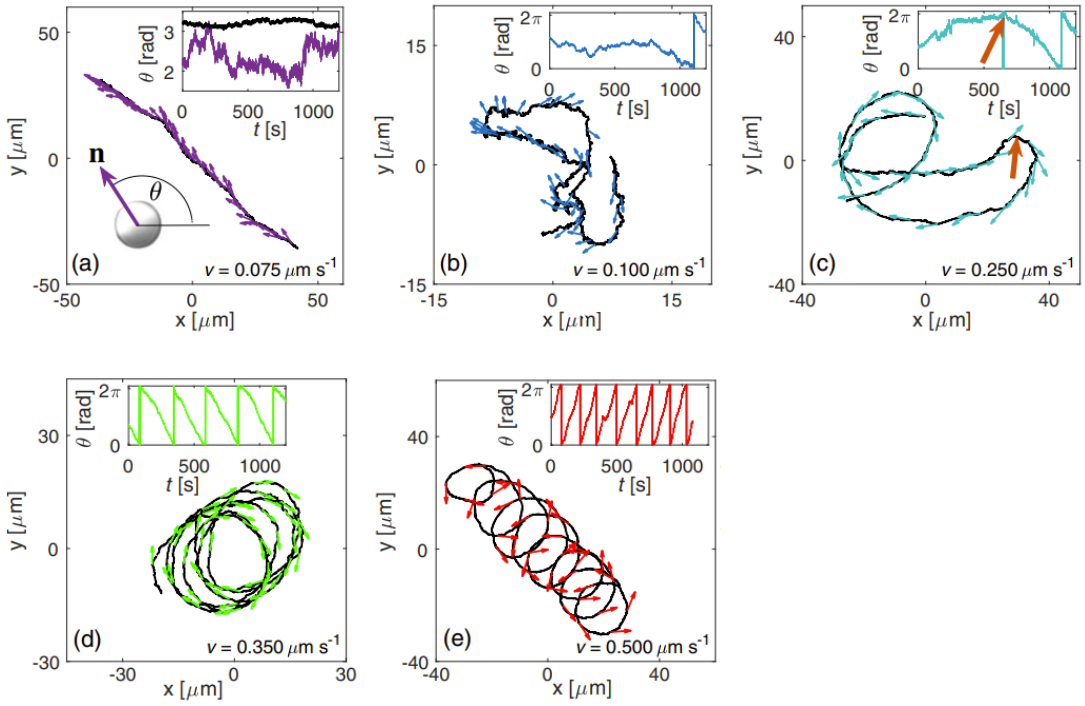

Figure 1.7. Trajectories of a Janus particle in polymer solution at different propulsion velocity v: (a) $v = 0.075$ μm/s, (b) $v = 0.100$ μm/s, (c) $v = 0.250$ μm/s, (d) $v = 0.350$ μm/s, (e) $v = 0.500$ μm/s. An inset represents the time evolution of θ defined in the image attached in (a). The colored arrows on the trajectories represent the instantaneous direction of the Janus particle. Images were adapted from [18].

Semidilute polymer solutions

Similar behavior is reported in semidilute polymer solutions [18]. Figures 1.7(a)-(e) show the trajectories (black lines) and their instantaneous orientation (colored arrows) in different propulsion velocity v. At small v (corresponding to Figs. 1.7(a)-(c)), the rotational motion is diffusive. On the other hand, the particle with v above a threshold velocity exhibits a circular motion as shown in Figs. 1.7(d) and (e). The rotational motion of the active particle is enhanced as v increases. A time-delayed restoring force from the polymer solution induces misalignment between the restoring and the propulsive forces and generates torque [18].

1.6.1 Rotation of active particles

The above examples indicate that rotation plays an important role in motion of active particles in viscoelastic fluids and crowded environments. In research on active particles in complex fluids, the translational motion is mainly controlled to understand their motion. Control of not only translation but also rotation is important for systematic understanding. Further, control of rotational motion in complex fluids leads to control of microscale flow or measurement of local properties of soft matter.

Chapter 2

Hydrodynamic theory

Motion of active particles is related to hydrodynamics. In this section, flow fields are briefly discussed by using the Navier-Stokes equation and the conservation equation for mass. The Navier-Stokes equation is a governing equation of fluid. Since our interest is focused on microscale phenomena, the behavior of microscale flow is also described.

2.1 Equation of continuity

The differential equation for conservation of mass is written as

$$\frac{\partial \rho}{\partial t} + \nabla \cdot (\rho \boldsymbol{v}) = 0, \tag{2.1}$$

where $\rho(\boldsymbol{r}, t)$ is the fluid density and $\boldsymbol{v}(\boldsymbol{r}, t)$ is the Eulerian velocity. These variables depend on time t and the position $\boldsymbol{r}$ which is fixed with respect to the laboratory frame. The first term on the left-hand side of Eq. (2.1) represents the change in density with respect to time. The second term on the left-hand side means the entering or leaving mass through the boundary of the unit volume. The conservation of mass means the change in density arises from the entering and leaving mass. If ρ does not depend on t and $\boldsymbol{r}$ (incompressibility, $\rho(\boldsymbol{r}, t) = \text{const.}$), Eq. (2.1) reduces to the following equation,

$$\nabla \cdot \boldsymbol{v} = 0. \tag{2.2}$$

The density of fluids generally depends on temperature. Since the system of our interest is in isothermal condition, the above assumption (incompressibility: $\rho(\boldsymbol{r}, t) = \text{const.}$) is acceptable.

2.2 Equation of motion for fluids

Navier-Stokes equation is expressed as

$$\rho \left[\frac{\partial \boldsymbol{v}}{\partial t} + (\boldsymbol{v} \cdot \nabla) \boldsymbol{v} \right] = -\nabla p + \eta \nabla^2 \boldsymbol{v}, \tag{2.3}$$

where p is the pressure and η is the viscosity of the fluid. The Navier-Stokes equation corresponds to Newton's second law of motion for fluid per unit volume. The left-hand side of Eq. (2.3) corresponds to inertia term. $-\nabla p$ and $\eta\nabla^2\boldsymbol{v}$ on the right-hand side of Eq. (2.3) represent pressure and viscous force, respectively.

2.2.1 Inertia term

The left-hand side of Eq. (2.3) corresponds to the material derivative. An acceleration $\boldsymbol{a}$ is generally described by

$$\boldsymbol{a} = \lim_{\Delta t\to 0} \frac{\boldsymbol{v}(\boldsymbol{r}+\boldsymbol{v}\Delta t, t+\Delta t) - \boldsymbol{v}(\boldsymbol{r}, t)}{\Delta t}. \tag{2.4}$$

We consider the x compornent of $\boldsymbol{a} = (a_x, a_y, a_z)$. a_x is written as

$$\begin{aligned} a_x &= \lim_{\Delta t\to 0} \frac{1}{\Delta t}\left(v_x(x+v_x\Delta t, y+v_y\Delta t, z+v_z\Delta t, t+\Delta t) - v_x(x,y,z,t)\right) \\ &= \lim_{\Delta t\to 0} \frac{1}{\Delta t}\left(v_x\Delta t\frac{\partial v_x}{\partial x} + v_y\Delta t\frac{\partial v_x}{\partial y} + v_z\Delta t\frac{\partial v_x}{\partial z} + \Delta t\frac{\partial v_x}{\partial t} + \mathcal{O}(\Delta t^2)\right) \\ &= v_x\frac{\partial v_x}{\partial x} + v_y\frac{\partial v_x}{\partial y} + v_z\frac{\partial v_x}{\partial z} + \frac{\partial v_x}{\partial t} = (\boldsymbol{v}\cdot\nabla)v_x + \frac{\partial v_x}{\partial t}. \end{aligned} \tag{2.5}$$

Similar expressions can be obtained for a_x and a_y, and $\boldsymbol{a} = \frac{\partial \boldsymbol{v}}{\partial t} + (\boldsymbol{v}\cdot\nabla)\,\boldsymbol{v}$. Multiplying ρ to $\boldsymbol{a}$ gives the inertia term per unit volume, $\rho\boldsymbol{a} = \rho\left[\frac{\partial \boldsymbol{v}}{\partial t} + (\boldsymbol{v}\cdot\nabla)\,\boldsymbol{v}\right]$. This is the same expression as the left-hand side of Eq. (2.3).

2.2.2 Pressure term

The first term on the right-hand side of Eq. (2.3) corresponds to the force caused by pressure p on unit volume of fluids. We consider the force acting on a plane perpendicular to the x-axis, F_x, as shown in Fig. 2.1. F_x is described as

$$F_x = \left[p\left(x - \frac{dx}{2}, y, z\right) - p\left(x + \frac{dx}{2}, y, z\right)\right] dydz. \tag{2.6}$$

p is expanded to the first order of dx and Eq. (2.6) is rewritten as

$$F_x = \left[-\frac{dx}{2}\frac{\partial p(x,y,z)}{\partial x} - \frac{dx}{2}\frac{\partial p(x,y,z)}{\partial x}\right] dydz = -\frac{\partial p(x,y,z)}{\partial x} dxdydz. \tag{2.7}$$

The force per unit volume is $\frac{F_x}{dxdydz} = -\frac{\partial p}{\partial x}$. y and z components of the force are also obtained as $-\frac{\partial p}{\partial y}$ and $-\frac{\partial p}{\partial z}$, respectively. The force caused by p is expressed as

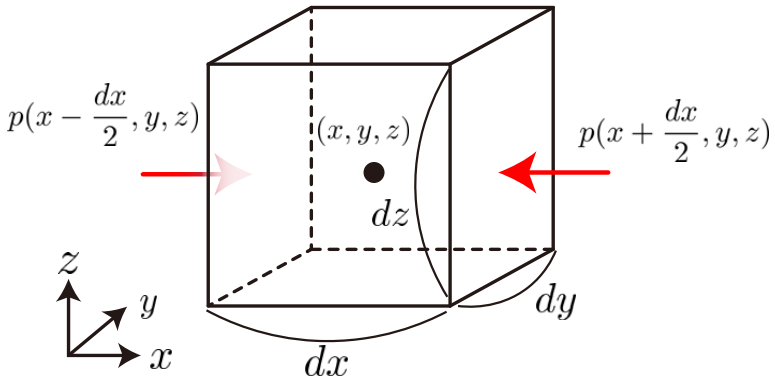

Figure 2.1. Schematic of pressure on unit volume of fluids in x direction.

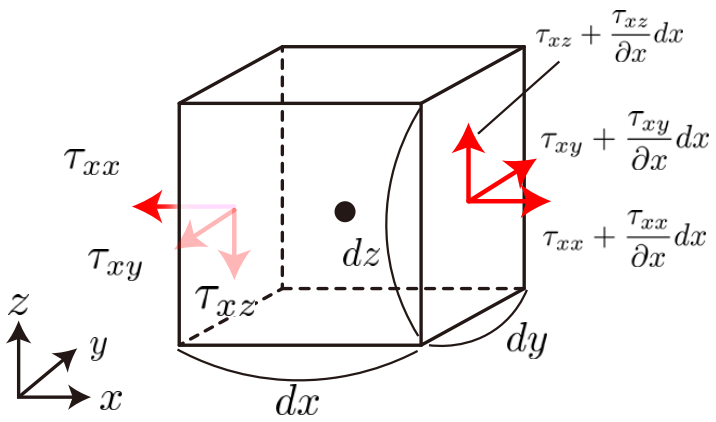

Figure 2.2. Schematic of viscous stress on unit volume of fluids.

$-\left(\frac{\partial p}{\partial x}, \frac{\partial p}{\partial y}, \frac{\partial p}{\partial z}\right) = -\nabla p$. This is the same expression as the first term on the right-hand side of Eq. (2.3).

2.2.3 Viscosity term

The second term on the right-hand side of Eq. (2.3) corresponds to force due to viscous stress τ_{ij} on unit volume where the first index i represents the plane subjected to the stress (perpendicular to i-direction), and the second index j represents the

direction of the stress. Viscous stress τ_{ij} is expressed as

$$\tau_{ij} = \eta \left(\frac{\partial v_i}{\partial r_j} + \frac{\partial v_j}{\partial r_i} \right), \tag{2.8}$$

where $i \neq j$. We consider the viscous stress in the x-direction per unit volume as shown in Fig. 2.2. Total force in the x-direction is written as

$$\frac{\partial \tau_{xx}}{\partial x} dxdydz + \frac{\partial \tau_{yx}}{\partial y} dydxdz + \frac{\partial \tau_{zx}}{\partial z} dzdxdy. \tag{2.9}$$

Total force per unit volue is

$$\frac{\partial \tau_{xx}}{\partial x} + \frac{\partial \tau_{yx}}{\partial y} + \frac{\partial \tau_{zx}}{\partial z}. \tag{2.10}$$

Substituing Eq. (2.8) into Eq. (2.10) gives

$$\begin{aligned}
&\eta \frac{\partial}{\partial x} \left(\frac{\partial v_x}{\partial x} + \frac{\partial v_x}{\partial x} \right) + \eta \frac{\partial}{\partial y} \left(\frac{\partial v_x}{\partial y} + \frac{\partial v_y}{\partial x} \right) + \eta \frac{\partial}{\partial z} \left(\frac{\partial v_z}{\partial x} + \frac{\partial v_x}{\partial z} \right) \\
&= \eta \left(\frac{\partial^2 v_x}{\partial x^2} + \frac{\partial^2 v_x}{\partial y^2} + \frac{\partial^2 v_x}{\partial z^2} \right) + \eta \frac{\partial}{\partial x} \left(\frac{\partial v_x}{\partial x} + \frac{\partial v_y}{\partial y} + \frac{\partial v_z}{\partial z} \right) \\
&= \eta \nabla^2 v_x + \eta \frac{\partial}{\partial x} \nabla \cdot v = \eta \nabla^2 v_x,
\end{aligned} \tag{2.11}$$

where $\nabla \cdot v = 0$ by Eq. (2.2). y and z components of viscous force are also expressed as $\eta \nabla^2 v_y$ and $\eta \nabla^2 v_z$, respectively. Therefore, the pressure term is written as $\eta \nabla^2 \boldsymbol{v}$.

2.3 Stokes Equations

Navier-Stokes equation can be non-dimensionalized with typical velocity U and length L as

$$\frac{\partial \boldsymbol{v}^*}{\partial t^*} + (\boldsymbol{v}^* \cdot \nabla^*) \boldsymbol{v}^* = \frac{1}{Re} \left(-\nabla^* p^* + \nabla^{*2} \boldsymbol{v}^* \right), \tag{2.12}$$

where dimensionless variables are marked with a superscript * ($t^* = \frac{t}{L/U}$, $p^* = \frac{p}{\eta U/L}$, $v^* = \frac{v}{U}$ and $\nabla^* = \frac{\nabla}{1/L}$). Re in the right-hand side of Eq. (2.12) is known as the Reynolds number Re,

$$Re = \frac{\rho U L}{\eta}. \tag{2.13}$$

The Reynolds number means the ratio of the inertia term to viscous term. If $Re \ll 1$, the inertia term of the Navier-Stokes equation is negligible, and the Navier-Stokes equation reduces to the Stokes equation,

$$\nabla p = \eta \nabla^2 \boldsymbol{v}. \tag{2.14}$$

In the systems we used, $L \sim 10$ µm, $U \sim 10$ µm/s, $\eta \sim 10^{-3}$ Pa·s and $\rho \sim 1000$ kg/m^3, and thus $Re \sim 10^{-4}$ and the inertia term can be negligible. The Stokes equation is applicable in microscale flow.

2.4 Stokes flow around a sphere

We consider flow fields around a translating or rotating particle with the Stokes equation.

2.4.1 Translation of a particle

We consider a moving sphere at a constant velocity U in the z-direction. It is convenient to choose a reference frame where the sphere with radius a is stationary and the fluid far from the sphere is moving with a uniform velocity, $\boldsymbol{v} = U\boldsymbol{e}_z$ as shown in Fig. 2.3. In the polar coordinate system, the continuity equation Eq. (2.2) is written as

$$\nabla \cdot \boldsymbol{v} = \frac{1}{r^2}\frac{\partial}{\partial r}\left(r^2 v_r\right) + \frac{1}{r\sin\theta}\frac{\partial}{\partial \theta}(v_\theta \sin\theta) = 0, \tag{2.15}$$

where we assume $v_\phi = 0$ and $\frac{\partial}{\partial \phi} = 0$ due to symmetry of the flow field. Stream function Ψ is introduced satisfying the following equations:

$$v_r = \frac{1}{r^2\sin\theta}\frac{\partial \Psi}{\partial \theta}, \tag{2.16}$$

$$v_\theta = -\frac{1}{r\sin\theta}\frac{\partial \Psi}{\partial r}, \tag{2.17}$$

where Eqs. (2.16) and (2.17) satisfy Eq. (2.15). $\boldsymbol{v}$ can be also written as a following expression, using ∇ and Ψ,

$$\boldsymbol{v} = \nabla \times \left(\frac{\Psi}{r\sin\theta}\boldsymbol{e}_{\boldsymbol{\phi}}\right), \tag{2.18}$$

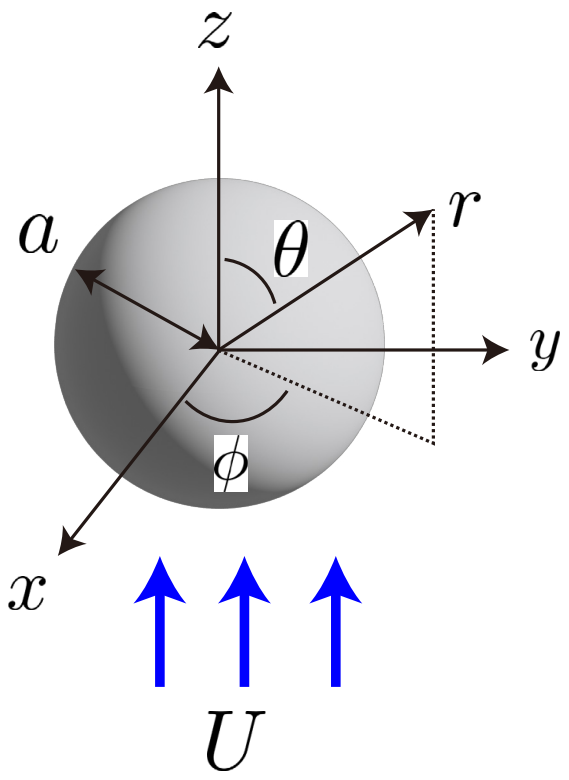

Figure 2.3. Schematic of a sphere (radius a) in a flow field with uniform velocity $U\boldsymbol{e}_z$.

because $\nabla \times \boldsymbol{A}$ in the polar coordinate system is expressed as

$$(\nabla \times \boldsymbol{A})_r = \frac{1}{r\sin\theta}\left[\frac{\partial}{\partial\theta}(\sin\theta A_\phi) - \frac{\partial A_\theta}{\partial\phi}\right] \tag{2.19}$$

$$(\nabla \times \boldsymbol{A})_\theta = \frac{1}{r}\left[\frac{1}{\sin\theta}\frac{\partial A_r}{\partial\phi} - \frac{\partial}{\partial r}(rA_\phi)\right]. \tag{2.20}$$

Multiplying both sides of Eq. (2.14) by ∇ gives

$$\nabla \times \nabla^2 \boldsymbol{v} = 0$$

$$\nabla \times \nabla^2 \left[\nabla \times \left(\frac{\Psi}{r\sin\theta}\boldsymbol{e}_\phi\right)\right] = 0, \tag{2.21}$$

where $\nabla \times \nabla p = 0$ and Eq. (2.18) are used. Finally, Eq. (2.21) reduces to

$$\left[\frac{\partial^2}{\partial r^2} + \frac{\sin\theta}{r^2}\frac{\partial}{\partial\theta}\left(\frac{1}{\sin\theta}\frac{\partial}{\partial\theta}\right)\right]^2 \Psi = 0. \tag{2.22}$$

$\boldsymbol{v} = U\boldsymbol{e}_z$ at $r \to \infty$ gives

$$v_r(r=\infty) = U\cos\theta = \frac{1}{r^2\sin\theta}\frac{\partial\Psi}{\partial\theta}, \tag{2.23}$$

$$v_\theta(r=\infty) = -U\sin\theta = -\frac{1}{\sin\theta}\frac{\partial\Psi}{\partial r}. \tag{2.24}$$

From the above two equations, $\Psi \to \frac{U}{2}r^2\sin^2\theta$ at $r \to \infty$. We assume $\Psi = f(r)\sin^2\theta$, and substituting Ψ into Eq. (2.22) gives

$$\left[\frac{\partial^2}{\partial r^2} - \frac{2}{r^2}\right]^2 f(r) = 0. \tag{2.25}$$

Assuming $f(r) = r^n$, Eq. (2.25) reduces to

$$(n+1)(n-1)(n-2)(n-4) = 0. \tag{2.26}$$

Therefore,

$$\Psi = \sin^2\theta\left(\frac{A}{r} + Br + Cr^2 + Dr^4\right), \tag{2.27}$$

where A, B, C and D are constants determined by the boundary conditions. Since $\Psi \to \frac{U}{2}r^2\sin^2\theta$ at $r \to \infty$, $D = 0$ and $C = U/2$. Eqs. (2.16) and (2.17) are expressed as

$$v_r = \cos\theta\left(2Ar^{-3} + 2B^{-1} + U\right), \tag{2.28}$$

$$v_\theta = -\sin\theta\left(-Ar^{-3} + B^{-1} + U\right). \tag{2.29}$$

No-slip boundary condition ($v_r(r=a) = 0$ and $v_\theta(r=a) = 0$) gives $A = \frac{1}{4}Ua^3$ and $B = -\frac{3}{4}Ua$. v_r and v_θ are written as

$$v_r = U\cos\theta\left(1 + \frac{a^3}{2r^3} - \frac{3a}{2r}\right), \tag{2.30}$$

$$v_\theta = -U\sin\theta\left(1 - \frac{a^3}{4r^3} - \frac{3a}{4r}\right). \tag{2.31}$$

Next, we consider pressure and viscous stress acting on the sphere. The pressure can be calculated from r component of the Stokes equation as

$$\frac{\partial p}{\partial r} = \eta(\nabla^2\boldsymbol{v})\boldsymbol{e}_r = \frac{3\eta UR}{r^3}\cos\theta. \tag{2.32}$$

The pressure is expressed as

$$p(r) = \int_r^\infty \frac{\partial p}{\partial r} dr = p_\infty - \frac{3\eta U r}{2r^2} \cos\theta, \tag{2.33}$$

where p_∞ represents the pressure at $r = \infty$ and is constant. The force acting on the sphere arising from the pressure in z direction F_p is

$$\begin{aligned} F_p &= \int_0^\pi \int_0^{2\pi} \left[\frac{3\eta U a}{2r^2} \cos^2\theta - p_\infty \cos\theta \right] a^2 \sin\theta d\phi d\theta \\ &= \left[-\eta\pi U a \cos^3\theta \right]_0^\pi \\ &= 2\pi\eta U a. \end{aligned} \tag{2.34}$$

On the other hand, since the sphere experiences the viscous stress via its surface, we consider τ_{rr} and $\tau_{r\theta}$ ($\tau_{r\phi} = 0$ because $v_\phi = 0$),

$$\tau_{rr} = \eta \left[\frac{\partial v_r}{\partial r} \right]_{r=a} = 0, \tag{2.35}$$

$$\begin{aligned} \tau_{r\theta} &= \eta \left[r \frac{\partial}{\partial r} \left(\frac{v_\theta}{r} \right) + \frac{1}{r} \frac{\partial v_r}{\partial \theta} \right]_{r=a} \\ &= -\frac{3}{2} \eta U \sin\theta \left[\frac{a^3}{r^4} \right]_{r=a} \\ &= -\frac{3\eta U}{2a} \sin\theta. \end{aligned} \tag{2.36}$$

The sum of the z component of the viscous stress F_η is given by

$$\begin{aligned} F_\eta &= \int_0^\pi \int_0^{2\pi} \left[\frac{3\eta U}{2a} \sin^2\theta \right] a^2 \sin\theta d\phi d\theta \\ &= 4\pi\eta U a. \end{aligned} \tag{2.37}$$

The force acting on the sphere F_v is written as

$$F_v = F_p + F_\eta = 6\pi\eta U a. \tag{2.38}$$

This is known as Stokes's law of resistance.

Translational motion of a droplet

In the case of a droplet, we consider flow velocity both inside $\boldsymbol{v}^i$ and outside $\boldsymbol{v}^o$ the droplet. The velocity outside a droplet v_r^o and v_θ^o are given by Eqs. (2.28) and (2.29),

which are expressed as

$$v_r^{\mathrm{o}} = \cos\theta \left(\frac{2A_1}{r^3} + \frac{2B_1}{r} + U \right), \tag{2.28}$$

$$v_\theta^{\mathrm{o}} = -\sin\theta \left(-\frac{A_1}{r^3} + \frac{B_1}{r} + U \right). \tag{2.29}$$

Inside the droplet, the general solution for Ψ is expressed by Eq. (2.27), which is expressed as

$$\Psi = \sin^2\theta \left(\frac{A_2}{r} + B_2 r + C_2 r^2 + D_2 r^4 \right). \tag{2.39}$$

v_r^{i} and v_θ^{i} are expressed using Eqs. (2.16) and (2.17),

$$v_r^{\mathrm{i}} = 2\cos\theta \left(\frac{A_2}{r^3} + \frac{B_2}{r} + C_2 + D_2 r^2 \right), \tag{2.40}$$

$$v_\theta^{\mathrm{i}} = -\sin\theta \left(-\frac{A_2}{r^3} + \frac{B_2}{r} + 2C_2 + 4D_2 r^2 \right). \tag{2.41}$$

Since v_r^{i} and v_θ^{i} do not diverge at $r \to 0$,

$$A_2 = B_2 = 0. \tag{2.42}$$

The velocity inside the droplet v_r^{i} and v_θ^{i} is written as

$$v_r^{\mathrm{i}} = \cos\theta \left(2C_2 + 2D_2 r^2 \right), \tag{2.43}$$

$$v_\theta^{\mathrm{i}} = -\sin\theta \left(2C_2 + 4D_2 r^2 \right). \tag{2.44}$$

The boundary conditions at $r = a$ are

1. $v_r^{\mathrm{o}} = 0$ (a kinematic condition),
2. $v_r^{\mathrm{i}} = 0$ (a kinematic condition),
3. v_θ is continuous (no-slip boundary condition),
4. $\tau_{r\theta}$ is continuous (tangential stress is continuous).

This leads to the following equations:

$$\frac{A_1}{a^3} + \frac{B_1}{a} = -\frac{U}{2}, \tag{2.45}$$

$$C_2 = -D_2 a^2, \tag{2.46}$$

$$-\frac{A_1}{a^3} + \frac{B_1}{a} + U = 2C_2 + 4D_2 a^2, \tag{2.47}$$

$$\frac{A_1}{a^4} = \lambda D_2 a, \tag{2.48}$$

where λ is the ratio of the inner viscosity of the droplet η_{i} to the outer viscosity η_{o}, $\lambda = \frac{\eta_{\mathrm{i}}}{\eta_{\mathrm{o}}}$. The following equations are obtained:

$$A_1 = \frac{\lambda}{4(\lambda+1)} U a^3, \quad B_1 = -\frac{3\lambda+2}{4(\lambda+1)} U a, \tag{2.49}$$

$$C_2 = \frac{1}{4(\lambda+1)} U, \quad D_2 = -\frac{1}{4(\lambda+1)} \frac{U}{a^2}. \tag{2.50}$$

The force F_z exerted by the fluid on the droplet is derived from the external field in the same way as for solid particles,

$$F_z = -6\pi\eta_o a U \frac{2+3\lambda}{3(1+\lambda)}. \tag{2.51}$$

If the sphere is rigid ($\lambda \to \infty$), $F_z \to -6\pi\eta_{\mathrm{o}} a U$ and we recover the Stokes law. If the sphere is a bubble ($\lambda \to 0$), we obtain $F_z \to -4\pi\eta_{\mathrm{o}} a U$.

2.4.2 Rotation of a particle

We consider a rotating sphere with an angular frequency ω around the z-direction as shown in Fig. 2.4. From the axisymmetric geometry, we assume that $v_r = 0$, $v_\theta = 0$ and no parameter depends on ϕ ($\frac{\partial}{\partial\phi} = 0$). The boundary condition (no-slip boundary condition) at $r = a$ for $\boldsymbol{v}$ is as follows,

$$v_r = 0, \ v_\theta = 0, \ v_\phi = a\omega \sin\theta. \tag{2.52}$$

Eq. (2.52) implies that v_ϕ is expressed as $v_\phi = f(r)\sin\theta$. We assume that p is constant throughout the fluid. The ϕ component of the Stokes equation gives

$$\frac{1}{r^2}\frac{\partial}{\partial r}\left(r^2 \frac{\partial v_\phi}{\partial r}\right) + \frac{1}{r^2 \sin\theta}\frac{\partial}{\partial\theta}\left(\sin\theta \frac{\partial v_\phi}{\partial\theta}\right) - \frac{v_\phi}{r^2\sin^2\theta} = 0. \tag{2.53}$$

Substituting $v_\phi = f(r)\sin\theta$ into Eq. (2.53) gives the following differential equation,

$$r^2 \frac{d^2 f(r)}{d^2 r} + 2r\frac{df(r)}{dr} - 2f(r) = 0. \tag{2.54}$$

Assuming $f(r) = r^n$, Eq. (2.54) reduces to

$$(n-1)(n+2) = 0. \tag{2.55}$$

Therefore,

$$v_\phi = \left(Ar + Br^{-2}\right)\sin\theta, \tag{2.56}$$

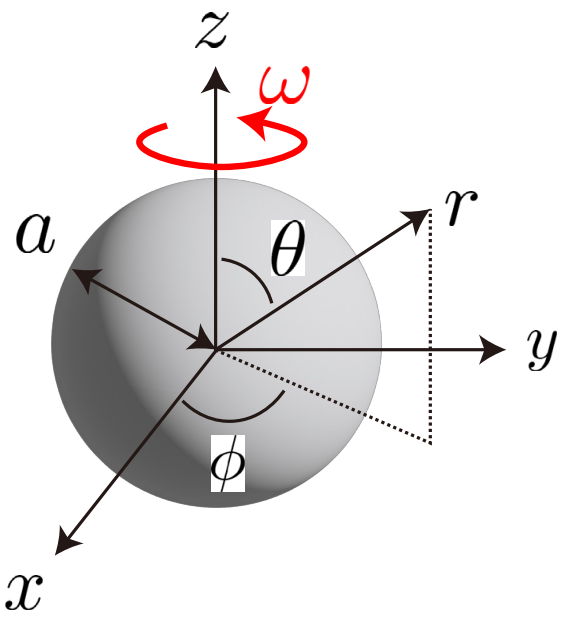

Figure 2.4. Schematic of a rotating sphere (radius a) with a constant angular frequency ω.

where A and B are constants determined by the boundary condition. $v_\phi(r \to \infty) = 0$ and $v_\phi(r = a) = a\omega \sin\theta$ give $A = 0$ and $B = \omega a^3$, respectively. Thus,

$$v_\phi = \frac{a^3 \omega \sin\theta}{r^2}. \tag{2.57}$$

We consider the force acting on the rotating sphere. Since $v_r = 0$ and $v_\theta = 0$, the viscous stress acting on the sphere surface is only $\tau_{r\phi}$,

$$\tau_{r\phi} = \eta r \frac{\partial}{\partial r}\left(\frac{v_\phi}{r}\right)\Big|_{r=a} = -3\eta\omega \sin\theta. \tag{2.58}$$

The net force caused by the pressure is zero due to symmetry and $p = const.$ Viscous torque Γ due to the viscous stress is expressed as

$$\begin{aligned} \Gamma &= \int_0^\pi \int_0^{2\pi} (-3\eta\omega \sin\theta)\,(a \sin\theta) a^2 \sin\theta d\phi d\theta \\ &= -8\pi\eta a^3 \omega. \end{aligned} \tag{2.59}$$

Slip boundary condition for a rotating sphere

The general solution of v_ϕ for the Stokes equation is given by Eq. (2.56),

$$v_\phi = \left(Ar + Br^{-2}\right)\sin\theta, \tag{2.56}$$

where A and B are constants determined by the boundary conditions. Since v_ϕ must not be infinite at $r \to \infty$, $A = 0$. In slip boundary conditions, the shear stress is described by the product of slip coefficient β and slip velocity v_{slip} [19]. v_{slip} is the difference between surface velocity of the sphere and flow velocity at the surface. In a rotating sphere, the shear stress $\tau_{r\phi}$ is given as

$$\tau_{r\phi} = \beta\left(v_\phi(a) - a\omega\sin\theta\right), \tag{2.60}$$

where a is the radius of the sphere. Since the tangential stress $\tau_{r\phi}$ is continuous,

$$\beta\left(v_\phi(a) - a\omega\sin\theta\right) = \eta r\,\frac{\partial}{\partial r}\left(\frac{v_\phi}{r}\right)\Big|_{r=a}. \tag{2.61}$$

Eq. (2.61) gives

$$B = \omega a^3\left(1 + \frac{3\eta}{\beta a}\right)^{-1}. \tag{2.62}$$

Finally, v_ϕ is given as

$$v_\phi = \frac{\omega a^3}{r^2}\sin\theta\frac{\beta a}{\beta a + 3\eta}. \tag{2.63}$$

When $\theta = \frac{\pi}{2}$,

$$v_\phi = \frac{\omega a^3}{r^2}\frac{\beta a}{\beta a + 3\eta}. \tag{2.64}$$

We also consider the force acting on the rotation sphere. The viscous stress due to rotation is $\tau_{r\phi}$,

$$\tau_{r\phi} = \eta r\frac{\partial}{\partial r}\left(\frac{v_\phi}{r}\right)\Big|_{r=a} = -3\eta\omega\sin\theta\frac{\beta a}{\beta a + 3\eta}. \tag{2.65}$$

In the slip boundary condition, viscous torque Γ due to the viscous stress is expressed as

$$\begin{aligned}\Gamma &= \int_0^\pi\int_0^{2\pi}\left(-3\eta\omega\sin\theta\frac{\beta a}{\beta a + 3\eta}\right)(a\sin\theta)a^2\sin\theta d\phi d\theta \\ &= -8\pi\eta a^3\omega\frac{\beta a}{\beta a + 3\eta}.\end{aligned} \tag{2.66}$$

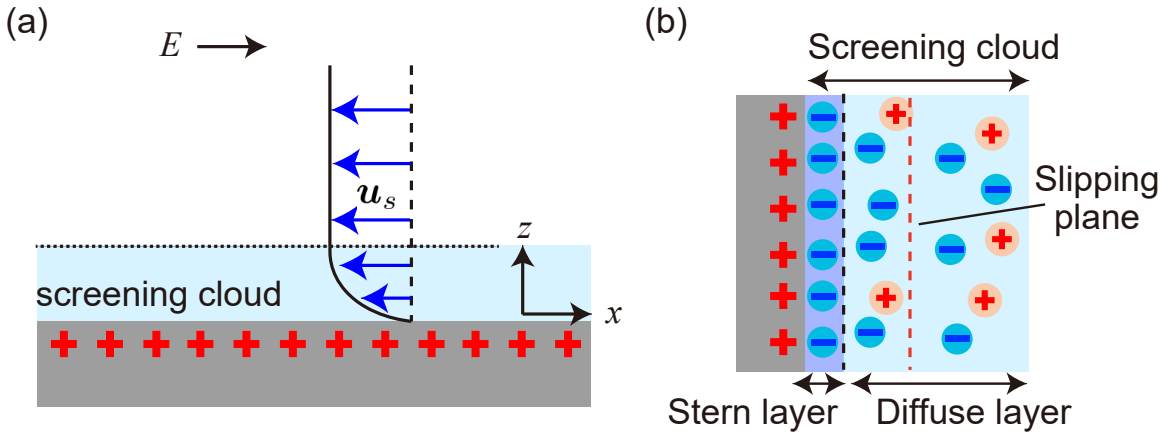

Figure 2.5. Schematic of (a) electro-osmotic flow and (b) electrical double layer. (a) Surrounding ions are driven by the electric field E parallel to the x-axis. The blue arrows represent the flow velocity near the surface. (b) Electrical double layer composed of the stern and diffuse layer. The dashed red line represents the slipping plane. The filled blue and red circles represent anions and cations, respectively.

2.5 Electro-osmotic flow

Electro-osmotic flow is the electrokinetic phenomenon involving the interaction between ionic screening clouds, applied electric fields, and hydrodynamic flow at low Reynolds number [20]. The importance of this phenomenon for colloid and interface science has led to much research. The basic mechanism is explained as follows. An ionic screening cloud forms around a charged solid surface in a liquid electrolyte. The cloud is typically a few nm thick, which is thin compared to other geometric features in the system. The external electric field exerts force on the ions in the cloud, and induces a flow around the solid surface as shown in Fig. 2.5(a). The resulting flow is electro-osmotic flow and appears to slip outside the screening cloud.

The Stokes equation for the screening cloud is expressed as

$$\nabla p - \eta \nabla^2 \boldsymbol{u} = \rho_{\mathrm{e}} \boldsymbol{E}, \tag{2.67}$$

where $\boldsymbol{u}$ is the fluid velocity, p is the pressure, ρ_{e} is the charge density and $\boldsymbol{E}$ is the electric field parallel to the x-direction as shown in Fig. 2.5(a). We assume that p does not vary with the x-direction and $\boldsymbol{u}$ is parallel to the x-direction. Accordingly,

we consider Eq. (2.67) only for the velocity in the x-direction u_s, which depends only on the z-position,

$$\begin{aligned} \eta \frac{d^2 u_s}{dz^2} &= -\rho_{\mathrm{e}} E \\ &= \varepsilon E \frac{d^2 \Psi}{dz^2}, \end{aligned} \tag{2.68}$$

where the Poisson equation $\rho_{\mathrm{e}} = -\varepsilon \frac{d^2 \Psi}{d^2 z}$ is used to express ρ_{e} with electric potential Ψ and the permittivity ε. The first integral of Eq. (2.68) gives

$$\eta \frac{du_s}{dz} = \varepsilon E \frac{d\Psi}{dz}, \tag{2.69}$$

where $du_s/dz \to 0$ and $d\Psi/dz \to 0$ at $z \to \infty$. The second integral from $z = 0$ to $z \to \infty$ gives

$$\begin{aligned} \eta \left(u_s(\infty) - u_s(0) \right) &= \varepsilon E \left(\Psi(\infty) - \Psi(0) \right) \\ &= -\varepsilon E \zeta, \end{aligned} \tag{2.70}$$

where $\zeta = \Psi(0) - \Psi(\infty)$ is the potential drop across the screening cloud.

- For fixed surface: $u(0) = 0$
  If the charged surface is fixed, $u(0) = 0$. The velocity $u_{\mathrm{s}}(\infty)$ is written as

  $$u_{\mathrm{s}}(\infty) = -\frac{\varepsilon \zeta}{\eta} E. \tag{2.71}$$

  This is the Helmholz-Smoluchowski formula [21].

- For freely suspended object: $u(\infty) = 0$
  In the freely suspended object $u(\infty) = 0$, the electro-osmotic flow drives the object. This phenomenon is called electrophoresis. The object velocity $u_{\mathrm{s}}(0)$ is written as

  $$u_{\mathrm{s}}(0) = \frac{\varepsilon \zeta}{\eta} E. \tag{2.72}$$

  This is the Smoluchowski equation [21].

2.5.1 Electrical double layer

We assume that the whole screening cloud is driven by an electric field. However, the ions in the vicinity of a charged surface do not move due to adsorption even when fluids flow. The boundary plane is called slipping plane [22]. Screening cloud is composed of Stern (adsorption layer) and diffuse layer as shown in Fig. 2.5(b), which is called electric double layer (EDL). EDL can be considered as a series circuit of capacitors of adsorption layer C_{im} and mobile one C_{m} [22]. The potential drop outside the slipping plane ζ_{slip} is expressed as

$$\zeta_{\mathrm{slip}} = \left(\frac{1}{1+\delta}\right)\zeta, \tag{2.73}$$

where $\delta = C_{\mathrm{m}}/C_{\mathrm{im}}$. δ depends on the concentration and type of surrounding ions [22]. Since only ions outside the slipping plane are moved by an electric field, the potential drop outside the slipping plane should be considered to calculate electro-osmotic flow in EDL. In this case, velocity of electro-osmotic flow u_{s} is proportional to $\frac{\varepsilon\zeta}{(1+\delta)\eta}E$,

$$u_{\mathrm{s}} \propto \frac{\varepsilon\zeta}{(1+\delta)\eta}E. \tag{2.74}$$

2.5.2 Induced-charge electro-osomotic flow

Electro-osmotic flow is induced not only for a fixed-charge object but also for a polarized object, which is called induced-charge electro-osmosis (ICEO) [21]. In the case of fixed charge (standard electro-osmosis), the potential ζ is constant. On the other hand, in the case of induced charge, ζ is proportional to $\boldsymbol{E}$ [20], and consequently, flow velocity u_{ICEO} induced by ICEO is proportional to $\boldsymbol{E}^2$,

$$u_{\mathrm{ICEO}} \propto \frac{\varepsilon E^2}{(1+\delta)\eta}. \tag{2.75}$$

ICEO drives freely suspended particles, which is called induced-charge electrophoresis (ICEP). For the particle, velocity U_{ICEP} of electrophoresis due to ICEO is calculated by sum of $\boldsymbol{u}_{\mathrm{ICEO}}$ on the particle surface [23],

$$U_{\mathrm{ICEP}} = -\frac{1}{4\pi}\int \boldsymbol{u}_{\mathrm{ICEO}}(\theta)d\Omega, \tag{2.76}$$

where $d\Omega$ is an element of solid angle. Since symmetrical flow induces no net motion, asymmetrical flow is necessary to drive an object. A Janus particle induces an asymmetric flow, and the particle is self-propelled by ICEO. The mechanism of ICEP is explained in Section 3.2.

Chapter 3

Mechanism of rotation and translation

In order to control active particles, it is important to understand their driving mechanisms. In this section, the mechanism of motion for a birefringence object (rotation) and a Janus particle (translation) is briefly explained.

3.1 Rotation of birefringent particle

Famous birefringence objects are vaterite and calcite, which are polymorphs of calcium carbonate ($CaCO_3$) [9]. The optical path length inside the particle depends on the oscillatory direction of the electric field of light. Due to the difference in the optical path length, the polarization changes between incident and transmitted light as shown in Fig. 3.1. This phenomenon is called waveplate effect. Polarization state is related to spin angular momentum of light, and the change of the polarization means the transfer of the momentum to the birefringent object.

We consider the spin angular momentum for the incident and transmitted beams to estimate the transferred torque. An elliptically polarized incident plane wave $\boldsymbol{E}_{\mathrm{in}}$

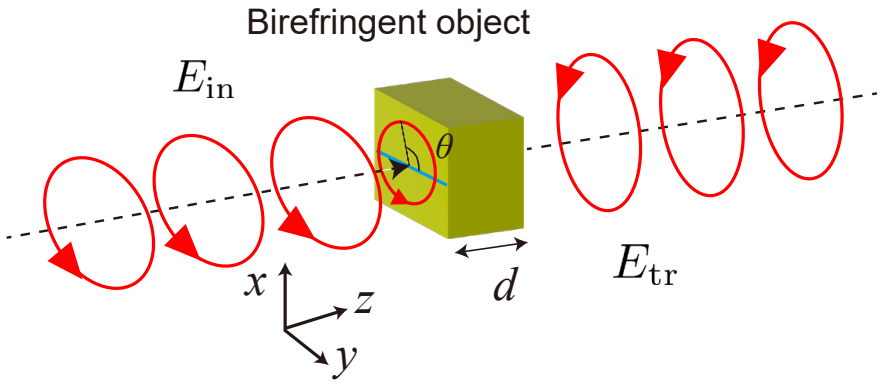

Figure 3.1. Schematic of light transmitted through a birefringent object with thickness d. The red arrow represents the polarization of light. The blue line represents the optical axis of the birefringent object. θ is the angle between the major axis of the polarization ellipse and the optical axis.

is written as

$$\boldsymbol{E}_{\mathrm{in}} = E_0 \left(\cos\varphi\hat{\boldsymbol{x}} + i\sin\varphi\hat{\boldsymbol{y}}\right) e^{-ift}, \tag{3.1}$$

where E_0 is the amplitude of the electric field, f is the frequency of light, φ is the ellipticity angle of the laser beam, and $\hat{\boldsymbol{x}}$ and $\hat{\boldsymbol{y}}$ represent the unit vectors in the x- and y- directions, respectively. The linearly polarized beam corresponds to $\varphi = 0$, and the circularly polarized beam corresponds to $\varphi = \pi/4$. Unit vectors of the circular basis are useful for calculation, which is expressed as

$$\hat{\boldsymbol{e}}_+ = \frac{1}{\sqrt{2}}\left(\hat{\boldsymbol{x}} + i\hat{\boldsymbol{y}}\right), \tag{3.2}$$

$$\hat{\boldsymbol{e}}_- = \frac{1}{\sqrt{2}}\left(\hat{\boldsymbol{x}} - i\hat{\boldsymbol{y}}\right), \tag{3.3}$$

where $\hat{\boldsymbol{e}}_+$ and $\hat{\boldsymbol{e}}_-$ correspond to right and left-handed circular polarization propagating in the z-direction, respectively. Here, the direction of circular polarization is defined from the point of view of the receiver. The rotation axis of the circular polarization The unit vectors have the following properties:

$$\hat{\boldsymbol{e}}_+^* = \hat{\boldsymbol{e}}_-, \tag{3.4}$$

$$\hat{\boldsymbol{e}}_-^* = \hat{\boldsymbol{e}}_+, \tag{3.5}$$

$$\hat{\boldsymbol{e}}_+ \times \hat{\boldsymbol{e}}_- = -i\hat{\boldsymbol{z}}, \tag{3.6}$$

where A^* represents the complex conjugate of A. Using $\hat{\boldsymbol{e}}_+$ and $\hat{\boldsymbol{e}}_-$, $\boldsymbol{E}_{\mathrm{in}}$ is rewritten as

$$\boldsymbol{E}_{\mathrm{in}} = \frac{E_0}{\sqrt{2}} e^{-ift}\left[\left(\cos\varphi + \sin\varphi\right)\hat{\boldsymbol{e}}_+ + \left(\cos\varphi - \sin\varphi\right)\hat{\boldsymbol{e}}_-\right]. \tag{3.7}$$

The average spin angular momentum density $\boldsymbol{L}$ for an electric field is expressed as [9, 24, 25]

$$\boldsymbol{L} = \frac{\varepsilon}{2if}\boldsymbol{E}^* \times \boldsymbol{E}, \tag{3.8}$$

where ε is the permittivity of the medium (Brief derivation is presented in Appendix A). We assume that the medium is isotropic because the used medium is water or an aqueous glycerin solution. The average spin angular momentum density for the

incident light $\boldsymbol{L}_{\rm in}$ is written as

$$\begin{aligned}\boldsymbol{L}_{\rm in} &= \frac{\varepsilon}{2if}\boldsymbol{E}_{\rm in}^{*}\times\boldsymbol{E}_{\rm in}\\ &= \frac{\varepsilon}{2if}\frac{E_0^2}{2}\left[(\cos\varphi+\sin\varphi)^2\,\hat{\boldsymbol{e}}_-\times\hat{\boldsymbol{e}}_+ + (\cos\varphi-\sin\varphi)^2\,\hat{\boldsymbol{e}}_+\times\hat{\boldsymbol{e}}_-\right]\\ &= \frac{\varepsilon E_0^2}{2f}\sin 2\varphi\hat{\boldsymbol{z}}. \end{aligned} \tag{3.9}$$

Next, we consider the transmitted light $\boldsymbol{E}_{\rm tr}$. Since change of the polarization by passing through a birefringent object depends on the angle θ between the major axis of the polarization ellipse and the optical axis of the object, the rotation matrix $R(\theta)$ is introduced,

$$\begin{pmatrix}E_x\\E_y\end{pmatrix} = \begin{pmatrix}\cos\theta & -\sin\theta\\ \sin\theta & \cos\theta\end{pmatrix}\begin{pmatrix}\cos\varphi\\ i\sin\varphi\end{pmatrix}. \tag{3.10}$$

$\boldsymbol{E}$ is written as

$$\boldsymbol{E} = E_0 e^{-ift}\left[(\cos\theta\cos\varphi - i\sin\theta\sin\varphi)\,\hat{\boldsymbol{x}} + (\sin\theta\cos\varphi + i\cos\theta\sin\varphi)\,\hat{\boldsymbol{y}}\right]. \tag{3.11}$$

In a birefringent object, the refractive index depends on the direction of oscillation of the electric field characterized by the extraordinary and ordinary ray [26]. The oscillatory direction of the ordinary ray is perpendicular to the optical axis of the object, whereas the oscillatory direction of the extraordinary ray is parallel to the optical axis. We impose that the x-axis is parallel to the optical axis. The phase shift due to passing through the object with a thickness d is kdn where n is the refractive index and $k = 2\pi/\lambda$ is the wavenumber (λ is the wavelength of light). $\boldsymbol{E}_{\rm tr}$ is written as

$$\boldsymbol{E}_{\rm tr} = E_0 e^{-ift}\left[e^{ikdn_{\rm e}}(\cos\theta\cos\varphi - i\sin\theta\sin\varphi)\,\hat{\boldsymbol{x}} + e^{ikdn_{\rm o}}(\sin\theta\cos\varphi + i\cos\theta\sin\varphi)\,\hat{\boldsymbol{y}}\right], \tag{3.12}$$

where $n_{\rm e}$ and $n_{\rm o}$ are the refractive indices for extraordinary and ordinary rays, respectively. The average spin angular momentum density for the transmitted light $\boldsymbol{L}_{\rm tr}$ is calculated in the same way as for $\boldsymbol{L}_{\rm in}$, and the following expression is obtained,

$$\boldsymbol{L}_{\rm tr} = \frac{\varepsilon E_0^2}{2f}(\cos\Delta\sin 2\varphi - \sin\Delta\cos 2\varphi\sin 2\theta)\,\hat{\boldsymbol{z}}, \tag{3.13}$$

where Δ is the retardance expressed by $\Delta = 2\pi\Delta nd/\lambda$, ($\Delta n = n_{\rm e} - n_{\rm o}$).

The transfer of angular momentum density $\Delta \boldsymbol{L}$ from the light to the object corresponds to the difference between $\boldsymbol{L}_{\mathrm{in}}$ and $\boldsymbol{L}_{\mathrm{tr}}$,

$$\begin{aligned}\Delta \boldsymbol{L} &= \boldsymbol{L}_{\mathrm{in}} - \boldsymbol{L}_{\mathrm{tr}} \\ &= \frac{\varepsilon E_0^2}{2f} \left[(1-\cos\Delta)\sin\varphi - \sin\Delta\cos 2\varphi \sin 2\theta\right] \hat{\boldsymbol{z}}. \end{aligned} \tag{3.14}$$

The reaction torque Γ per unit time Δt is calculated by integrating the ΔL on a volume element $Sc\Delta t$,

$$\begin{aligned}\boldsymbol{\Gamma} &= \frac{Sc\Delta t \Delta \boldsymbol{L}}{\Delta t} = Sc\Delta L \\ &= \frac{c\varepsilon E_0^2 S}{2f} \left[(1-\cos\Delta)\sin\varphi - \sin\Delta\cos 2\varphi \sin 2\theta\right] \hat{\boldsymbol{z}} \\ &= \frac{P}{f} \left[(1-\cos\Delta)\sin\varphi - \sin\Delta\cos 2\varphi \sin 2\theta\right] \hat{\boldsymbol{z}} \end{aligned} \tag{3.15}$$

where S is the irradiation area, c is the speed of light and $P = \frac{\varepsilon}{2} ScE_0^2$ is the light power [27]. The applied torque Γ is proportional to the light power P, $\Gamma \propto P$. The first term on the right-hand side of Eq. (3.15) represents the contribution of the spin angular momentum. This term rotates the object in the same direction as the rotation for the polarization ellipse. The second term represents the alignment effect along the major axis of the elliptical polarization, except when the incident beam is circularly polarized.

Controlling polarization of light enables orientational control of the birefringent object. For example, linearly polarized light controls the orientation of birefringent objects as shown in Fig. 3.2(a). Further, circularly polarized light induces continuous rotation as shown in Fig. 3.2(b). However, size control of vaterite is not easy [28].

Another typical birefringent object is a liquid crystal (LC) droplet [29]. Since LC material also has birefringence, LC droplets can be controlled by polarized light [14]. The development of microfluidic technology enables precise control of droplet size ranging from a few µm to hundreds of µm [30].

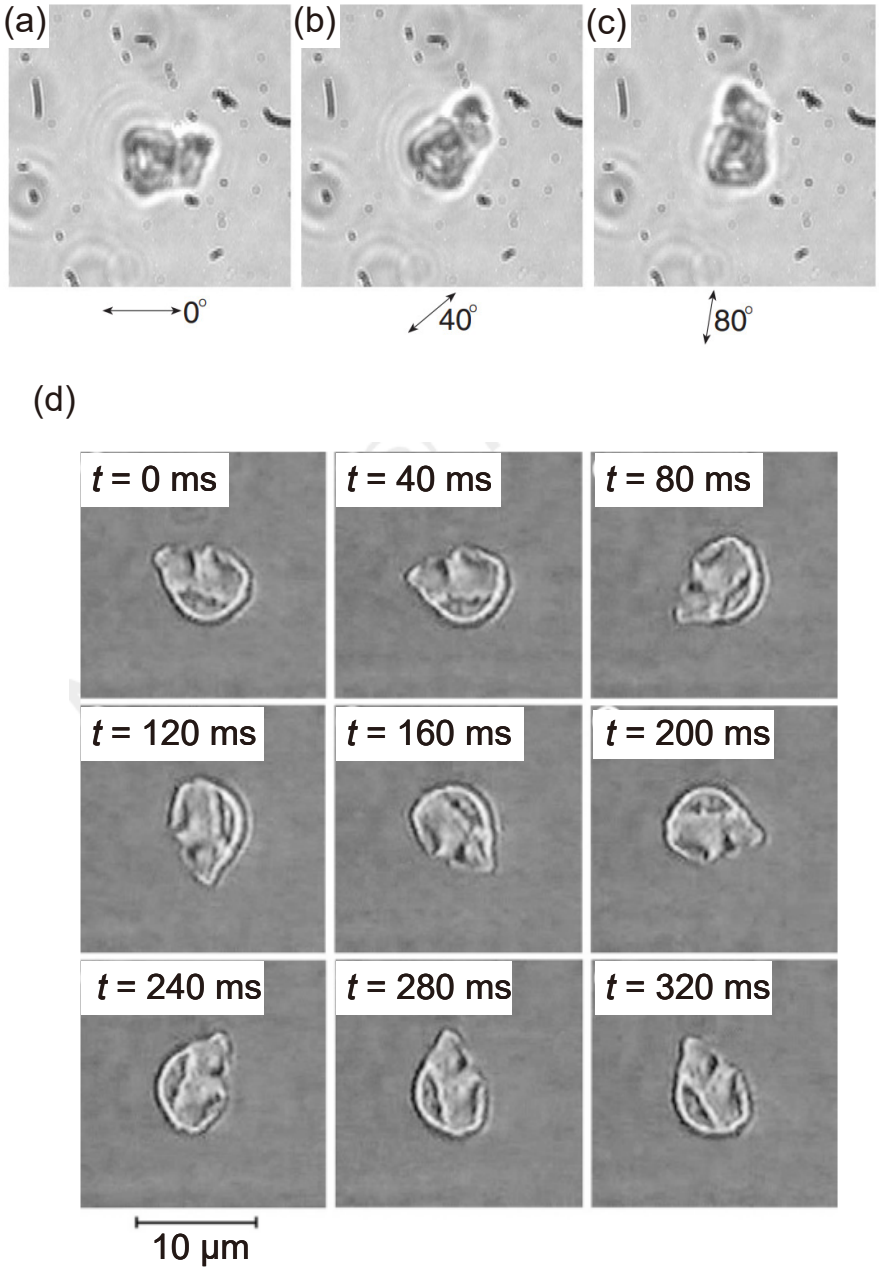

Figure 3.2. Orientational control of the calcite crystal [9]. (a) Orientational control by linear polarized light. The double arrow represents the direction of the linear polarization. (b) Sequential images of the rotating calcite by circularly polarized light. The frames are 40 ms apart.

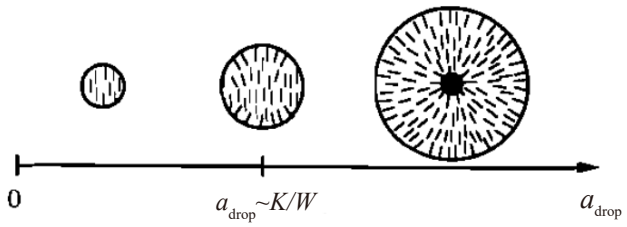

Figure 3.3. Schematic of the inner structure of a nematic LC droplet with homeotropic anchoring (normal anchoring) [31]. The LC molecules in a large droplet with $a_{\mathrm{drop}} \gg K/W$ align radially. The LC molecules tend to align in the same direction for a small droplet with $a_{\mathrm{drop}} \ll K/W$.

3.1.1 LC droplet

LC droplets have several inner structures depending on the type of LC and anchoring [29]. LC molecules align in a certain direction due to the effect of the surface, which is called anchoring. The inner structure is determined by the minimum of the free energy function F_{LC} expressed as

$$F_{\mathrm{LC}} = F_{\mathrm{V}} + F_{\mathrm{S}}, \tag{3.16}$$

where F_{V} and F_{S} arise from the bulk elastic energy and surface energy, respectively [31]. F_{V} for an LC droplet can be scaled with a radius of the droplet a_{drop} as $F_{\mathrm{V}} \propto Ka_{\mathrm{drop}}$ (K is the elastic constant). On the other hand, F_{S} can be scaled with a_{drop}^2 as $F_{\mathrm{S}} \propto Wa_{\mathrm{drop}}^2$ (W is the anchoring strength coefficient). Since the surface energy is dominant for a large droplet, the surface anchoring is the dominant effect on the inner structure for the large droplet. On the other hand, for a small droplet with $a_{\mathrm{drop}} \ll K/W$, the main contribution to the inner structure is the bulk elasticity. Figure 3.3 shows variation of the inner structure of a nematic LC droplet with homeotropic anchoring where LC molecules align perpendicular to the surface. For a large droplet, the LC molecules align radially due to the homeotropic anchoring. On the other hand, for a small droplet, the LC molecules tend to align in the same direction to decrease the bulk elastic energy. The critical radius $a_{\mathrm{c}} = K/W$ is of the order of 1 µm with typical $W \sim 10^{-5}$ J/m^2 and $K \sim 10^{-11}$ N [31]. In the following, we consider the situation where the effect of surface anchoring is dominant.

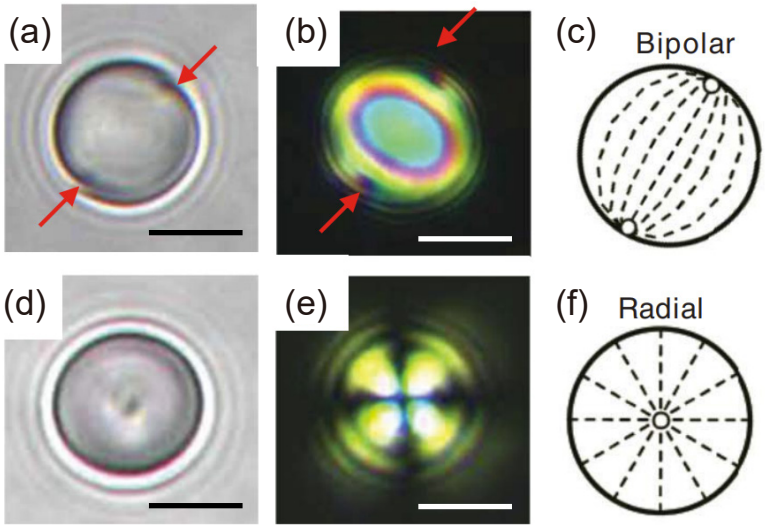

Figure 3.4. NLC droplets with bipolar (a-c) and radial (d-e) structures [32]. Bright field images of bipolar (a) and radial (d) structure. Polarized images of bipolar (b) and radial (e) structure. Schematic of the inner structures of bipolar (c) and radial (f) structures. The red arrow represents the boojums at the aqueous-LC interface of the droplet. Scale bars are 5 µm.

3.1.2 Nematic LC droplte

In nematic LC (NLC) droplets, bipolar and radial structures are mainly observed as shown in Fig. 3.4. The boundary condition of LC molecules on the droplet surface determines whether the inner structure is bipolar or radial [29]. For tangential anchoring at the droplet surface, LC molecules align along the surface, and two point defects exist at the poles of the droplet as shown in Figs. 3.4(a)-(c). This structure is called bipolar. On the other hand, for homeotropic anchoring where LC molecules align perpendicular to the surface, the center of the droplet has a defect (radial hedgehog) as shown in Figs. 3.4(d)-(f). This structure is called radial.

The response of bipolar and radial droplets to circularly polarized light is different. A bipolar droplet rotates in a plane where two defects exist as shown in Fig. 3.5(a). Since the irradiated area can be regarded as a uniaxial birefringent object when the irradiated area is small, waveplate effect can be used to explain the rotation of

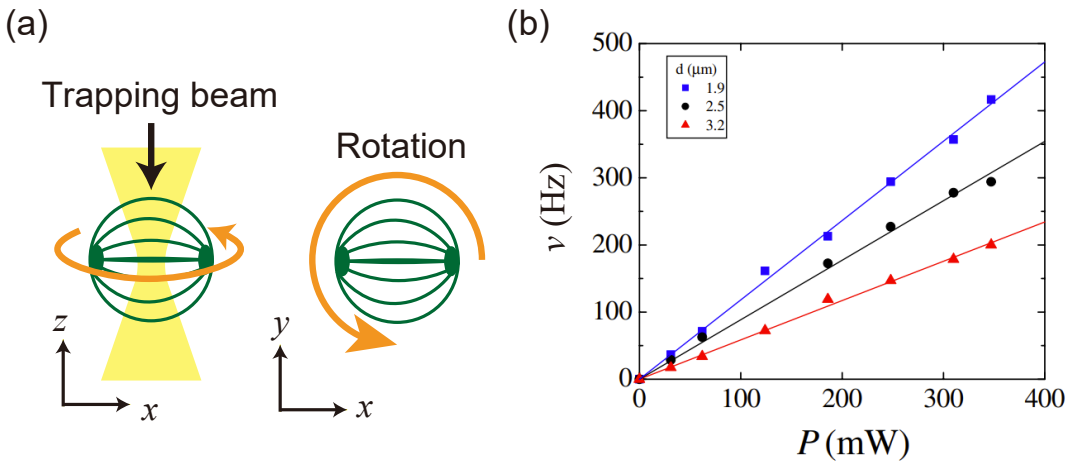

Figure 3.5. Bipolar droplet rotation under irradiation with circularly polarized beam. (a) A trapped bipolar droplet. The rotation axis is the z axis. (b) Power dependence of rotation frequency ν of bipolar droplets with diameter d [14].

the droplets [14]. Its rotation frequency ν is proportional to applied laser power as shown in Fig. 3.5(b), and this is consistent with waveplate effect. On the other hand, the behavior of a radial droplet is different from that in bipolar one. Since the radial structure is symmetric and has no optical anisotropy, the droplet does not rotate. However, high-power irradiation changes the orientation of LC molecules via optical Freedericksz transition as shown in Fig. 3.6(a) [33]. The droplet becomes a birefringent object due to the change of the orientation, resulting in rotation under the irradiation with circularly polarized light as shown in Fig. 3.6(b). Figure 3.6(c) shows the power dependence of rotation frequency. In rotation region, nonlinear power dependence indicates that the induced birefringence has strongly nonlinear power dependence [34].

3.1.3 Cholesteric liquid crystal (ChLC) droplet

A ChLC droplet has helical molecular alignment with pitch p inside the droplet as shown in Figs. 3.7(a) and (b). ChLC can be fabricated by mixing NLC and a chiral dopant such as CB-15 [29]. p becomes shorter as the concentration of the chiral dopant increases as shown in Figs. 3.7(i)-(v) of (a) and (b) [35]. The inner structure of a ChLC droplet also varies depending on an anchoring type (tangential

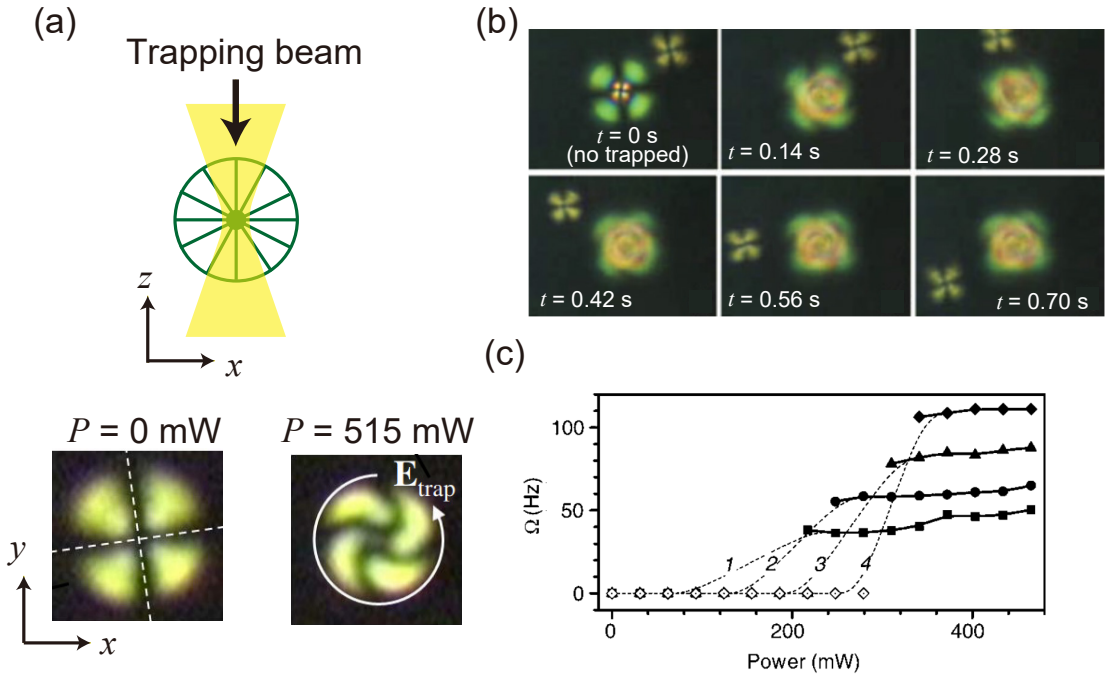

Figure 3.6. Rotation of radial droplets [14, 33]. (a) Schematic of a trapped droplet with circularly polarized beam. Images of the trapped droplets with power P= 0 mW (left) and 515 mW (right) under the crossed-Nicol state. (b) Images of the rotating droplet under the crossed-Nicols state. (c) Power dependence of rotation frequency Ω in several diameters (1: 7.8 µm, 2: 6.7 µm, 3: 5.4 µm and 4: 4.8 µm,) [33].

or homeotropic) as shown in Figs. 3.7(a) and (b).

ChLC droplets and solidified ChLC droplets with tangential anchoring exhibit rotation under irradiation with circularly polarized light [27, 36, 37]. The helical structure of ChLC reflects circularly polarized light when the direction of circularly polarized light is the same as the chirality of the structure [38]. This phenomenon is called Bragg reflection. Since the droplet recieves reaction torque via the Bragg reflection, the droplet also rotates. Since Bragg reflection only occurs when the direction of circularly polarized light is the same as the chirality of the particle, the chiral particle rotates only in the same direction as the chirality [27].

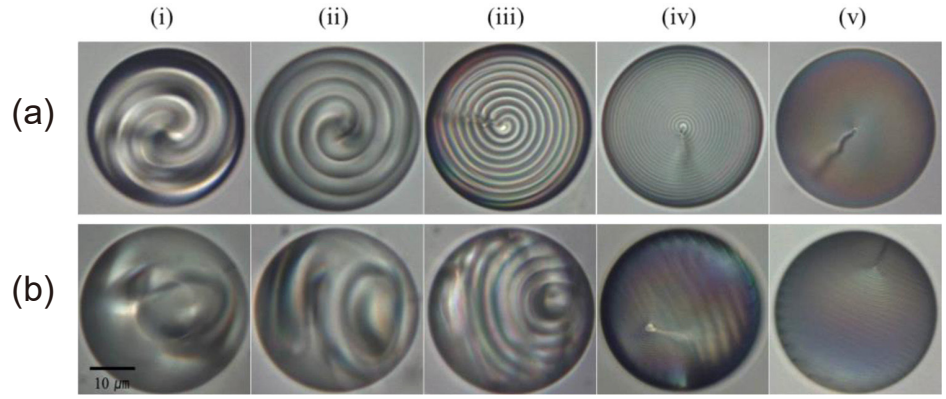

Figure 3.7. Bright field images of ChLC droplets for tangential (a) and homeotropic (b) anchoring in several concentrations of a chiral dopant, (i) 0.8, (ii) 1, (iii) 2, (iv) 5 and (v) 10 wt% [35]. Corresponding p for tangential anchoring are (i) 24 µm, (ii) 21 µm, (iii) 9 µm, (iv) 4 µm and (v) 2 µm.

3.2 Self-propelled motion of Janus particles

A Janus particle usually has two different surfaces, and there are many combinations of surface materials [10]. Since the driving mechanism depends on the material combination, we can choose a suitable driving method according to the situation. Three typical driving methods are presented: chemical, optical and electrical control of Janus particles.

3.2.1 Chemical methods

The chemical method is one of the most studied methods. Platinum (Pt) and polystyrene (PS) are often used as surface materials of a Janus particle where Pt works as a catalyst. The driving mechanism is briefly explained as follows [40].

1. Catalytic decomposition
   When the Janus with Pt hemisphere is dispersed in an H_2O_2 solution, catalytic decomposition of H_2O_2 into water and oxygen occurs on the Pt surface. This decomposition ($2H_2O_2 \rightarrow H_2O + 2H_2$) induces the concentration gradient as shown in Fig. 3.8(a).
2. Induced flow by concentration gradient

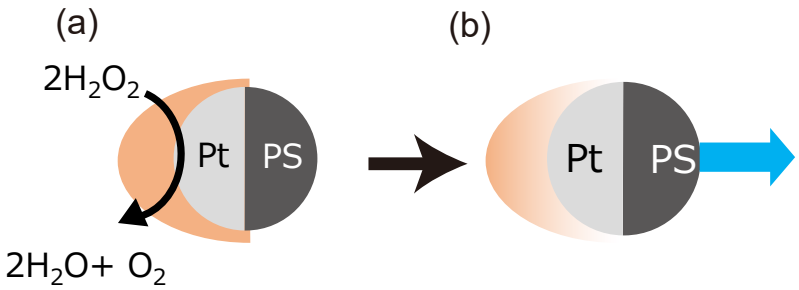

Figure 3.8. Schematic of diffusionpheresis for a Janus particle composed of platinum (Pt) and polystyrene (PS) in an H_2O_2 solution [39]. (a) Catalytic decomposition of H_2O_2 into water and oxygen on the Pt side. The intensity of the red color represents the concentration of reaction products. (b) Diffusionpheresis induced by the concentration gradient of reaction products. The blue arrow represents the self-propelled direction.

Due to the decomposition, concentration of the reaction products becomes high at the Pt side. This gradient of the concentration induces flow, resulting in particle motion known as diffusionpheresis as shown in Fig. 3.8(b).

The combination of Pt and PS is not special, and a pair of other materials is applicable [41]. This method has some problems. A limited quantity of fuel (H_2O_2) makes long-time observations difficult. Further, the composition of the solution changes due to the chemical reaction, and this leads to changes in the solution properties.

3.2.2 Optical methods

Light irradiation drives Janus particles dispersed in a binary mixture of water and lutidine [42]. In this method, a light-absorbing material is used as the surface of one side, and a typical combination is Au-silica or carbon-silica. Since this method does not involve chemical reactions, the composition of the solution does not change. The driving mechanism is briefly explained as follows [42].

1. Local heating
   The fluid in which the Janus particles disperse is a binary mixture of water and lutidine with a critical temperature of 307 K. The mixture separates into water and lutidine phases above the critical temperature. The metal (carbon) hemisphere of a Janus particle absorbs light and releases the heat to a surrounding solution as shown in Fig. 3.9(a).
2. Demixing of mixture
   Due to the local heating on the metal cap, the solution near the cap is demixed, and a concentration gradient of water and lutidine appears as shown in Fig. 3.9(b). This gradient induces flow, resulting in particle motion known as diffusionpheresis [42, 44]. The Janus particle will move away from the metal cap.

The advantage of the optical method is good tunability in intensity, wavelength, and temporal modulation. Multi-particle control can be realized using optical manipulation techniques as shown in Fig. 3.9(c) [43]. However, it is difficult to accurately control the temperature. Further, there is a possibility of changing the solution properties due to the heating or phase separation.

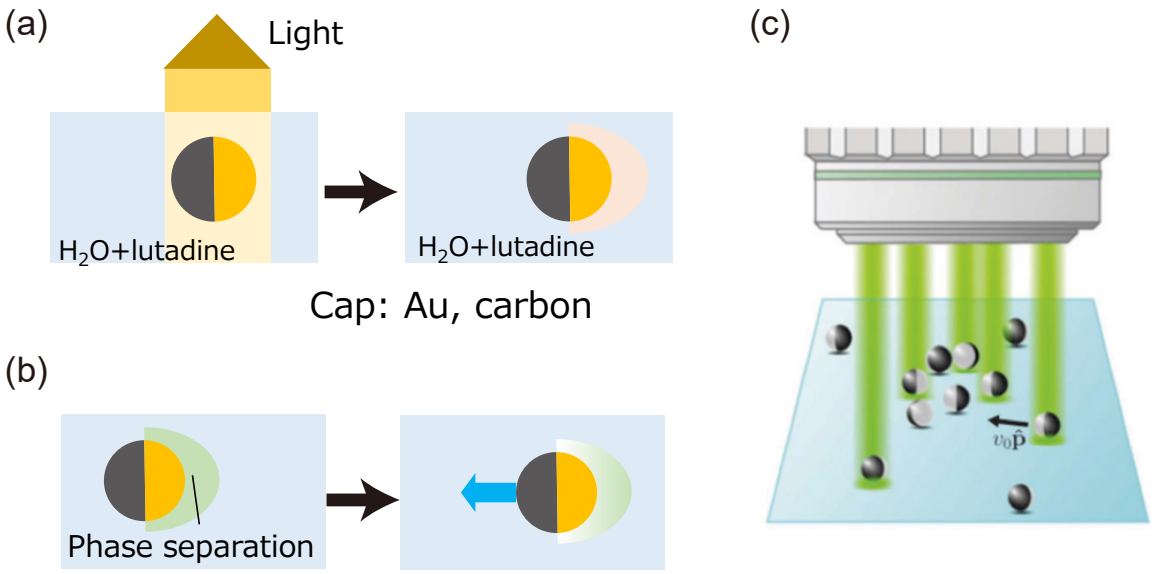

Figure 3.9. Swimming Janus particles in a binary mixture of water and lutidine [43]. (a) Light absorption on the yellow cap (Au or carbon) induces local heating illustrated by the red region. (b) Phase separation caused by the local heating induces diffusiophoresis. The blue arrow represents the self-propelled direction. (c) Multi-particle control by laser manipulation.

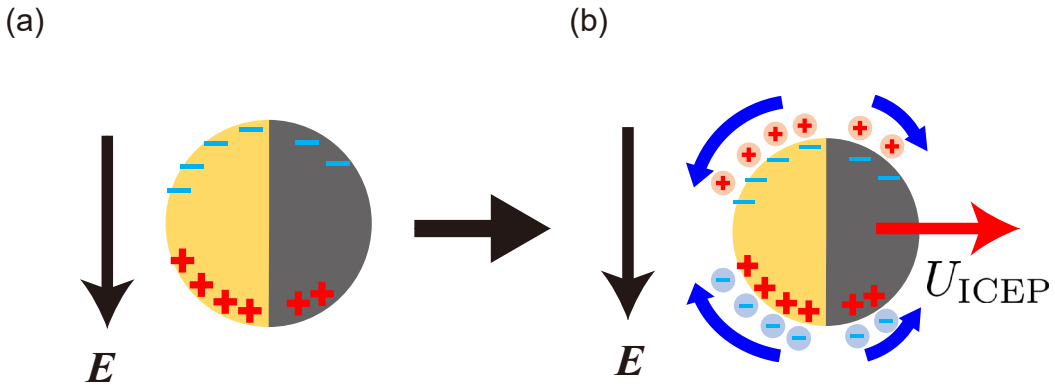

Figure 3.10. Schematic explanation of induced-charge electrophoresis. The yellow and grey areas represent the metal and dielectric surfaces, respectively. (a) Surface charge is induced by an applied electric field $\boldsymbol{E}$. "-" and "+" represent the negative and positive charge induced by the electric field, respectively. The black arrow represents the direction of $\boldsymbol{E}$. (b) Induced flow field around the Janus particle. The filled red and blue circles represent cations and anions, respectively. The blue arrow denotes the flow of the surrounding fluid. The red arrow represents the direction of propulsion.

3.2.3 Induced-charge electrophoresis (ICEP)

An AC electric field can also drive Janus particles immersed in an electrolyte solution. This phenomenon is known as induced-charge electrophoresis (ICEP). ICEP was first predicted theoretically [20] and subsequently demonstrated experimentally in 2008 [45]. The propulsion mechanism is briefly explained as follows [20]:

1. Induced charge on a Janus particle surface
   Under an electric field E, surface charge on the Janus particle is induced as shown in Fig. 3.10(a). The amount of surface charge on the metal side is greater than that on the dielectric side.
2. Induced flow around the particle
   The surface charge on the particle attracts surrounding ions, and then the attracted ions move along the applied electric field as shown in the blue arrows of Fig. 3.10(b). Due to the asymmetrical charge distribution on the particle surface, the induced flow on the metal side is stronger than that on the dielectric side. Consequently, the particle moves with its dielectric hemisphere forward.

Since ICEP does not involve heating or chemical reaction, it has less influence on the surrounding solution compared to the above two methods. The self-propelled velocity depends not only on the magnitude of the electric field but also on its frequency. ICEP does not occur at high-frequency regions because surrounding ions cannot follow the AC electric field with a high frequency [46].

The propulsion velocity of ICEP U_{ICEP} is calculated by Eq. (2.76). U_{ICEP} is expressed as [20]

$$U_{\mathrm{ICEP}} = \frac{9}{64}\frac{\varepsilon a E^2}{\eta(1+\delta)}, \tag{3.17}$$

where a is the radius of the particle, ε is the permittivity, η is the viscosity of the solution and $\delta = C_{\mathrm{m}}/C_{\mathrm{im}}$ is the ratio of capacitors of mobile layer C_{m} to that of adsorption layer C_{im}. Eq. (3.17) assumes that the induced flow occurs on only the metal side because the induced flow of the metal side is much greater than that of the dielectric side.

3.3 Outline

Systems composed of complex fluids and active particles have the potential for novel materials and could be good models for understanding biological microswimmers. Although motion of active particles in complex fluids is a critical issue to understand nonequilibrium soft matter, researches on active particles in complex fluids and artificially activated complex fluids are limited. The purpose of this study is to systematically understand the motion of active particles in viscous or viscoelastic fluids. We used two types of active particles to achieve this purpose: rotating particles (Chapter 4 and 5) and translating particles (Chapter 6).

In Chapter 4, optically driven LC droplets are used as active particles because their fabrication and size control are easy. First, the driving mechanism and its energy efficiency are investigated using several types of LC droplets. Efficient driving is important because viscosity of complex fluids is relatively higher. Further, light intensity with low power suppresses heating of the system. Next (Chapter 5), the rotational frequency of the droplet and the flow field around the droplet are studied using efficient droplets. As an application of the droplets, we construct a micro-viscometer. Subsequently, the hydrodynamic interaction between two rotating droplets in viscous fluids is studied.

In Chapter 6, we control tranlational motion of Janus particles in polymer solutions. The relationship between rotation and translation of a Janus particle is studied. The experimental results are discussed by considering time-delayed restore force from the polymer network.

Finally, we summarize our study in Chapter 7 and discuss future perspectives of driven non-equilibrium soft matter by local force generators.

Chapter 4
Optically driven liquid crystal droplet rotator

4.1 Introduction

Micromanipulation is important for evaluating the microscopic properties of soft materials [47, 48]. Optical tweezers allow precise control of micro-objects such as colloids, micro-organisms and cells in a non-contact and non-invasive manner [49]. The transfer of the linear and angular momenta of light to materials induces their translational and rotational motions, respectively. Indeed, colloids can be arranged in complex patterns and can be dynamically controlled in a complex manner [50]. The orientation of birefringent objects can also be controlled using polarized light [9]. Irradiating a birefringent object with circularly polarized light induces continuous rotation (spinning motion) [9].

Liquid crystal (LC) droplets are typical birefringent materials, and an LC droplet can be rotated by circularly polarized light [14, 51, 52]. The inner structure depends on the boundary condition of the molecules at the droplet surface [29, 53]. For tangential anchoring at the surface of a nematic LC (NLC) droplet, the LC molecules are aligned parallel to the droplet surface. In this anchoring, two point defects exist at the poles of the droplet, and this is called the bipolar structure [29]. On the other hand, for homeotropic anchoring, the NLC molecules are arranged radically. In this alignment, there is a single point defect at its center, and this is known as the radial structure[29]. In addition to the bipolar and radial structures, several other structures exist depending on the strength and type of anchoring [29]. A cholesteric LC (ChLC) droplet, which has a helical molecular arrangement, can be fabricated by stirring the mixture of an NLC and a chiral dopant [29, 54]. The ratio of the droplet diameter d to helical pitch p is an important parameter that determines the inner structure of the ChLC droplet [54].

Several mechanisms for the rotation of LC droplets have been investigated, and their main contributions depend on their inner structure [27, 37, 55–59]. For example, in a bipolar structure, the waveplate effect and light-scattering process are dominant [56–58]. It has been reported that the rotation frequency of the bipolar droplet

reaches up to 10^3 Hz[51]. However, in a radial structure, the droplet does not rotate under weak light [14]. In chiral solid particles composed of optically cured ChLCs which are the mixture of a photo-polymerizable monomar and ChLC, the helical arrangement of LC molecules induces the Bragg reflection under the irradiation of circularly polarized light. This Bragg reflection induces the rotation by Gaussian [27, 37] and non-Gaussian trap[59]. Since Bragg reflection only occurs if the direction of circularly polarized light is the same as the chirality of the particle, the chiral particle rotates only in the same direction as the chirality [27]. Under specific conditions (strong light irradiation that reorganizes the molecular alignment of a ChLC droplet with $d/p = 0.5$ or 1), linearly polarized light rotates the droplet [60].

An LC droplet is a useful material for opto-microfluidic devices because its angular frequency of rotation can be controlled without contact and size of the droplet can be easily controlled. High efficiency of energy transfer to LC droplets is important for the application of LC droplets to opto-microfluidic devices. It is also important to clarify the relationship between the optical interactions of the LC droplets and their inner structures in order to understand the rotation mechanism in detail. This leads to the fabrication of opto-microfluidic devices with high energy transfer efficiency.

In this section, we investigate the optical torque transfer to NLC and ChLC droplets by varying the inner structure to discuss which inner structure can rotate an LC droplet more efficiently. The effects of droplet size and chirality on the applied torque are also measured. The experimental results are discussed by the inner structure of the droplets [35, 61].

4.2 Optical tweezers

Microscopic objects such as colloidal particles and cells can be trapped three-dimensionally and manipulated by a strongly focused laser beam. This technique is usually called "optical tweezers" (OT). The concept of OT was first introduced by A. Ashkin [62, 63]. LC droplets used were also controlled with OT. The trapping mechanism is interpreted in terms of both ray optics and electromagnetic theory.

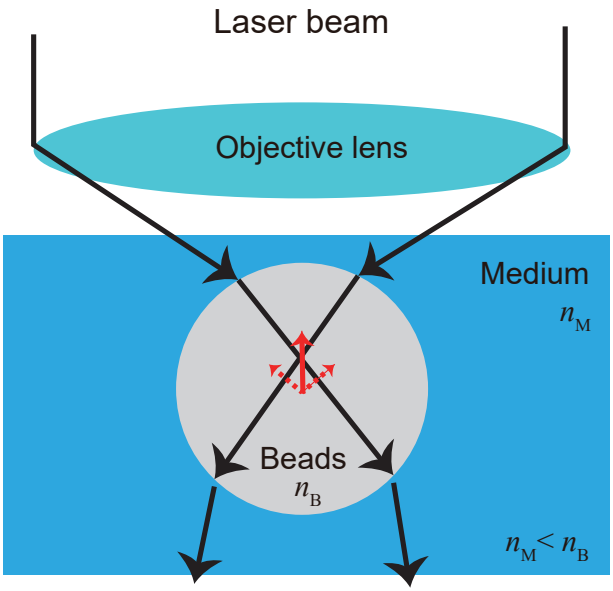

Figure 4.1. A trapped particle by an optical tweezer. The black arrows represent ray of light. The dashed red arrows represent the momentum transferred to the bead due to the refraction of each ray. The solid red arrow represents the sum of the transferred momentum.

4.2.1 Principle based on ray optics

Trapping force of OT is explained by ray optics when the wavelength of light is smaller than the object to be manipulated. Light has momentum and its momentum can be transferred by refraction. We consider a focused beam propagating in colloidal dispersion as shown in Fig. 4.1. The focused beam is refracted at the interface between a surrounding solution and a colloidal particle due to the difference in refractive index (solution n_{M} and particle n_{B}) as shown in Fig. 4.1. Due to the refraction, the momentum of the light changes by passing through the particle, and the particle receives the momentum as its reaction. As a result, the particle is pushed toward the focal position of the beam.

4.2.2 Principle based on electromagnetic theory

When an object is much smaller than the wavelength of the laser beam, trapping mechanism is explained by electromagnetic theory. An electric field $\boldsymbol{E}$ of the laser

beam induces electric dipole $\boldsymbol{p} = \alpha_{\mathrm{p}}\boldsymbol{E}$ in an object where α_{p} is polarizability of the object. The electric dipole $\boldsymbol{p}$ is also written as $\boldsymbol{p} = q\boldsymbol{d}_{\mathrm{q}}$ where q is the magnitude of the induced charge and $\boldsymbol{d}_{\mathrm{q}}$ is the position vector from negative to positive charge in the dipole. Considering positive and negative charges, Lorentz force $\boldsymbol{F}$ acting on the dipole in the electric field is given as

$$\boldsymbol{F} = q\left[\boldsymbol{E}(\boldsymbol{x}_1) - \boldsymbol{E}(\boldsymbol{x}_2) + \frac{d\boldsymbol{x}_1}{dt} \times \boldsymbol{B}(\boldsymbol{x}_1) - \frac{d\boldsymbol{x}_2}{dt} \times \boldsymbol{B}(\boldsymbol{x}_2)\right], \tag{4.1}$$

where $\boldsymbol{B}$ is the magnetic field, and $\boldsymbol{x}_1$ and $\boldsymbol{x}_2$ are positions of positive and negative charges, respectively ($\boldsymbol{x}_1 - \boldsymbol{x}_2 = \boldsymbol{d}_{\mathrm{q}}$). Since $|\boldsymbol{d}_{\mathrm{q}}|$ is small, Eq. (4.1) can be written as

$$\boldsymbol{F} = (\boldsymbol{p} \cdot \nabla)\boldsymbol{E} + \frac{d\boldsymbol{p}}{dt} \times \boldsymbol{B}. \tag{4.2}$$

Substituting $\boldsymbol{p} = \alpha_{\mathrm{p}}\boldsymbol{E}$ into Eq. (4.2) gives

$$\begin{aligned}
\boldsymbol{F} &= \alpha_{\mathrm{p}}\left[(\boldsymbol{E} \cdot \nabla)\boldsymbol{E} + \frac{d\boldsymbol{E}}{dt} \times \boldsymbol{B}\right] \\
&= \alpha_{\mathrm{p}}\left[\frac{1}{2}\nabla E^2 - \boldsymbol{E} \times (\nabla \times \boldsymbol{E}) + \frac{d\boldsymbol{E}}{dt} \times \boldsymbol{B}\right] \\
&= \alpha_{\mathrm{p}}\left[\frac{1}{2}\nabla E^2 - \boldsymbol{E} \times \left(-\frac{d\boldsymbol{B}}{dt}\right) + \frac{d\boldsymbol{E}}{dt} \times \boldsymbol{B}\right] \\
&= \alpha_{\mathrm{p}}\left[\frac{1}{2}\nabla E^2 + \frac{d}{dt}(\boldsymbol{E} \times \boldsymbol{B})\right].
\end{aligned} \tag{4.3}$$

The first term on the right-handed side of Eq. (4.3) is the contribution of the electric field gradient, corresponding to gradient force. The second term is the contribution of the Poynting vector, which corresponds to the radiation pressure directed at the light propagation. A focused beam can only trap an object if the gradient force (corresponding to $\alpha_{\mathrm{p}}\frac{1}{2}\nabla E^2$) is greater than the radiation pressure (corresponding to $\alpha_{\mathrm{p}}\frac{d}{dt}(\boldsymbol{E} \times \boldsymbol{B})$). When the objective lens with a high NA (numerical aperture) is used, the first term on the right-handed side of Eq. (4.3) becomes greater, and the trapping force is dominant, as shown in Fig. 4.2 [50].

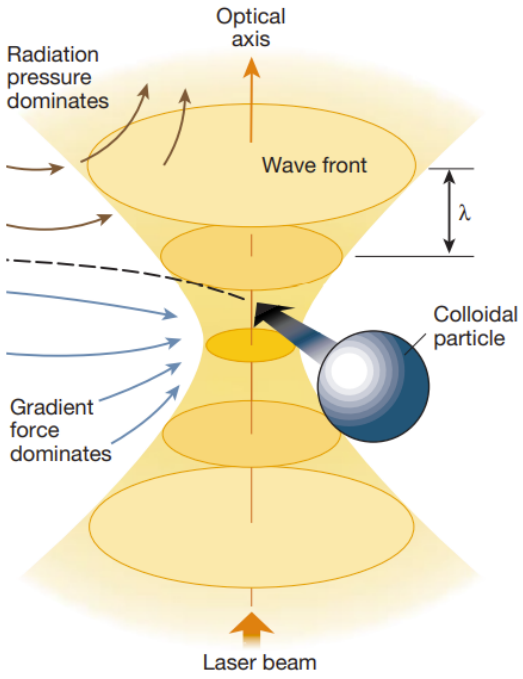

Figure 4.2. The intensity gradient in the beam attracts a small object such as a colloidal particle. The image was adapted from [50].

4.3 Materials and Methods

4.3.1 Materials

NLC droplets

5CB (TCI) and E7 (a mixture of 51 wt% 5BC (TCI), 25 wt% 7CB (Sigma-Aldrich), 16 wt% 8OCB (TCI), and 8 wt% 5CT (TCI)) were used as NLCs. The birefringence Δn of 5CB ($\Delta n = 0.159$) and E7 ($\Delta n = 0.192$) is different.

A mixture of E7 and ultrapure water (18.2 MΩ·cm) was stirred using a vortex mixer (Scientific Industries, Vortex-Genie 2) or a homogenizer (IKA, T25 digital ULTRA-TURRAX) to produce E7 droplets as shown in Fig. 4.3(a). The homogenizer and the vortex mixer were used to produce small droplets ($d < 3$ µm) and large droplets ($d > 3$ µm), respectively.

Solid birefringent particles

For preparation of solid birefringent particles, E7 and 15 wt% RM257 (Sigma Aldrich, a photo-polymerizable monomer)[30] were mixed with toluene (Wako) as shown in Fig. 4.3(b). After the toluene evaporated, the mixture (E7 and RM257) and ultrapure water were stirred in the same way as for NLC droplets to produce the droplets. The droplet dispersion was irradiated with ultraviolet light for 30 min to solidify the droplets via photopolymerization.

ChLC droplets

E7 and right-handed chiral dopant R-811 (Merck) were mixed with isopropanol (Wako) to prepare ChLC. After stirring with a magnetic stirrer (AS ONE, RSH-1DN) for 3 h, isopropanol was evaporated to produce the ChLC as shown in Fig. 4.3(c). ChLC droplets were prepared in the same way as for NLC droplets.

Sample cells

The droplet dispersion was sealed in a sample cell with a thickness of approximately 85 µm as shown in Fig. 4.3(d).

4.3.2 Methods

Optical system

Figure 4.4(a) shows our optical system. The laser beam was modulated in the following steps:

1. The laser beam (YLM-10-CP, IPG Photonics, wavelength of 1064 nm) passed through a 1/2 waveplate. The polarization of the beam can be controlled by the 1/2 waveplate.
2. The transmitted light was split into P- and S-polarized light by a polarising beam splitter (PBS). Since the light incident on the spatial light modulator (SLM, X10468-03, Hamamatsu) must be P-polarized, PBS was aligned to satisfy the above condition.
3. A pair of convex lenses enlarged the beam diameter to fit the SLM window.
4. SLM can control the wavefront of the incident beam. A pair of convex lenses changed the beam diameter to fit the entrance pupil of the objective lens.
5. A pair of 1/2 and 1/4 waveplates controlled the ellipticity angle φ and the orientation angle θ of the polarization ellipse of the trapping beam.
6. The transmitted beam was focused by a 100 $\times$ objective lens (Plan Fluor, Nikon, NA1.4).

At the focal point, LC droplets were trapped at 20 µm above the bottom of the cell to prevent the wall effect except when wall effect on LC droplet rotation was investigated. The laser power used at the focal plane was 7.5 mW, measured by a power meter (PM16-405, Thorlabs) unless otherwise noted. The temperature was set at 25^{o}C (298 K).

Rotation frequency analysis

Images of the rotating LC droplets were captured by a complementary metal-oxide-semiconductor (CMOS) camera (Orca-Flash 4.0, Hamamatsu, 2048 $\times$ 2048 pix^2) attached to an inverted optical microscope (Eclipse Ti, Nikon). The exposure time of the CMOS camera changed depending on the droplet size: 2 ms for tiny droplets ($d < 3$ µm) and 20 ms for large droplets ($d > 3$ µm). Since the polarizer and analyzer were removable, the image could be switched between bright-field and crossed-Nicols

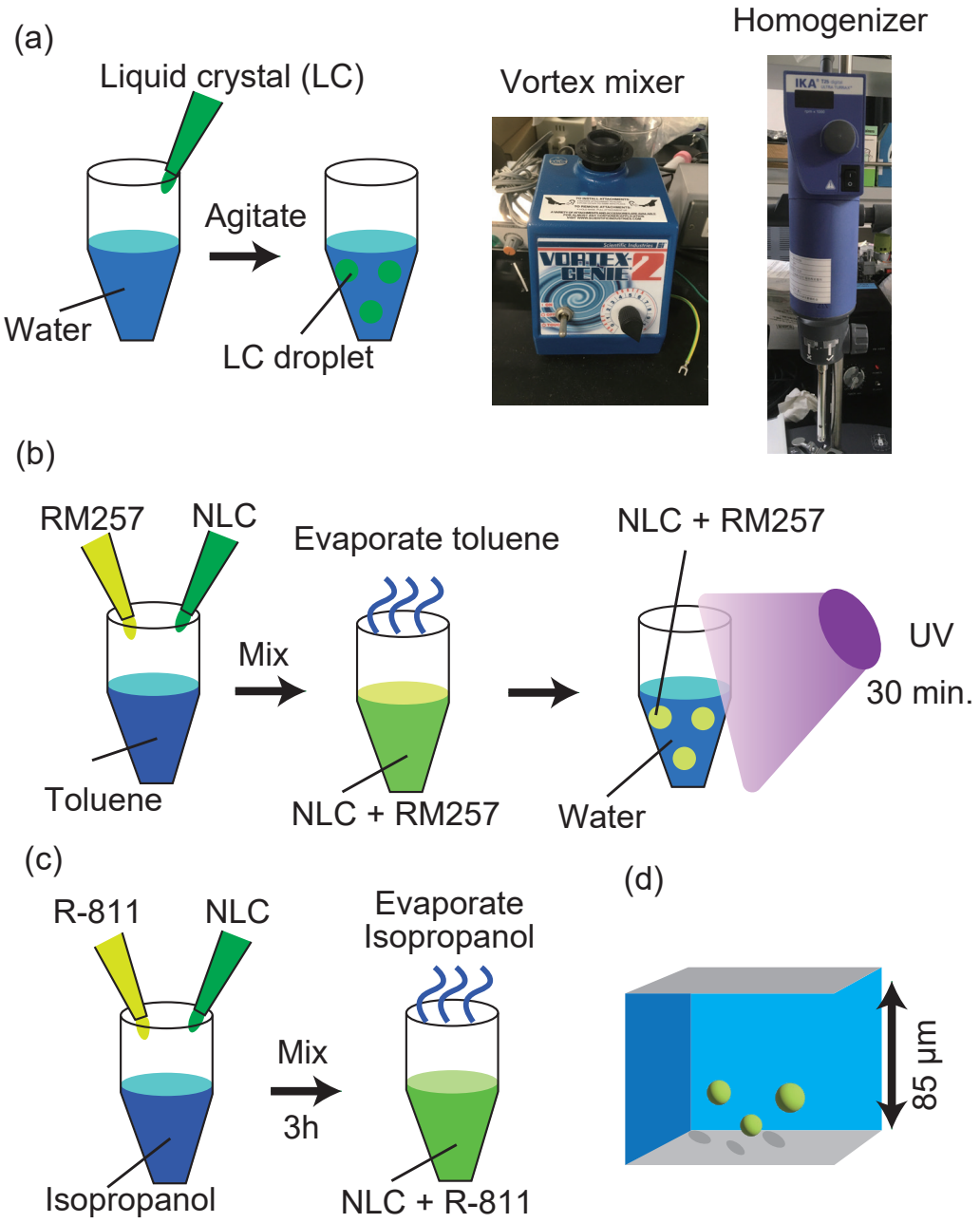

Figure 4.3. Method of droplet preparation. (a) Preparation for LC droplets. The mixture of LC and water was agitated with a vortex mixer or homogenizer. (b) Preparation for optically cured droplets. A photo-polymerizable monomer RM257 and NLC were mixed with toluene (left). Toluene was evaporated (middle). The droplets composed of RM257 and NLC were exposed to UV light for 30 min (right). (c) Preparation for ChLC. A chiral dopant R-811 and NLC were mixed with isopropanol (left). After stirring in a magnetic stirrer for 3 h, isopropanol was evaporated (right). (d) A Sample cell for droplet dispersion. Its thickness was 85 µm.

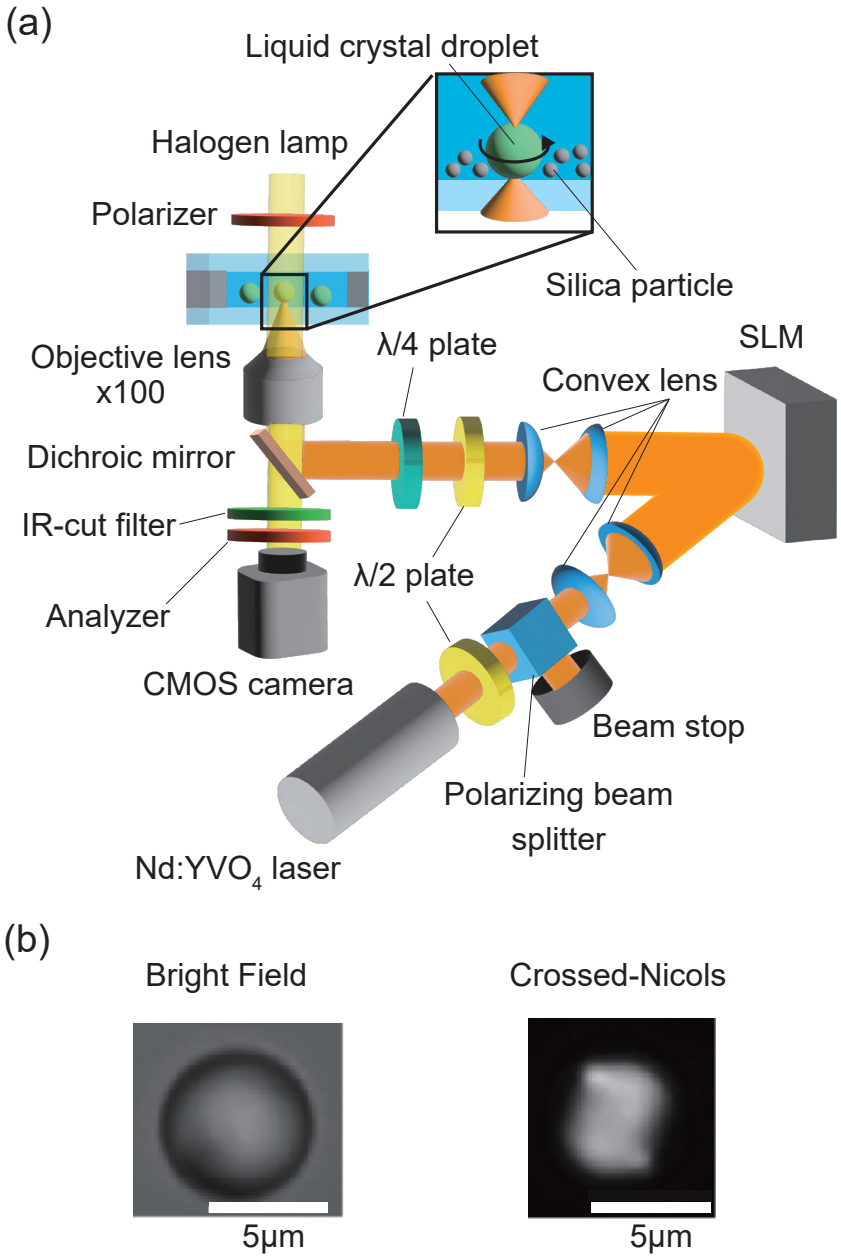

Figure 4.4. Experimental system. (a) Holographic optical tweezers and schematic of the sample cell. The small silica particles were added to NLC droplet dispersion for PIV measurement. (b) Microscope images of an NLC droplet under bright field (left) and crossed-Nicols polarizers (right).

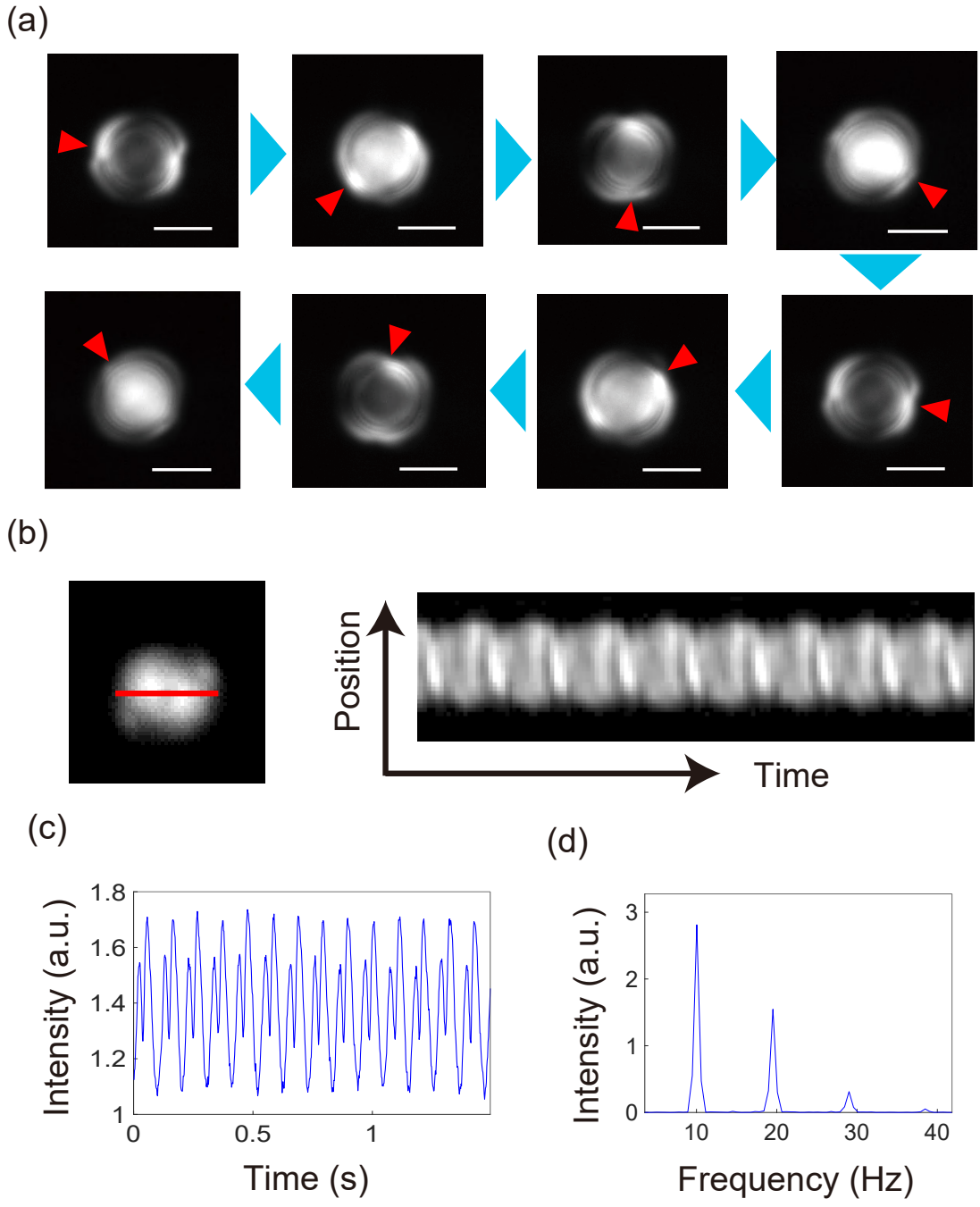

Figure 4.5. Rotation frequency analysis. (a) Images of a rotating NLC droplet under crossed-Nicols polarization. The red triangles point a defect in the droplet. The scale bar is 5 µm. (b) Image intensity along the red line was monitored (left). The spatiotemporal plot of the image intensity in the red line area (right). (c) The time evolution of the sum of the image intensity along the red line in (b). (d) Fourier-transformed data from the time evolution data of (c).

polarization as shown in Fig. 4.4(b).

The rotational motion could be monitored from the temporal change in the image intensity under crossed-Nicols polarization as shown in Fig. 4.5(a). Owing to the birefringence of LC droplets, droplet rotation can be detected [56]. Figure 4.5(b) shows a spatiotemporal plot of the image intensity in a horizontal line across the center of the droplet (corresponding to the red line in the left image of Fig. 4.5(b)). The image intensity along the horizontal line periodically changed as shown in the right image of Fig. 4.5(b). To determine rotation frequency ν of a droplet, the time evolution data of the sum of the image intensity along the line was measured and Fourier-transformed as shown in Figs. 4.5(c) and (d), respectively. The lowest frequency peak in Fig. 4.5(d) corresponded to either the 2ν or 4ν modulation of the rotation frequency, depending on the inner structure. We checked the videos to confirm whether the low-frequency peak was either 2ν or 4ν and finally determined ν.

4.4 Rotation of NLC droplets

4.4.1 Comparison between droplet and solid particle rotation

When a droplet exhibits stationary rotation with frequency ν, the optical torque Γ received from the laser beam is balanced by the viscous torque from the solution as [64],

$$\Gamma = \pi\eta\omega d^3, \tag{4.4}$$

where η is the viscosity of water, $\omega = 2\pi\nu$, d is the diameter of a particle. Since a rotating LC droplet is not a solid particle but a viscous droplet, we checked whether Eq. (4.4) is applicable to an NLC droplet. We compared ν of NLC droplets and their optically cured solid particles. Figure 4.6 shows the variation of ν with size d for the NLC droplets and cured solid particles. The fluidity of the NLC droplet had no significant effect on the rotational frequency because the viscosity of NLC was significantly higher than that of the surrounding water (the viscosity of E7 is approximately a few tens times higher than that of water [65]). Eq. (4.4) is applicable to the NLC droplets and allows optical torque Γ to be estimated.

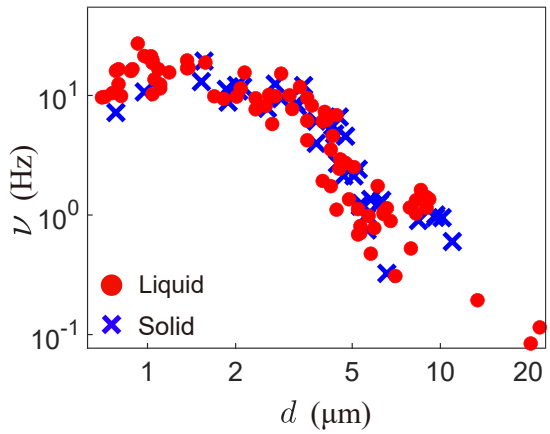

Figure 4.6. Variation of ν with d. The red dots and blue crosses correspond to the data for the droplet and the cured particle, respectively.

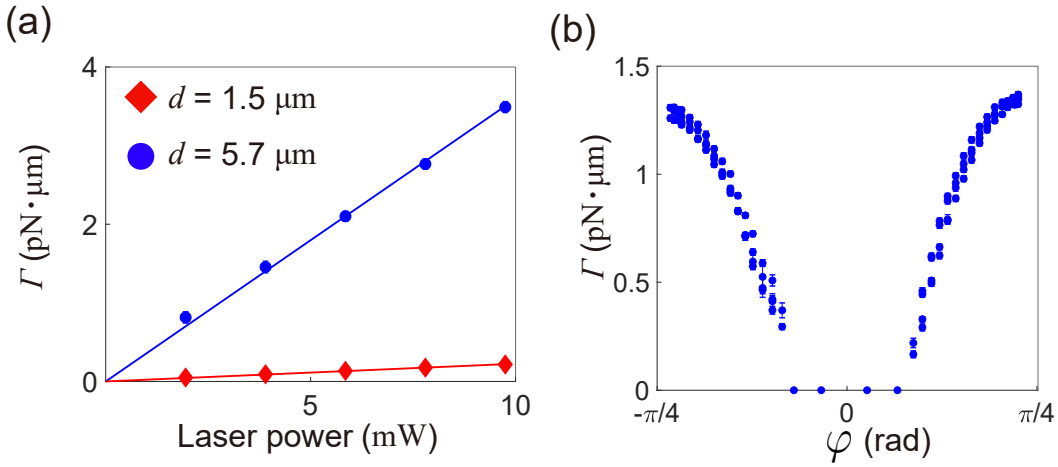

Figure 4.7. Variation of optical torque Γ with (a) laser power and (b) ellipticity angle of polarized laser beam φ. (a) Variation of Γ with laser power. The solid lines represent the linear-fitted lines. (b) Variation of Γ with φ. The diameter of a droplet was 5.5 μm.

4.4.2 Dependence of rotation on laser power and ellipticity angle of polarized laser beam

The relationship between Γ estimated by Eq. (4.4) and the laser power is depicted in Fig. 4.7(a). Γ linearly increased with increasing laser power from 1.9 to 9.4 mW. Γ also depends on the ellipticity angle φ of the laser beam as shown in Fig. 4.7(b). The linearly polarized beam corresponds to $\varphi = 0$, and the circularly polarized beam corresponds to $\varphi = \pi/4$. When the polarization of the trapping beam approached circular polarization above a certain critical value $|\varphi_c|$, the NLC droplet started to rotate, and ν increased with increasing $|\varphi|$. This behavior is explained by the waveplate effect [9, 14],

$$\Gamma = \frac{P}{f}\left[(1-\cos\Delta)\sin 2\varphi - \sin\Delta\cos 2\varphi \sin 2\theta\right], \tag{4.5}$$

where P is the laser power, f is the frequency of the trapping beam, Δ is the retardance expressed by $\Delta = 2\pi\Delta n d/\lambda$ (Δn is the birefringence, and λ is the wavelength of the trapping beam), θ is the angle between the major axis of the polarization ellipse and the optical axis of the object. Γ in Eq. (4.5) is proportional to P, and this is consistent with our experimental results (Fig. 4.7(a)). The first term on the right-hand side of Eq. (4.5) represents the contribution of the spin angular momentum, which rotates the object in the same direction as the rotation for the elliptical polarization. The second term represents the alignment effect along the major axis of the elliptical polarization, except if the incident beam is circularly polarized. The second term becomes maximum at $\theta = \frac{\pi}{4}$, $\sin\Delta\cos 2\varphi$, where Δ and φ are constant. Rotation occurs only if $|\varphi| > |\varphi_c|$ where $\tan 2\varphi_c = \frac{\sin\Delta}{1-\cos\Delta}$. This is consistent with our experimental result as shown in Fig. 4.7(b). Γ in Eq. (4.5) also depends on other parameters such as Δ which is related to the droplet size, and we examine the size dependence of Γ.

4.4.3 Size dependence of optical torque

Variation of Γ with diameter d of the NLC droplets was investigated under circularly polarized light ($\varphi = \frac{\pi}{4}$). The dependence of Γ on d is complex as shown in Fig. 4.8(a). We analyzed the size dependence by dividing it into two regions. For $d < 4$ µm, Γ increased monotonously with d. On the other hand, for $d > 4$ µm, oscillatory behavior of Γ was observed. There are four proposed origins of optical torque for

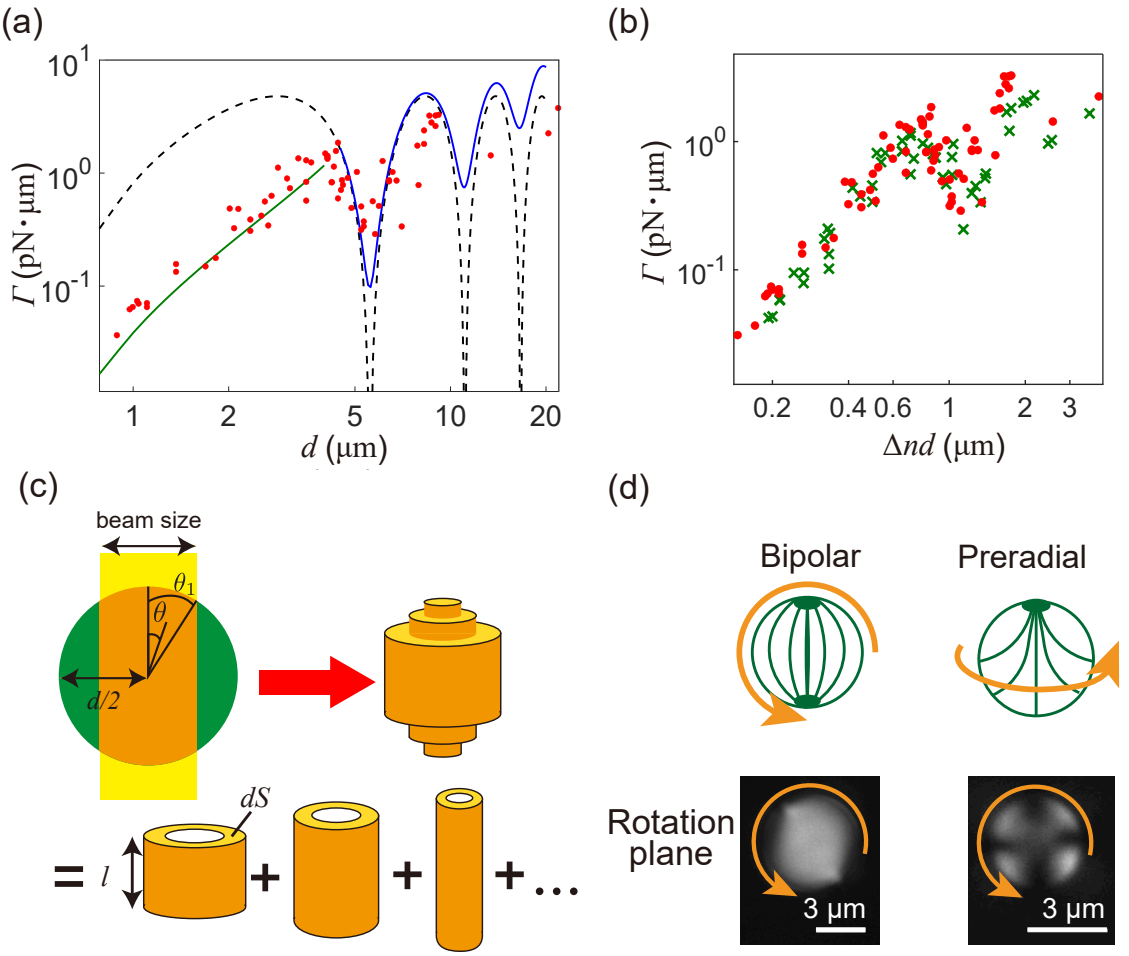

Figure 4.8. Size dependence of NLC droplets. (a) Variation of Γ with d of droplets. The dashed line is the best-fitted curve of Eq. (4.9). The green and blue lines are the best-fitted curves of Eq. (4.10) for $d < 4.5$ μm and $d > 4.5$ μm, respectively. (b) Variation of Γ with Δnd. The red dot and the green cross represent E7 ($\Delta n = 0.192$) and 5CB ($\Delta n = 0.159$), respectively. (c) Schematic of a trapped droplet. The orange region in the droplet represents the irradiated region by the incident beam. The irradiated region is decomposed into hollow cylinders. (d) Polarizing microscopic images of an NLC droplet under crossed-nicols polarizers and the schematics of molecular alignment. The molecular alignment within a smaller droplet is preradial, and that within a larger droplet is bipolar. The arrows indicate the rotation directions.

NLC droplets: the waveplate effect, light-scattering process, photon absorption, and light-induced Fréederickzs transition [14, 57].

In the waveplate effect, under circularly polarized light ($\varphi = \frac{\pi}{4}$), Eq. (4.5) reduces to

$$\Gamma(\varphi = \pi/4) = \frac{P}{f}\left(1 - \cos\Delta\right). \tag{4.6}$$

Light-scattering process, photon absorption, and light-induced Fréederickzs transition are briefly explained below.

- Light-scattering process [55]
  The transfer of angular momentum to an LC material can be achieved via light-scattering process. Light-scattering process originates from the phenomenon that the scattering angle depends on the polarization of light. Applied torque Γ_{LS} is expressed as

  $$\Gamma_{\mathrm{LS}} = \frac{PV\alpha n}{c}, \tag{4.7}$$

  where V is the volume of the object, c is the velocity of light in a vacuum, n is the average refractive index and α is the angle between the Poynting vector and wave vector.

- Photon absorption [55]
  Spin angular momentum can also be transferred via photon absorption. Under normal incidence of circularly polarized light with frequency f, the applied torque Γ_{A} is

  $$\Gamma_{\mathrm{A}} = \frac{V\alpha_{\mathrm{ab}}P}{f}, \tag{4.8}$$

  where α_{ab} is the absorption coefficient of a material.

- Light-induced Fréederickzs transition [66]
  This phenomenon is related to reorientation of LC molecules by light irradiation. The rotation induced by this phenomenon only occurs if irradiation power is strong enough (typical order is $1\mathrm{MW/cm^2}$). Theoretically, the angular frequency is non-linear with laser power.

Only the optical torque generated by waveplate effects expressed by Eq. (4.6) exhibits oscillatory dependence on droplet size, and its magnitude depends on the retardation of the droplet, $\Delta = 2\pi\Delta nd/\lambda$ [14, 57]. If the waveplate effect is dominant, oscillatory dependence can be scaled with Δnd for different LC droplets. The oscillatory behaviors in different NLCs, 5CB ($\Delta n = 0.159$) and E7 ($\Delta n = 0.192$)[67], can be scaled with Δnd as shown in Fig. 4.8(b). This also supports that the waveplate effect is the main contributor to Γ for large droplets.

The waveplate effect in a spherical birefringent particle was evaluated to quantitatively determine the variation of Γ with d. For steady-state rotation under circularly polarized light, the optical torque generated by the waveplate effect is expressed as Eq. (4.6), $\Gamma = (P/f)(1 - \cos\Delta)$. In our experiment, an LC droplet was partially irradiated as shown in Fig. 4.8(c). The irradiated area S was decomposed into hollow discs, and the birefringent sphere was decomposed into hollow cylinders. The optical axes of the cylinders were perpendicular to the center axis. The optical torque exerted on a hollow cylinder $d\Gamma$ was estimated based on the waveplate effect as $d\Gamma = (\mathscr{P}dS/f)(1 - \cos\Delta)$, where Δ is the retardance of the hollow cylinder ($\Delta = 2\pi\Delta nl/\lambda$, l is the height of the hollow cylinder), dS is the irradiated area of the hollow cylinder, and $\mathscr{P}$ is the power density of the laser ($\mathscr{P}S$ corresponds to P). We estimated the total torque Γ_{WP} by summing $d\Gamma$ as

$$\begin{aligned}\Gamma_{\mathrm{WP}} &= \int d\Gamma = \int_0^{\theta_1} \frac{\mathscr{P}}{f}\,(1-\cos\Delta)\,2\pi\left(\frac{d}{2}\right)^2 \sin\theta\cos\theta d\theta \\ &= \frac{\pi\mathscr{P}d^2}{2f}\left[\frac{1}{4}\,(1-\cos 2\theta_1) + \frac{1}{\Delta^2}\,(t_1\sin t_1 + \cos t_1 - \Delta\sin\Delta - \cos\Delta)\right], \quad (4.9)\end{aligned}$$

where θ_1 is the azimuth angle indicating the beam diameter (beam size $= d\sin\theta_1$) and $t_1 = \Delta\cos\theta_1$. The diameter of the beam is approximately $1.22\lambda/\mathrm{NA}$, where NA is the numerical aperture of the objective lens. A dashed line in Fig. 4.8(a) shows the best-fitted line of Eq. (4.9) for the experimental data with $\Delta n = 0.192$ [67] and the fitting parameter $\mathscr{P}$. For large droplets, the line captures the oscillatory behavior, but a discrepancy exists with the experimental data for small droplets. A possible reason for this difference was that only the waveplate effect was considered. Previous studies have suggested that both the waveplate effects and light-scattering process are significant for the rotation of NLC droplets [57]. However, the relative contribution of two effects has never been quantitatively mentioned. Since the optical torque depends

on the inner structure of the droplet, we observed molecular alignment within the LC droplets. The inner structure changed at approximately $d = 4$ µm. In larger droplets ($d > 4.5$ µm), the inner structure was bipolar (Fig. 4.8(d), left), and oscillatory behavior of Γ is observed in this region. On the other hand, for $d < 4.5$ µm, the inner structure changed to a preradial structure (Fig. 4.8(d), right).Such changes in the inner structure have also been reported in a previous study [61]. The critical size between the preradial and bipolar structures coincided with the size at which the dependence of Γ on d changed in our experiment. The power dependence in Fig. 4.7 is linear for both bipolar and preradial droplets. For a radial droplet, the nonlinear power dependence has been reported [14]. The linear dependence indicates that local optical deformation is not induced in a preradial droplet at lower power we used.

The optical torque Γ_{all} resulting from the waveplate effect Γ_{WP} and light-scattering process Γ_{LS} is expressed as

$$\Gamma_{\mathrm{all}} = A\Gamma_{\mathrm{WP}} + (1 - A)\Gamma_{\mathrm{LS}}, \tag{4.10}$$

where A is the ratio of Γ_{WP} to Γ_{LS} ($0 \leq A \leq 1$). α in Eq. (4.7) is derived from Δn and n (The calculation is presented in Appendix B). The experimental data are separately fitted with Eq. (4.10) at $d < 4.5$ µm and $d > 4.5$ µm, where $\mathscr{P}$ and A are the fitting parameters. The green and blue lines in Fig. 4.8(a) represent the best-fitted curves of Eq. (4.10) to data for $d < 4.5$ µm and $d > 4.5$ µm, respectively. For $d > 4.5$ µm, the waveplate effect was dominant because the optimal value of A was 0.997. This is consistent with the fact that the bipolar structure is anisotropic, and the waveplate effect is the main contributor to Γ. For $d < 4.5$ µm, A was 0.24, and the dominant contribution is light-scattering process. The preradial structure was more isotropic than the bipolar structure in the rotation plane. Therefore, the contribution of the waveplate effect became less significant than that of the light-scattering process. We estimated the energy efficiency, defined as the ratio of the power estimated by the fitting to that measured by the power meter at the focal plane. The energy efficiency was six times higher for bipolar droplets than for preradial droplets (9% and 1.5% for bipolar and preradial droplets, respectively). It indicates that the NLC droplet with a bipolar structure converted optical energy into mechanical energy more efficiently than that with a preradial structure.

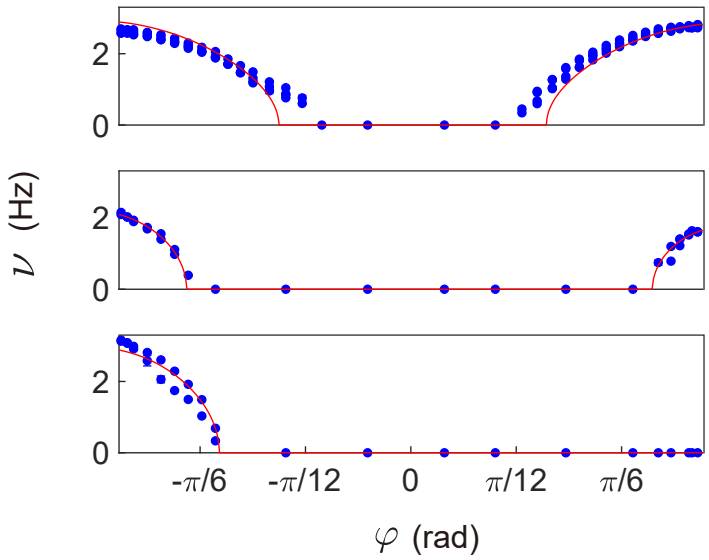

Figure 4.9. Variation of rotation frequency ν with ellipticity angle of polarized light φ with 10 mW laser power for NLC droplets and 25 mW for ChLC droplets. The R-811 concentrations are 0 wt% (top), 0.3 wt% (middle), and 1.0 wt% (bottom). The pitch length p are 6.0 µm (middle) and 5.2 µm (bottom). The diameters d of the droplets are 5.8 µm (top), 6.3 µm (middle, $d/p = 1.1$) and 6.4 µm (bottom, $d/p = 1.2$). The red lines are the best-fitted curve of Eq. (4.11).

4.5 Rotation of ChLC droplets

4.5.1 Dependence on ellipticity angle of incident beam

Based on the above discussion, the inner structure of the LC droplet is important for its rotational mechanism. To change the inner structure, we introduced helical modulation in the arrangement of LC molecules in NLC droplets by adding a chiral dopant. The amount of chiral dopant controls the optical chirality of ChLC droplets. Two droplets with different concentrations of the chiral dopant R-811 (0.3 and 1.0 wt%) were prepared. The change of rotation for the NLC and ChLC droplets was investigated by varying the ellipticity angle φ of the incident beam. Figure 4.9 shows the variation of rotation frequency ν with φ. For an NLC droplet (Fig. 4.9, top),

the dependence is almost symmetric with respect to $\varphi = 0$, and the direction of the circularly polarized beam determines the direction of the droplet rotation. On the other hand, the dependence on φ is asymmetric for the ChLC droplets (Fig. 4.9, middle and bottom), and ν for the beam with chirality opposite to ChLC decreases as the amount of chiral dopant increases. It has been reported that chiral solid particles selectively reflect circularly polarized light with the same direction of chirality as the particle [27, 37]. In the lower chirality region, such as our ChLC droplets, transmission and reflection of the circularly polarized beam co-occurred. When the torque transferred via reflection and transmission, ν is written as (derivation of ν for a ChLC droplet is presented in Appendix C), [37]

$$\nu = \frac{P\lambda}{4\pi^3 c\eta d^3}\mathrm{Re}\left[\left\{\sin^2 2\varphi\left[\left(1+\frac{R}{2}\right)-\left(1-\frac{R}{2}\right)\cos\Delta\right]^2 + R(1+\cos\Delta)\sin 2\varphi \right.\right.$$
$$\left.\left.\times\left[\left(1+\frac{R}{2}\right)-\left(1-\frac{R}{2}\right)\cos\Delta\right] + \frac{R^2}{4}(1+\cos\Delta)^2 - (1-R)\cos^2 2\varphi\sin^2\Delta\right\}^{\frac{1}{2}}\right], \tag{4.11}$$

where Re[A] represents the real part of A (In Eq. (4.11), A is either a real or a purely imaginary number) and R is the reflectance of the circularly polarized light in the same rotational direction as the chirality of the ChLC droplet.

The best-fitted lines obtained by Eq. (4.11) are in good agreement with the experimental data, as indicated by the solid lines in Fig. 4.9. The optimal value of R increases with increasing amounts of R-811 ($R = 0\%$, 4%, and 8% for 0 wt% [NLC], 0.3 wt%, and 1.0 wt% of R-811, respectively). The chiral dopant induces a helical structure, and the reflectance of circularly polarized light from the helical structure depends on the degree of chirality.

4.5.2 Size dependence of optical torque

The variation of Γ with diameter d of the ChLC droplets was measured under the irradiation of right-hand circularly polarized light as shown in Fig. 4.10(a). The R-811 concentrations of the three ChLC droplets used were 0.1, 0.7 and 4.6 wt%, respectively. The inner structure of ChLC droplets depends on the ratio of d to the pitch of the helical structure p [68]. In Fig. 4.10(b), Γ and d are normalized by its maximum value $\Gamma_{\max}$ and p, respectively. The overall dependency trend is consistent

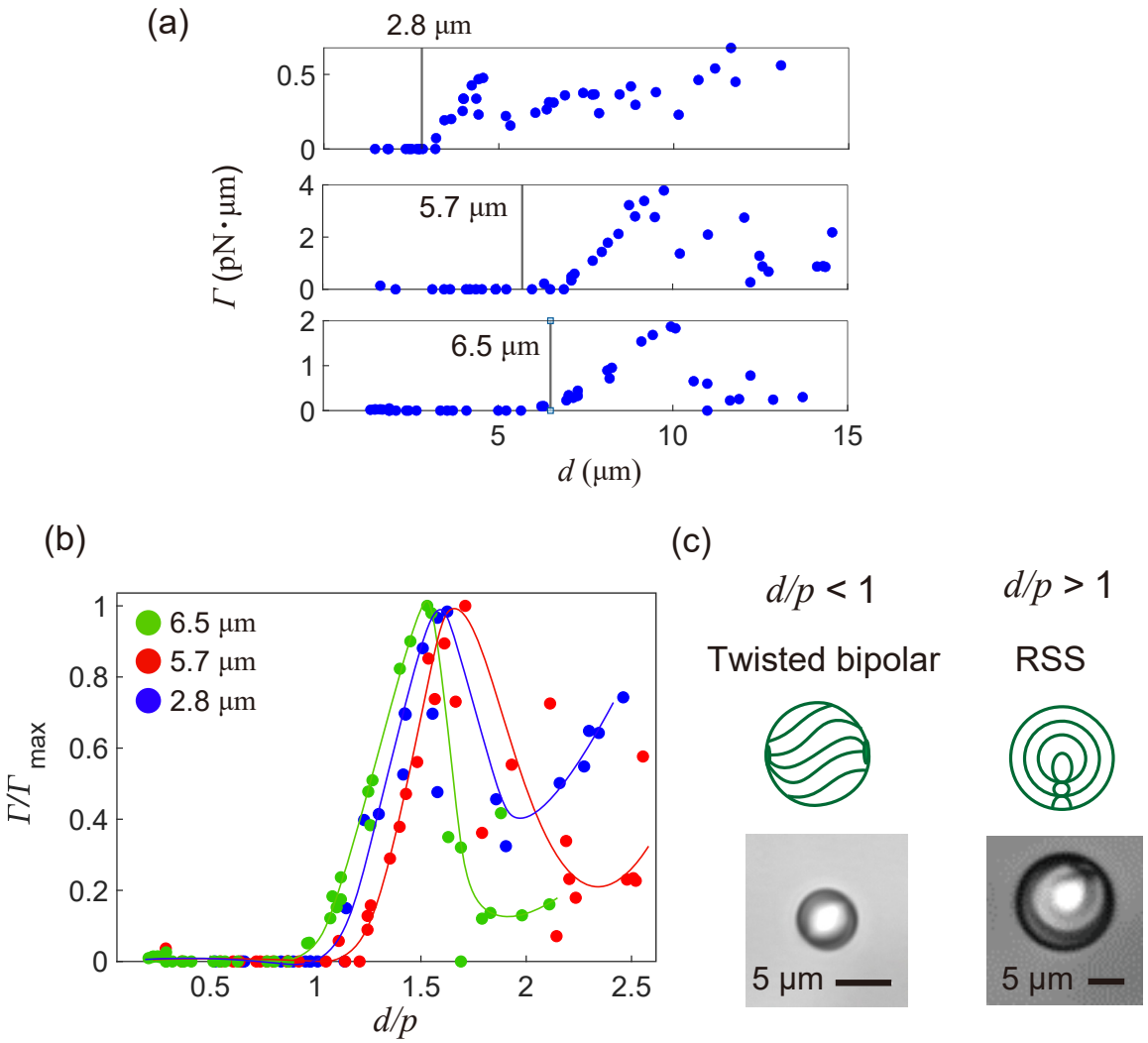

Figure 4.10. Size dependence of ChLC droplet rotation. (a) Variation of applied torque Γ with diameter d for three ChLC droplets with different amounts of R-811 (upper: 0.1 wt%, middle: 0.7 wt%, and lower: 4.6 wt%). The vertical line indicates pitch p of ChLC. 17.5 mW laser power was used. (b) Variation of scaled optical torque $\Gamma/\Gamma_{\max}$ with scaled diameter d/p. The solid lines are eye guides. (c) Bright field microscopic images and schematically shown molecular alignment of ChLC droplets with twisted bipolar structure and RSS. For $d/p < 1$, the inner structure is twisted bipolar; for $d/p > 1$, the inner structure is RSS.

for the three ChLCs. For $d/p < 1$, the ChLC droplets do not rotate within the laser power range we used. In this case, the inner structure of the droplet is twisted bipolar (Fig. 4.10(c), left) and acts as a waveguide [69]. Therefore, the droplet does not change the polarization of the incident light, and there is no transfer of angular momentum from the light to the droplet. For $d/p > 1$, the inner structure changes to a radial spherical structure (RSS) (Fig. 4.10(c), right), and the droplet rotates. In the RSS, the waveguide function disappeared and angular momentum transfer occurs. All plots have peaks at approximately the same position ($d/p \sim 1.5$). At this peak position, d approaches the Bragg wavelength np of the ChLC droplet, where n is the refractive index of approximately 1.503 for E7 [67].

4.6 Rotation of an NLC droplet near cell wall

Here, we consider deformation of an NLC droplet (bipolar) by pushing it against the cell wall to change the inner structure. Variation of ν with the distance from the cell wall was studied, as shown in Fig. 4.11(a). ν decreased as the droplet approached the bottom, and ν reached the minimum value when the droplet was in close contact with the wall of the cell ($z = z_0$, z: z-stage position). The particle-wall interaction increases the effective viscosity η_{eff} [64], resulting in this reduction. η_{eff} is approximately 1.1 times the viscosity in bulk. When $z - z_0 > d$ (d: droplet diameter) for the bottom wall case, the wall effect on ν was negligible. When the droplet was pressed against the bottom, ν increased rapidly, as shown in the blue and red dots of Fig. 4.11(a). In this case, the focal point was below the center height of the droplet, and the shape of the droplet was deformed. For the upper wall case, dependence of ν on the z-position relative to the wall is similar to the bottom wall case. Since the anisotropy of the inner structure of the droplet is critical for the transfer of angular momentum [57], we observed the inner structure of the deformed droplet under the crossed-Nicol state. The change in the inner structure depending on z-position was found as shown in Fig. 4.11(b). This result indicates that the deformation changes the birefringence. As an additional validation, the same measurement with a polymerized droplet which does not deform was performed. In the polymerized droplet case, ν decreased when the droplet was pressed as shown in the green dots of Fig. 4.11(a). This result suggests that the deformation is important to increase the optical torque transfer.

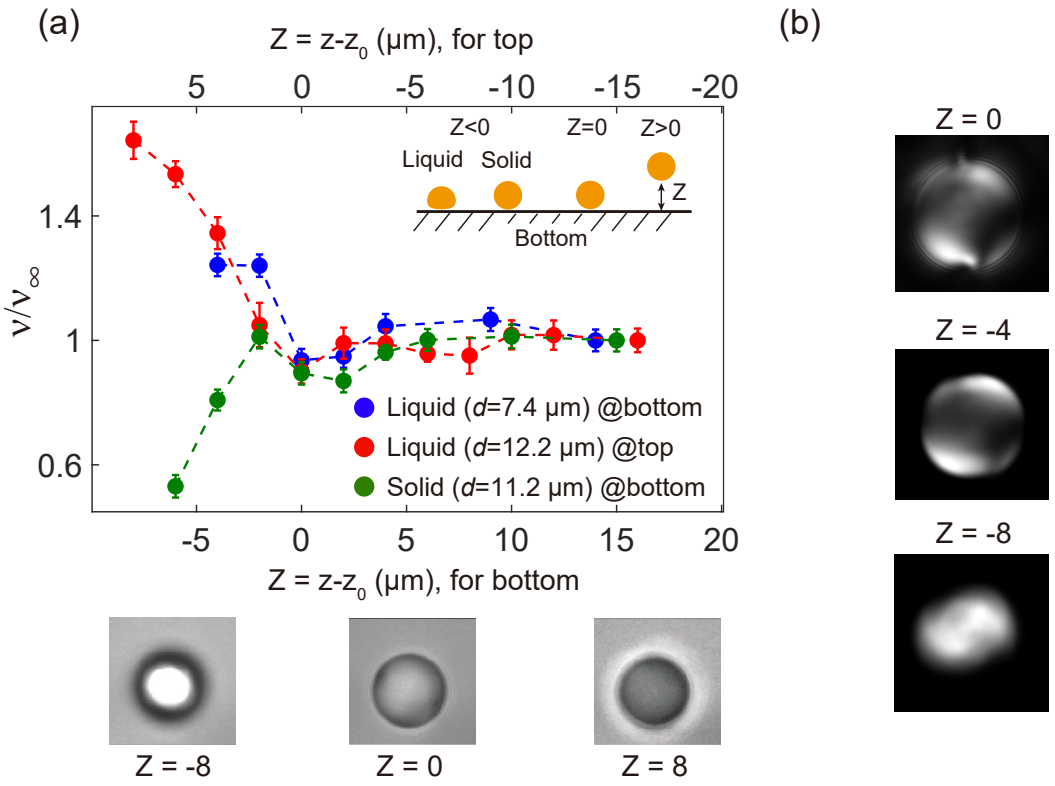

Figure 4.11. Variation of rotation frequency ν with the distance from cell wall. (a) z is the z-stage position, and z_0 is the position where the droplet touches the bottom of the cell. For bottom case, in region $Z = z - z_0 > 0$, Z is the gap between the cell and the droplet. In $Z < 0$, the droplet is attracted downward the bottom, resulting in deformation of its shape. For upper case, the droplet pushes against the wall in $Z > 0$, and $|Z|$ is the gap between the cell and the droplet in $Z < 0$. Bright-field microscopic images of the droplet for bottom wall case are shown in the bottom row. At $Z = -8$ μm, the white area corresponds to the region where the droplet touches the wall. (b) Images of the droplet at different z-position. The images were captured under the crossed-Nicol state.

4.7 Conclusion

We studied the rotation mechanism for NLC and ChLC droplets and evaluated energy transfer efficiency as shown in Fig. 4.12. For NLC droplets, the waveplate effect and the light-scattering process are the main contributions to the rotation. Above the critical diameter (about 4.5 μm in this study), the inner structure is bipolar and opti-

cally anisotropic. In this case, the main contribution is the waveplate effect, and the energy transfer efficiency of the bipolar droplet is approximately 9%. As the diameter of the NLC droplet decreases, the droplet loses optical anisotropy of the inner structure, and the inner structure becomes preradial, which is isotropic in the rotational plane. The energy transfer efficiency of the radial droplet is approximately 1.5%. In this case, the waveplate effect becomes weaker and the scattering process becomes dominant. In the case of ChLC droplets, transmissions and Bragg reflections due to the helical structure co-occur. Therefore, light angular momentum is transferred to the ChLC droplet via waveplate effect and Bragg reflection. The torque induced by the waveplate effect and Bragg reflection explains the rotational behavior influenced by the ellipticity angle φ. The diameter-to-pitch ratio d/p is important for its rotation behavior. For $d/p < 1$, the inner structure is twisted bipolar and acts as a waveguide. As a result, the transfer from the light to the ChLC droplet was minimal, and the ChLC droplet does not rotate. For $d/p > 1$, the inner structure changes to RSS, and the function of waveguide vanishes, resulting in rotation. Γ for ChLC droplets with $d/p < 1$ become the local maxmum value where d approches the Bragg wavelength np. The energy transfer efficiency of the ChLC droplet is less than 9%.

In the prepared droplets, bipolar droplets have the highest energy transfer efficiency. We calculate the energy transfer efficiency of a bipolar droplet reported by S. Juodkazis, *et al.* [56]. The calculated value is approximately 5%, and this value is slightly smaller than our value (9%). Since the droplet used for the calculation is small ($d = 2.5$ µm), the waveplate effect could become weak and decrease the energy efficiency. We also calculate the energy efficiency of cylindrical calcite reported by M. E. J. Friese, *et al.* [9]. The energy transfer efficiency is approximately 22% where the energy transfer efficiency is defined as the ratio of power estimated by waveplate effect for a cylinder to laser power. In the case of a spherical droplet, the retardance is different in the center and edge of the irradiation area. The transferred momentum cannot be maximized in all parts of the irradiation areas at the same time. On the other hand, in a cylinder, the retardance is the same in any part of the irradiation area because the thickness parallel to the traveling direction of light is the same. This geometry enables the maximization of transferred momentum in all parts of the irradiation area at the same time. This difference implies that the shape of birefringent object is important for the energy transfer efficiency.

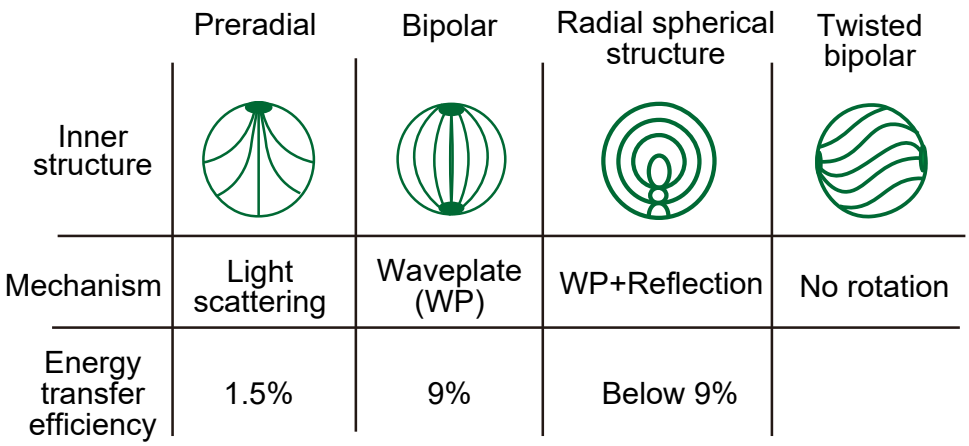

Figure 4.12. Summary of the relationship between the inner structure of the LC droplets and the rotation mechanism.

This study reveals that the waveplate effect efficiently transfers torque from light to LC droplets. Furthermore, comparison with the other studies implies the significance of the shape to the energy efficiency in the waveplate effect. Our findings lead to the design of microscale motors with high energy efficiency from light to kinetic energy.

Chapter 5
Rotation of an NLC droplet in viscous fluids

5.1 Introduction

Microscale flow plays an important role in a variety of biological phenomena [70, 71] and for particle separation in microfluidic devices [72]. For instance, microscale flow caused by the rotation of bacterial flagella leads to a turbulence-like collective motion, known as bacterial turbulence [71]. A particle moving in a linear microfluidic channel is subjected to a force perpendicular to the direction of movement due to the difference in the flow velocity at the top and bottom of the particle. Since this force depends on the particle size, flowing particles through the channel can be separated according to their sizes [73]. Analyzing and controlling microscale flows is important for understanding the collective motion of microorganisms and for developing cell-separation techniques. In many cases, since microscale flows are controlled by changing the geometry of a microfluid device, we need to fabricate the device according to research objectives [74]. Furthermore, these systems are often placed in viscous or viscoelastic fluids. These systems are often placed in viscous or viscoelastic fluids. Examples include bacteria in polymer solutions or cells in blood [75, 76]. Therefore, elucidating the flow field of viscous fluids is important for understanding the behavior of microparticles in real environment.

Optical tweezers is a fascinating tool for micromanipulation because they enable noncontact and nondestructive control of the positions of micro-objects [78]. As described in Section 4, NLC droplets are useful materials for creating and controlling microscale flows because their rotation can be controlled by optical tweezers. The advantages of using an NLC droplet are the ease of droplet fabrication and the ability to control droplet size at the microscale [30]. Furthermore, combination of the holographic optical tweezers (HOT) and the NLC droplet enables complex control of microscale flow [78].

In this study, the flow field induced by the rotation of an NLC droplet under a circularly polarized light was investigated by varying the viscosity of the surrounding solution to understand the effect of viscosity on rotation. For this purpose, the

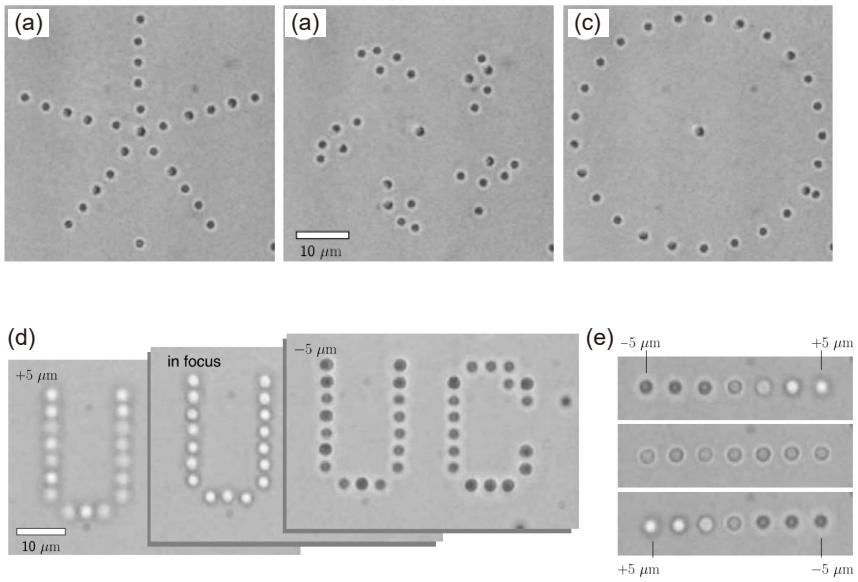

Figure 5.1. Micromanipulation with Holographic Optical Tweezers (HOT). Two-dimensional position control of colloidal silica spheres in a star-like pattern (a), sail-wing pattern (b) and circle (c). (d, e) Three-dimensional position control of the silica spheres.The images in (d) show trapped silica particles at different positions relative to the focal position. (e) Seven spheres were trapped at different positions relative to the focal position [77].

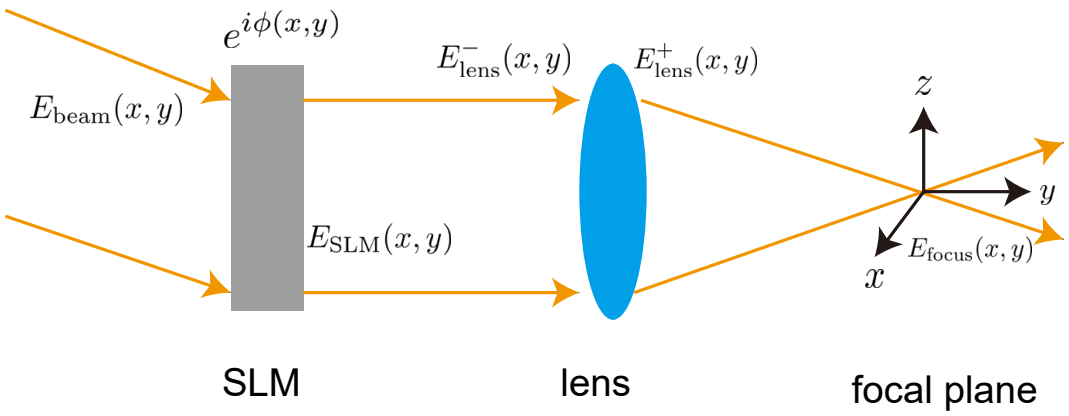

Figure 5.2. Principle of HOT. SLM modulates the incoming beam E_{beam} into E_{SLM} changing its phase by $e^{i\phi}$. E^{-}_{lens} and E^{-}_{lens} represent the electric field before and just after the lens, respectively. E_{focus} donates the electric field at the focal plane.

rotational frequency of the droplet and the flow velocity around the droplet were simultaneously measured. By comparing the rotation frequency with the magnitude of the induced flow velocity, the experimental results are discussed. We constructed a micro-viscometer using an optically trapped rotating droplet. Subsequently, hydrodynamic interaction between two rotating droplets was studied using HOT. Further, we demonstrated complex control of microscale flow.

5.2 Holographic optical tweezers (HOT)

We will explain the operating principle of HOT discussing how to modulate the wavefront of the beam to obtain the appropriate trap pattern [79]. An SLM receives a paraxial beam with transverse profile $E_{\mathrm{beam}}(x,y)$ as shown in Fig. 5.2. SLM modulates phase of the incoming beam by a phase factor $e^{i\phi(x,y)}$. Just after the SLM, the electric field $E_{\mathrm{SLM}}(x,y)$ is expressed as

$$E_{\mathrm{SLM}}(x,y) = e^{i\phi(x,y)} E_{\mathrm{beam}}(x,y). \tag{5.1}$$

Electric field of the entrance pupil of the lens $E^{-}_{\text{beam}}(x,y)$ is obtained using the Fresnel diffraction integral [79],

$$\begin{aligned} E^{-}_{\text{lens}}(x,y) &= \frac{e^{ik_0 l_\text{f}}}{i\lambda_0 l_\text{f}} \iint_{-\infty}^{+\infty} E_{\text{SLM}}(x',y') e^{i\frac{k_0}{2l_\text{f}}\left[(x-x')^2+(y-y')^2\right]} dx'dy' \\ &= \frac{e^{ik_0 l_\text{f}}}{i\lambda_0 l_\text{f}} e^{i\frac{k_0}{2l_\text{f}}\left(x^2+y^2\right)} \iint_{-\infty}^{+\infty} E_{\text{SLM}}(x',y') e^{i\frac{k_0}{2l_\text{f}}\left(x'^2+y'^2\right)} e^{-i\frac{k_0}{l_\text{f}}\left(xx'+yy'\right)} dx'dy', \end{aligned} \tag{5.2}$$

where k_0 is the vacuum wavenumber, λ_0 is the vacuum wavelength and l_f is the focal length of the lens and the superscript '-' indicates that we consider the beam just before the lens. Assuming that the diameter of the lens is much larger than the size of the beam and using the thin lens approximation, the effect of the lens is to add a quadratic phase factor to the beam,

$$E^{+}_{\text{lens}}(x,y) = E^{-}_{\text{lens}}(x,y) e^{-i\frac{k_0}{2l_\text{f}}\left(x^2+y^2\right)}, \tag{5.3}$$

where the superscript '+' indicates that we consider the beam just after the lens. Subsequently,

$$E^{+}_{\text{lens}}(x,y) = \frac{e^{ik_0 l_\text{f}}}{i\lambda_0 l_\text{f}} \iint_{-\infty}^{+\infty} E_{\text{SLM}}(x',y') e^{i\frac{k_0}{2l_\text{f}}\left(x'^2+y'^2\right)} e^{-i\frac{k_0}{l_\text{f}}\left(xx'+yy'\right)} dx'dy'. \tag{5.4}$$

To obtain the electric field at the focal plane E_{focus}, the Fresnel diffraction formula is applied to $E^{+}_{\text{lens}}(x,y)$, obtaining

$$E_{\text{focus}}(x,y) = \frac{e^{ik_0 l_\text{f}}}{i\lambda_0 l_\text{f}} e^{i\frac{k_0}{2l_\text{f}}\left(x^2+y^2\right)} \iint_{-\infty}^{+\infty} E^{+}_{\text{lens}}(x',y') e^{i\frac{k_0}{2l_\text{f}}\left(x'^2+y'^2\right)} e^{-i\frac{k_0}{l_\text{f}}\left(xx'+yy'\right)} dx'dy'. \tag{5.5}$$

Substituting Eq. (5.3) into Eq. (5.5) gives

$$E_{\text{focus}}(x,y) = \frac{e^{ik_0 l_\text{f}}}{i\lambda_0 l_\text{f}} e^{i\frac{k_0}{2l_\text{f}}\left(x^2+y^2\right)} 4\pi^2 \hat{E}^{-}_{\text{lens}}(f_x,f_y), \tag{5.6}$$

where $f_x = x/(\lambda l_\text{f})$, $f_y = y/(\lambda l_\text{f})$ and

$$\hat{E}^{-}_{\text{lens}}(f_x,f_y) = \frac{1}{4\pi^2} \iint_{-\infty}^{+\infty} E^{-}_{\text{lens}}(x,y) e^{-i2\pi(f_x x+f_y y)} dxdy \tag{5.7}$$

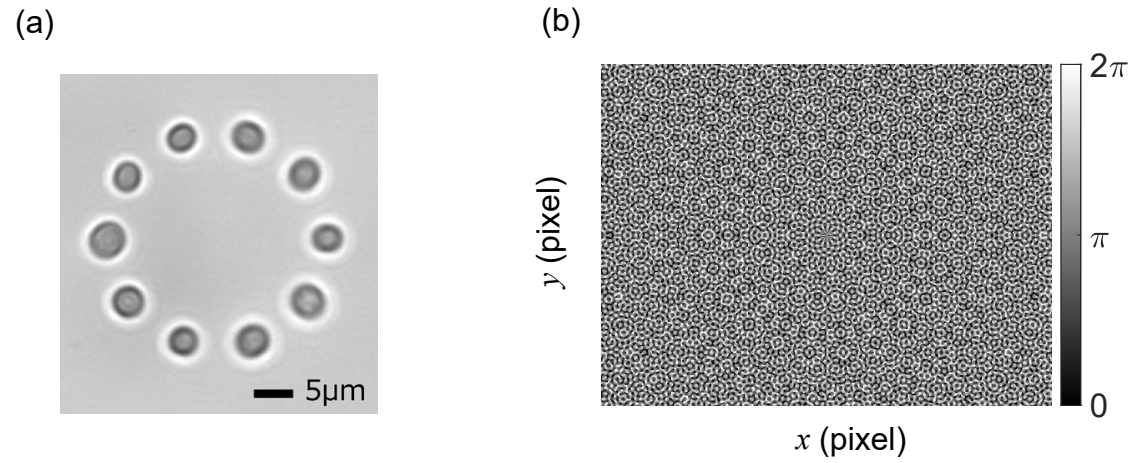

Figure 5.3. Multipoint trap by HOT. The trapped particle (a) and the phase mask displayed on SLM (b).

is the Fourier transform of $E^{-}_{\mathrm{lens}}(x, y)$. Here, $\hat{A}(f_x)$ is the Fourier transform of $A(x)$, which is defined as [79]

$$\hat{A}(f_x) = \frac{1}{2\pi} \int_{-\infty}^{+\infty} A(x) e^{-i2\pi f_x x} dx. \tag{5.8}$$

The relationship between $\hat{E}^{-}_{\mathrm{lens}}(f_x, f_y)$ and $\hat{E}_{\mathrm{SLM}}(f_x, f_y)$ is obtained by the Fourier transform of Eq. (5.2) as

$$\hat{E}^{-}_{\mathrm{lens}}(f_x, f_y) = e^{ik_0 l_{\mathrm{f}}} e^{-i\pi\lambda l_{\mathrm{f}}\left(f_x^2 + f_y^2\right)} \hat{E}_{\mathrm{SLM}}(f_x, f_y). \tag{5.9}$$

Substituting Eq. (5.9) into Eq. (5.6) gives

$$E_{\mathrm{focus}}(x, y) = \frac{e^{2ik_0 l_{\mathrm{f}}}}{i\lambda_0 l_{\mathrm{f}}} 4\pi^2 \hat{E}_{\mathrm{SLM}}(f_x, f_y). \tag{5.10}$$

Eq. (5.10) means that the electric field at the focal plane is the Fourier transform of the electric field at the SLM plane. Controlling phase $\phi(x, y)$ with SLM allows manipulation of the spatial trap pattern. The $\phi(x, y)$ is derived from the inverse Fourier transform of the desired spatial intensity pattern. Fig. 5.3(a) shows trapped particles using the phase mask $\phi(x, y)$ of Fig. 5.3 (b)

5.3 Materials and methods

5.3.1 Materials

NLC droplets

E7 droplets with diameters ranging from 4 to 12 µm were used. The inner structure of the droplets was bipolar. The preparation of E7 and droplets was the same as in Section 4. Optically cured particles were also prepared in the same way as in Section 4.

5.3.2 Methods

Optical system

Although the optical system used was the same as that described in section 4, we controlled a spatial light modulator (SLM) to manipulate the spatial intensity pattern in the focal plane, which enables multiple trapping as shown in Fig. 5.1 [77]. The temperature was set at 25^oC (298 K).

Image acquisition

Images of the droplets were captured every 10 ms using a complementary metal-oxide-semiconductor (CMOS) camera (OrcaFlash 4.0, Hamamatsu, 2048×2048 pix^2) attached to an inverted optical microscope (Eclipse Ti, Nikon). The rotation frequency of the droplet was estimated from the temporal change in the image intensity captured by crossed-Nicols polarizers in the same way as in section 4.3.2. Images captured under the bright field were used for the particle image velocimetry (PIV) analysis.

Particle image velocimetry (PIV)

0.15 wt% silica particles (Sicastar-greenF, Micromod) with a diameter of 500 nm were used as tracer particles to visualize flow fields. Since the silica particle was sedimented at the bottom, rotating droplets were set at the bottom of the cell. The captured images were analyzed using the PIV lab in MATLAB to calculate the flow field [80]. In the PIV analysis, the velocity field was estimated by cross-correlation in a pair of two consecutive images. The recorded movie for PIV analysis contained

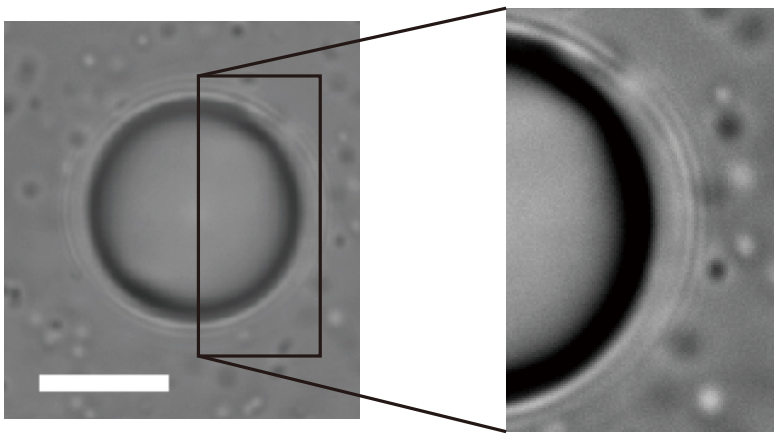

Figure 5.4. Microscopic image of an NLC droplet under bright field. The fringe pattern hides the probe particles near the droplet. The scale bar is 5 µm.

500 frames and 499 pairs were analyzed. The calculated velocity fields (499 results) were averaged to reduce noise. It was difficult to measure the flow field in the vicinity of the droplet surface due to the fringe pattern appearing near the droplet surface and the interrogation window problem, as shown in Fig. 5.4. The used interrogation window was 2.0 µm.

5.4 Flow field induced by an NLC droplet rotation

A bipolar NLC droplet receives optical torque Γ from circularly polarized beam via waveplate effect, $\Gamma \propto E^2(1 - \cos\Delta)$, where E is the electric field of the beam and Δ is the retardance, as described in Section 4. Angular frequency of the rotating droplet ω is determined by balance between Γ and viscous resistance torque from a surrounding fluid [81],

$$\Gamma = 8\pi\eta a^3\omega, \tag{5.11}$$

where a is the radius of the droplet and no-slip boundary condition is assumed. The induced flow fields by the rotating droplet were measured in water and a 60 wt% aqueous glycerol solution by PIV as shown in Figs. 5.5(a) and (b). Both flow fields were similar, except for the magnitude of the flow velocity. The tangential component of induced flow velocity v_θ at distance r from the center of the rotating particle is expressed as [81]

$$v_\theta = \frac{a^3}{r^2}\omega, \tag{5.12}$$

where a solid spherical particle and no-slip boundary condition are assumed. We took the radial average of v_θ and compared the measured v_θ with the theoretical value estimated by Eq. (5.12). The measured dependence of v_θ on r agrees well with the theoretical ones calculated by Eq. (5.12), as shown in Fig. 5.5(c). This agreement confirms that the droplet behaved as a solid particle in water. This is because the viscosity of E7 is several tens of times higher than that of water, as mentioned in Section 4. In contrast, in the 60 wt% aqueous glycerol solution, the measured v_θ were smaller than the theoretical values estimated by Eq. (5.12) as shown in Fig. 5.5(d). Before discussing the possible reasons for this discrepancy, we consider changes of Γ between water and the glycerol solution and the wall effect.

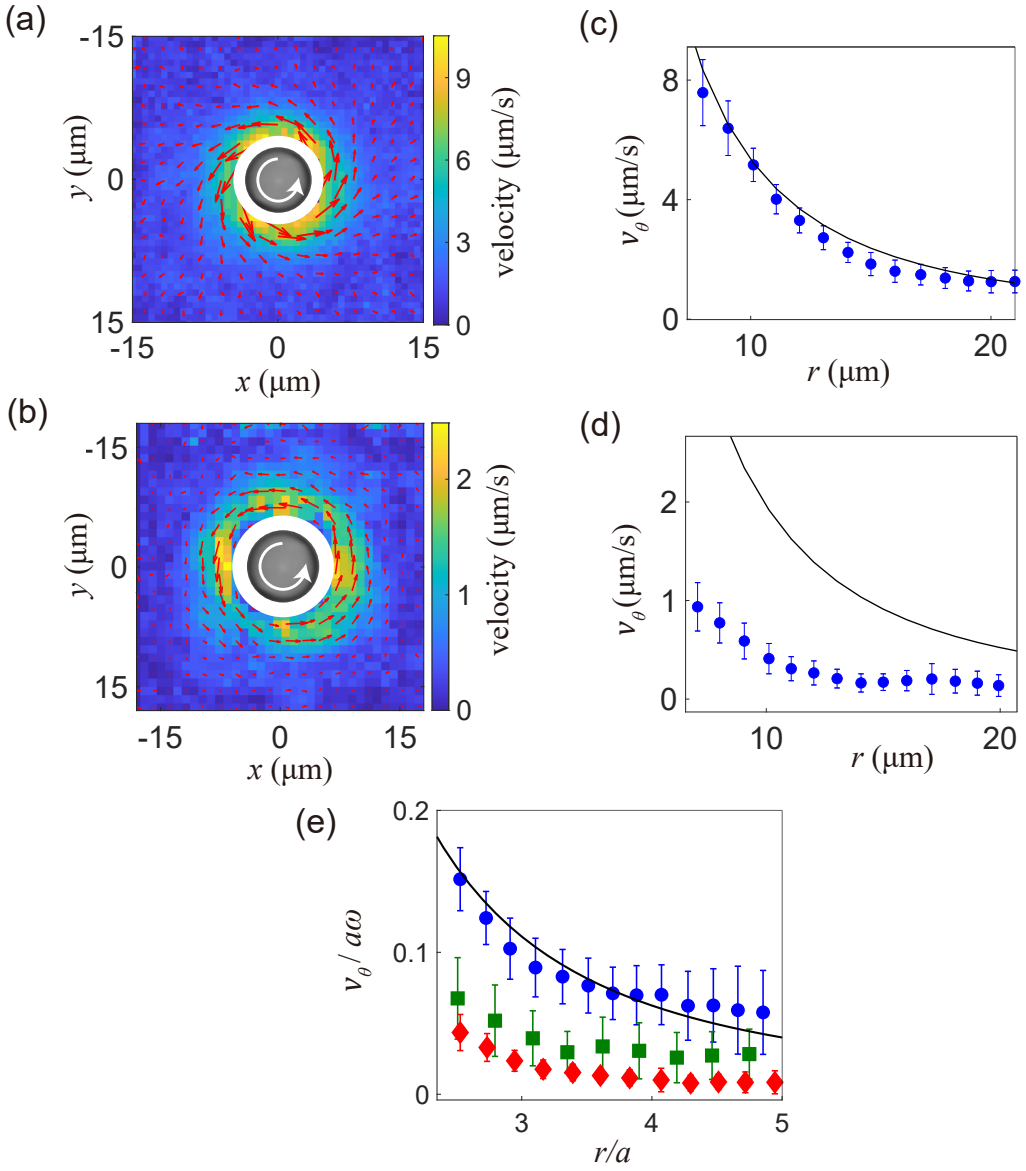

Figure 5.5. Induced flow field by a rotating NLC droplet. (a, b) Flow field in water (a) and a 60 wt% aqueous glycerol solution (b). The laser power used was 28.2 mW. The white circle represents the unmeasurable area by PIV, and a microscopic image of an NLC droplet was placed at the center of the white circle. Radius a in (a) is 3.4 μm and (b) is 4.5 μm. (c, d) Variation of the azimuthal component of induced flow velocity v_θ with the distance r from the droplet center in water (c) and in the glycerol solution (d). The solid line represents theoretical values calculated by Eq. (5.12). (e) Variation of the scaled azimuthal component of induced flow velocity $v_\theta/a\omega$ with the scaled distance r/a from the droplet center: a droplet in water (filled blue circles) corresponding to (a), a droplet in the 60 wt% aqueous glycerol solution (filled red diamonds) corresponding to (b), an optically cured particle ($a = 3.6$μm) in 60 wt% aqueous glycerol solution (filled green squares) and theoretical values calculated by Eq. (5.12) (solid line).

First, the effect of changes in the refractive index of the solution on Γ is examined. The refractive index of the solution depends on the mass concentration of glycerol C_{m}. The refractive indices of water ($C_{\mathrm{m}} = 0$ wt%) and the aqueous glycerol solution ($C_{\mathrm{m}} = 60$ wt%) are 1.33 and 1.42, respectively [82]. The amplitude of the electrical field inside droplet E_{d} is expressed by the Fresnel equation under normal incidence as follows,

$$E_{\mathrm{d}} = \frac{2n_1}{n_1 + 2n_2} E_{\mathrm{in}}, \tag{5.13}$$

where E_{in} is the incident electric field and n_1 and n_2 are the refractive indices of the solution and liquid crystal, respectively ($n_2 = 1.50$ for E7 [67]). The variation in n_1 changes the amplitude of the electric field. Since optical torque is proportional to the square of the electric field E_{d}^2 [57], Γ at $C_{\mathrm{m}} = 60$ wt% increases by 6 % relative to Γ at $C_{\mathrm{m}} = 0$ wt% with a fixed laser power. However, the change in Γ resulting from the variation of the refractive index is relatively small.

Next, the wall effect on the tracer particles was considered because the particles were settled down near the cell bottom. Effective viscosity η_{eff} is expected to increase due to the particle-wall interaction [64]. η_{eff} was estimated by measuring the trajectory of Brownian particles near the bottom (a detailed method is presented in Appendix D). The calculated η_{eff} at $C_{\mathrm{m}} = 60$ wt% is 9.8 mPa·s and this is larger than literature one in bulk η_0 (8.8 mPa·s) [83]. Due to the increase in effective viscosity, the velocity of the particle near the bottom is reduced by about 11%. The measured velocity from PIV was corrected by multiplying $\eta_{\mathrm{eff}}/\eta_0$ to the measured velocity to remove the influence of the velocity reduction due to the wall effect. In addition, the solution viscosity relative to the droplet increased because the rotating droplet was also placed at the bottom. Experimental observations show that the viscosity at the bottom is approximately 1.1 times the bulk viscosity as shown in Fig. 4.11.

We consider the possible origin of the discrepancy between the results in water and those in the aqueous glycerol solution to be a violation of the assumptions in Eq. (5.12): a solid particle and the no-slip boundary condition. There are possibilities of fluidization inside the droplet and slippage at the droplet surface. The disagreement between the direction of LC director and flow velocity inside the LC due to fluidity of LC has been reported in a rotating cholesteric LC pillar [84]. To verify these possibilities, we used optically cured particles that exhibited no internal fluidization

in water [30]. We compared $v_\theta/a\omega$ for the droplet and a cured particle as shown in Fig. 5.5(e), because $v_\theta/a\omega$ can be scaled by r/a as in Eq. (5.12). The average ratio of the measured v_θ for the droplet to the estimated one by Eq. (5.12) was 0.21, and this reduction can be attributed to both slip and fluidization inside the droplet. On the other hand, the ratio of the cured particle was 0.4. In this case, only the slip contributed to this decrease. The viscous resistance of a droplet is $\frac{2\eta_\mathrm{s}+3\eta_\mathrm{d}}{3(\eta_\mathrm{s}+\eta_\mathrm{d})}$ times smaller than that of a solid particle where η_d and η_s are the viscosities of the liquids inside and outside the droplet, respectively [85]. Even in $C_\mathrm{m} = 60$ wt%, the factor, $\frac{2\eta_\mathrm{s}+3\eta_\mathrm{d}}{3(\eta_\mathrm{s}+\eta_\mathrm{d})}$, is 0.94 where $\eta_\mathrm{d} = 40$ mPa·s and $\eta_\mathrm{d} = 8.8$ mPa·s [65, 83]. This reduction (0.06) due to fluidization is relatively small to the overall reduction of the flow velocity. We considered that the remaining difference between the droplet and the cured one was attributed to changes in the slip condition arising from the polymerization. In both cases, the surface slip appeared to be a dominant contributor to the reduction in the induced flow velocity. The azimuthal component of the induced flow velocity $v_{\theta\mathrm{s}}$ under the slip boundary condition (Fig. 5.6(a)) is written as [19],

$$v_{\theta\mathrm{s}} = \frac{\beta a}{\beta a + 3\eta}\frac{a^3}{r^2}\omega, \tag{5.14}$$

where β is the slip coefficient and there is no particle-wall interaction. The situation is shown schematically in Fig. 5.6. The corrected measured data (multiplying η_eff/η_0 by the measured velocity) was used by removing the influence of the particle–wall interaction. The measured dependence of corrected v_θ on r in the glycerol solution at $C_\mathrm{m} = 60$ wt% can be fitted using Eq. (5.14) with fixed ω and the fitting parameter β as shown in Fig. 5.6(b). The optimal value of β is 3.50×10^3 N·s/m^3, and the corresponding slip velocity is 14.6 µm/s. In this study, slip velocity v_slip is defined as the difference between surface velocity of the droplet and flow velocity at the surface, $v_\mathrm{slip} = a\omega - v_\mathrm{slip}(a)$, as schematically shown in Fig. 5.6(a). This value ($v_\mathrm{slip} = 14.6$ µm/s) is comparable to the slip velocity reported for microchannels (from 30 to 50 µm/s [86]). The variation of v_θ at the droplet surface with $a\omega$ was also measured by changing the power of the incident beam as shown in Fig. 5.6(c). The experimental results are in good agreement with the theoretical equation $v_{\theta\mathrm{s}}(a) = \frac{\beta a}{\beta a+3\eta}a\omega$, which is a modified version of Eq. (5.14) with the same β as in Fig. 5.6(b), $\beta = 3.50 \times 10^3$ N·s/m^3. This agreement confirms that the slip effect is dominant. In a cholesteric LC droplet, the discrepancy between the calculated flow velocity by

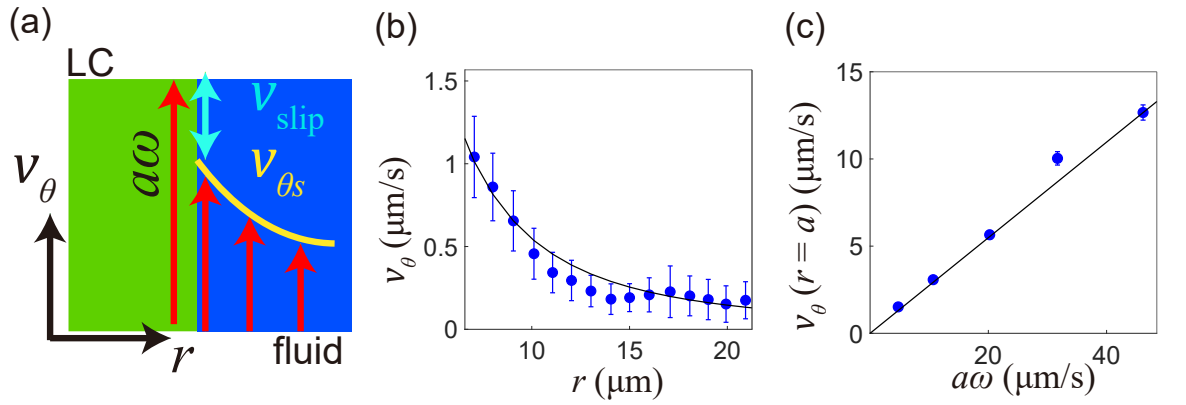

Figure 5.6. Flow field induced by an NLC rotator (radius $a = 3.4$ μm) in a 60 wt% aqueous glycerol solution. (a) A schematic of a velocity profile under the slip boundary condition. The green and blue regions represent the regions of an LC and a fluid, respectively. The red arrow denotes a v_θ vector. Slip velocity is represented by the double-blue arrow. The yellow line corresponds to $v_{\theta s}$ by Eq. (5.14). (b) Variation of the tangential component of the flow field v_θ with the distance r from the center of the droplet with a 28.2 mW laser power. The solid line represents the best-fitted curve of Eq. (5.14) with $\beta = 3.50 \times 10^3$ N·s/m^3. (c) Variation of the flow velocity at the droplet surface $v_\theta(a)$ with $a\omega$ (a: fixed). The laser power used were ranged from 9.4 mW to 47 mW. The solid line is the theoretical value determined using Eq. (5.14) with the same β as in (b).

the droplet rotation and the measured one has been also observed [87]. The slip at the droplet surface has been cited as one of the possible origins of this disagreement. Slip phenomena are widely observed at the interface between the polymer solution and solid surface [88], and the initial shear stress at which slip occurs is usually as large as 10^5 Pa [89]. In the case of the liquid–liquid interface, the initial shear stress decreases dramatically and its magnitude becomes a few Pa. [90]. In our experiment, the shear stress acting on the droplet $\eta \frac{\partial v_{\theta s}}{\partial r}\big|_{r=a}$ is approximately 0.03 Pa where $\eta = 9.8$ mPa·s, $\beta = 3.50 \times 10^3$ N·s/m^3, $a = 3.4$ μm and $\omega = 6.0$ rad/s, which is two orders of magnitude lower than the above value. Although the reason for the slip is not clear at the present stage, it may be related to the alignment of the LC molecules. In an aqueous glycerol solution, the NLC molecules align along the surface because glycerol induces planer anchoring [91]. The surface roughness with planer anchoring is smoother than that with homeotropic anchoring [92]. The slip easily occurs for a smoother surface [93]. We assume that this is also applicable to

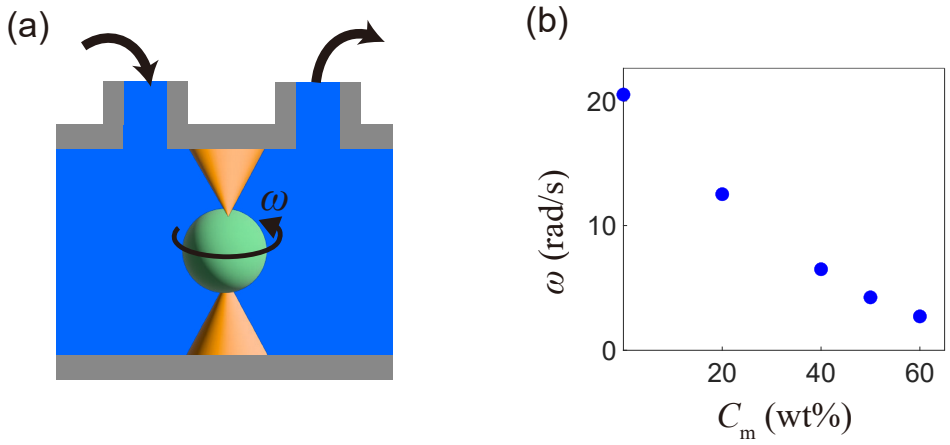

Figure 5.7. Micro-viscometer with an NLC droplet in aqueous glycerol solutions. (a) Schematic of the micro-viscometer. The surrounding solution is exchanged via holes at the top. The black arrow represents the direction of solution flow during solution exchange. (b) Variation of rotation frequency ω with C_{m}. Radius a of the droplet was 5.2 µm and the laser power used was 18.8 mW.

an LC droplet, and the planar anchoring promotes slip at the interface. Furthermore, intermolecular interactions at the interface also affect the slip [94]. Since the adhesive force between glycerol and 5CB (a main component of used LC) in the nematic phase due to hydrogen bonding is weaker than that between water and 5CB, slip at the glycerol–5CB interface is more likely to occur [95]. Adding glycerol can reduce the adhesion force between the droplet surface and the surrounding fluid and promotes slip.

5.5 A droplet micro-viscometer

For the application of the rotating droplet, we used a droplet as a micro-viscometer. In our micro-viscometer, a single rotating droplet was captured with optical tweezers while changing the glycerol mass concentration C_{m} in a laboratory-made flow device as schematically shown in Fig. 5.7(a). Angular frequency ω of the identical droplet at the same laser power was measured for several C_{m}. The measured ω decreased with C_{m} because the viscosity of the solution increased with increasing C_{m} as shown in Fig 5.7(b). In water, the optical torque Γ_{W} was estimated using Eq. (5.11) with known

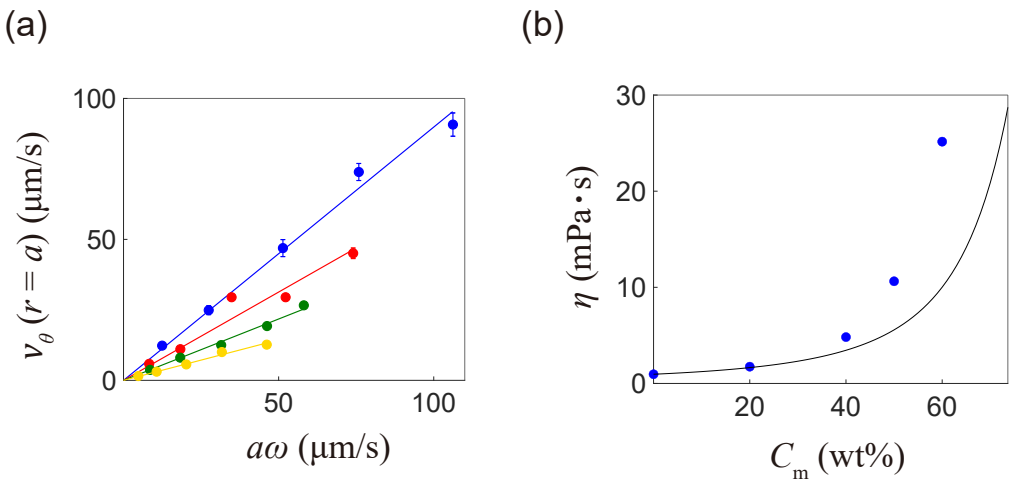

Figure 5.8. Estimation of η in slip boundary condition. (a) Dependence of the flow velocity at the droplet surface $v_\theta(a)$ on $a\omega$ in 20 wt% (filled blue circles, $a = 2.5$ μm), 40 wt% (filled red circles, $a = 2.8$ μm), 50 wt% (filled green circles, $a = 3.8$ μm) and 60 wt% (filled yellow circles, $a = 3.4$ μm) glycerol solutions. The laser power used ranged from 9.4 mW to 47 mW. The solid line represents the linearly fitted line (blue: 20 wt%, red: 40 wt%, green: 50 wt% and yellow: 60 wt%). (b) Variation of viscosity η of the glycerol solutions with the mass concentration C_m measured by our micro-viscometer. The solid line represents literature values [83].

η, $\Gamma_\mathrm{W} = 0.804$ pN· μm. From our previous results, the boundary condition changed to slip boundary condition in the aqueous glycerol solutions. Therefore, the viscous torque in the slip boundary condition is $\frac{\beta a}{\beta a+3\eta}$ times the viscous torque in the no-slip boundary condition, $\Gamma = 8\pi\eta\omega a^3 \frac{\beta a}{\beta a+3\eta}$ [19]. In slip condition, η is expressed as

$$\eta = \frac{\Gamma}{8\pi\omega a^3}\left(\frac{\beta a}{\beta a + 3\eta}\right)^{-1}. \tag{5.15}$$

For estimation of the factor $\frac{\beta a}{\beta a+3\eta}$, the variation of v_θ at the droplet surface with $a\omega$ was measured by changing the power of the incident beam in several C_m as shown in Fig. 5.8(a). Since dependence of v_θ was described by modified Eq. (5.14) $v_{\theta\mathrm{s}}(r = a) = \frac{\beta a}{\beta a+3\eta} a\omega$, the factor $\frac{\beta a}{\beta a+3\eta}$ can be derived from the slope of the best-fitted line to data. This estimation gives the value of the factor $\frac{\beta a}{\beta a+3\eta}$ without knowing β and η. We also considered the increase of Γ due to changes in the refractive index n using Eq. (5.13). At low η, the estimated η agreed with the literature value [83] as shown

in Fig. 5.8(b). An NLC droplet behaves as a solid one because the viscosity of the NLC is much higher than that of solutions. Therefore, fluidization inside the droplet is negligible at low η. On the other hand, at high η, a discrepancy becomes apparent. With the above correction method, the difference between the rotation speed and flow velocity is attributed only to slippage at the surface. η may have been overestimated because the effects of slip and fluidization were not properly separated at this stage. We evaluated the application of the LC droplet to viscosity measurement because the fabrication is easy compared to the solid particle. The results show that the solid particle is more suitable for viscometry because fluidization is negligible.

5.6 Measurement of hydrodynamic interaction between two rotating LC droplets

As another application of LC droplets, we studied the hydrodynamic interactions between two rotating droplets in the same direction. We measured the dependence of rotation frequency ω on the interparticle distance l by controlling trap patterns with an SLM under crossed-Nicols polarizers, as schematically shown in Fig. 5.9(a). Since the dependence of ω for left and right droplets on l is similar, ω for only the left droplet is presented in Figs. 5.9(b) and (c). Water and a 70 wt% aqueous glycerol solution were prepared as the surrounding media. In water, when the droplets were close together ($l < 7$ µm), ω decreased as the droplets approached each other as shown in Fig. 5.9(b). Since the optical torque changes slightly depending on the trapping position, ω gradually changed with l even if the droplets were largely separated ($l >$ 14 µm). Hydrodynamic interaction with the Ronte-Prager approximation gives the rotation frequency $\omega_{i\mathrm{th}}$ of the i-th droplet as

$$\omega_{i\mathrm{th}} = \frac{\Gamma_i}{8\pi\eta a_i^3} - \frac{\Gamma_j}{16\pi\eta l^3}, \tag{5.16}$$

where i and j denote the indices of particles ($i \neq j$). For estimation of Γ, ω for each droplet was measured in the single-particle system, and Γ was estimated by Eq. (5.11). The measured values are in good agreement with the calculated values by Eq. (5.16) as indicated by the solid line in Fig. 5.9(b). The surrounding medium was replaced with a glycerol solution and measured the dependence of ω on l in the same manner as described above. We compared the measured values with the calculated

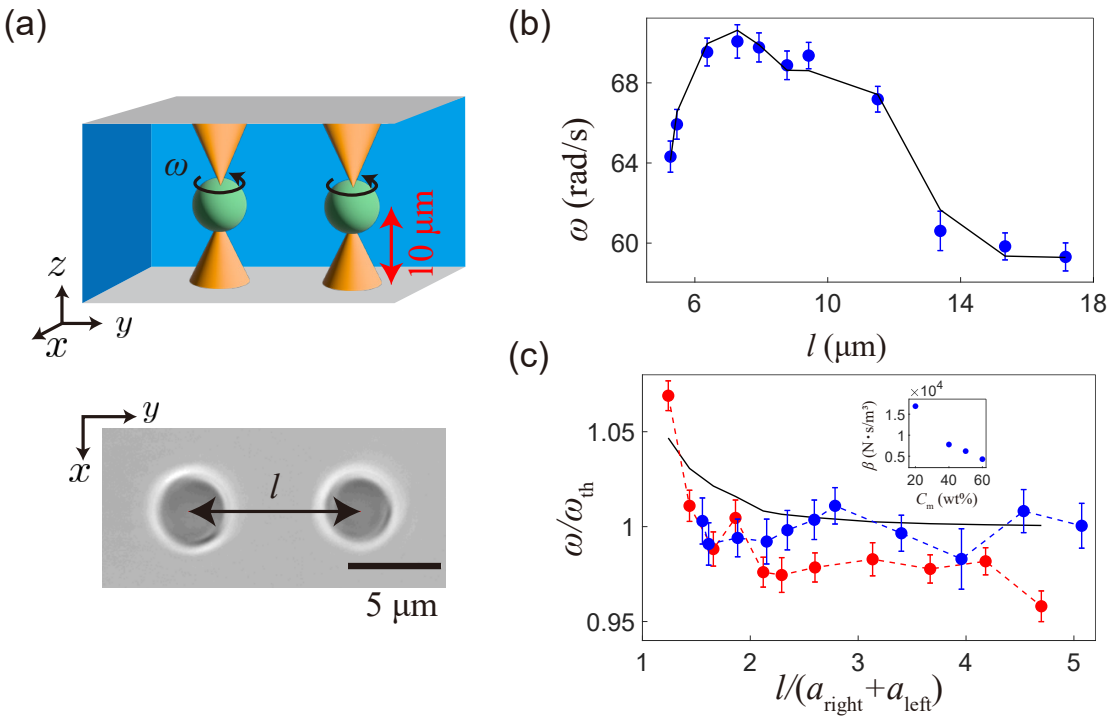

Figure 5.9. Two Rotating particles placed at distance l. (a) Schematic of two rotating particles in a sample cell (top) and its microscope image in the x-y plane (bottom). scale bar is 5 μm. (b) Variation of rotation frequency ω of the left droplet with l in water with 5.6 mW laser power. The solid line represents the calculated values using Eq. (5.16) under the no-slip boundary condition. (c) Ratio of the measured values ω of the left droplet to the theoretical ones $\omega_{\rm th}$ estimated by Eq. (5.16) under no-slip boundary condition in water (blue dots) and a 70 wt% aqueous glycerol solution (red dots). The solid line represents the calculated values using Eq. (5.16) under slip boundary condition. The horizontal axis is normalized by contact distance $a_{\rm right} + a_{\rm left}$, where $a_{\rm right}$ is the radius of the right droplet and $a_{\rm left}$ is that of the left one. The inset represents the variation in the slip coefficient β with $C_{\rm m}$.

values for the water and glycerol solutions as shown in Fig. 5.9(c). Ratios ω/ω_{ith} were almost close to unity in water, which is consistent with the results shown in Fig. 5.9(b). Ratios ω/ω_{ith} were also almost close to one but slightly less than one in the glycerol solution, except for the nearest-neighbor distance ($\frac{l}{a_{\rm right}+a_{\rm left}} = 1.2$). It took a longer time for the measurement in the glycerol solution because ω was slow in the glycerol solution, resulting in a large time difference between the measurement of the two-particle system and the single-particle system for the estimation of Γ. Since

the measurement of the two-particle system was followed by that of the single-particle system, the viscosity of the solution in the single-particle system may slightly decrease due to the heating by light absorption. The estimated Γ in the single-particle system may be overestimated compared to Γ in the two-particle system because we assume the viscosity is constant. When l is small, the second term on the right side of Eq. (5.16) becomes large, and Γ_j becomes significant for ω. In the case of the slip being significant, slip reduces viscous torque Γ_j. The viscous torque in the slip boundary condition $\Gamma_{\rm slip}$ is $\frac{\beta a}{\beta a+3\eta}$ times the viscous toerque in the no-slip boundary condition, $\Gamma_{\rm slip} = 8\pi\eta\omega a^3 \frac{\beta a}{\beta a+3\eta}$ [19]. The value of β at $C_{\rm m} = 70$ wt% was estimated by linear extrapolation with three data points in the inset of Fig. 5.9(c), $\beta = 2.1 \times 10^3 {\rm N{\cdot}s/m^3}$. We calculated ω derived from Eq. (5.16) with $\Gamma_{\rm slip}$, as shown in the solid line of Fig. 5.9(c). The calculated ω is also slightly larger than unity when l is small, and this supports the reduction of hydrodynamic interaction due to the slip.

5.7 Microscale flow field induced by multi-rotators

As a further application of LC droplets, we constructed a microscale device to control the local flow field using rotating NLC droplets. In this system, the spatial arrangement of NLC droplets can be controlled by the HOT. The rotation speed and direction of droplet rotation can be controlled by the laser power and the circular polarization direction, respectively. Two droplets of approximately the same size were trapped using optical tweezers, and the flow field around them was measured. Since the direction of the rotation was the same, a circulating flow appeared around the two particles, and a shear field was induced in the gap between the droplets, as shown in Fig. 5.10(a) and (b). The control of trap patterns by HOT enables the manipulation of multiple particles.

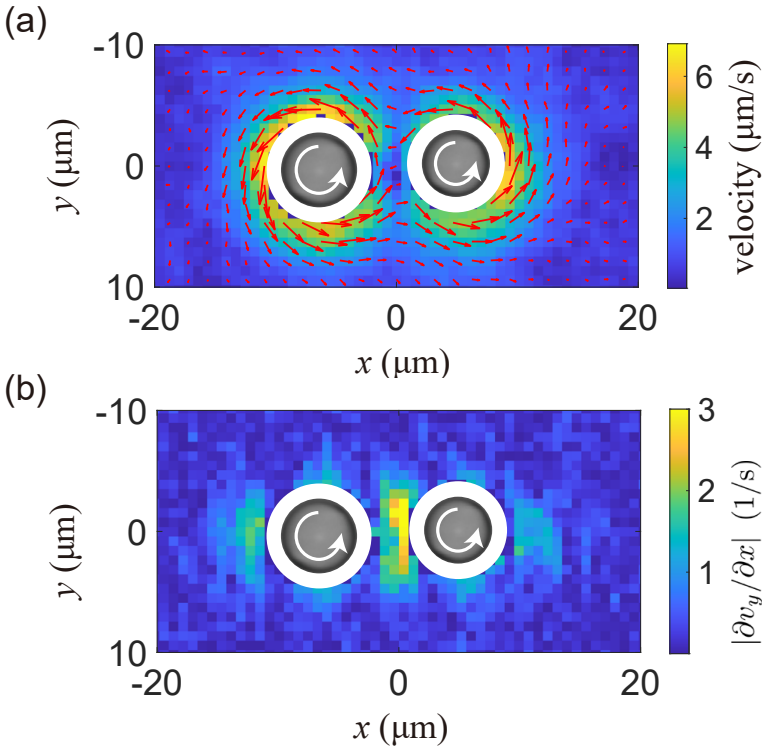

Figure 5.10. Two Rotating NLC droplets. (a) Induced velocity field v for two rotating NLC droplets with 36 mW laser power. The arrows represent local velocity vectors. (b) Shear rate of flow velocity in y-direction $\frac{\partial v_y}{\partial x}$ evaluated from (a).

5.8 Conclusion

The rotational motion of an NLC droplet was studied in water and aqueous glycerol solutions. In water, the flow field induced by the droplet rotation was in good agreement with the theoretical field where solid particle and no-slip boundary conditions are assumed. However, the induced flow velocity in the glycerol solution was lower than the theoretical value. This suggests that the above assumptions (the solid particle and no-slip boundary conditions) may have been violated. We tested whether the fluidization effect or slip at the droplet surface was dominant. The results indicated that the slip at the droplet surface was the dominant contributor to the reduction of the induced flow field. K. Nishiyama *et al.* report the disagreement between the calculated flow velocity by rotation of a ChLC droplet and the measured one [87]. Although they mention the possible reasons for the disagreement, the reasons remain unclear. Although the type of LC is different from our droplet, our results indicate the importance of investigating the boundary condition. Indeed, LC materials have been explored as lubricants because some LC materials exhibit low friction due to their long-range orientational order [96]. Furthermore, this study shows that the boundary condition can be controlled by changing the surrounding solution. Since the control of the boundary condition enables the reduction of viscous resistance of objects, our findings lead to the efficient transportation of objects in viscous fluids.

We constructed multi-droplet systems with HOT and demonstrated the control of microscale flow. In contrast to many microfluidics devices [97, 98], the combination of the droplets and HOT can induce various flow patterns without changing microfluidics devices. This advantage enables the control of flow fields on demand, resulting in saving the design time of microfluidics devices.

Chapter 6

Electrically driven Janus particles in complex fluids

6.1 Introduction

Microorganisms and bacteria, known as microswimmers, are often exposed to viscoelastic fluids in nature [75, 99]. For example, spermatozoa swim in cervical mucus and bacteria are surrounded by polymer solutions [100]. Non-swimming objects such as blood cells also exist in viscoelastic fluids [101]. Thus understanding of motion in viscoelastic fluids is important not only for biological phenomena but also for microfluidics.

These viscoelastic fluids differ from Newtonian fluids in that they behave as either a liquid or a solid depending on the deformation rate applied [2]. Indeed, the motility of the bacterium *E.coil* is different in Newtonian and viscoelastic fluids [102]. To study the effect of viscoelasticity on the motion of microswimmers, it is important to control the swimming velocity because the fluid behavior depends on the deformation rate. Artificial microswimmers are useful tools for studying the effect of viscoelasticity because their swimming velocity can be controlled by external fields.

A Janus particle is a typical artificial microswimmer, which is a colloidal particle with two distinct surfaces or regions that exhibit different properties [10]. Janus particles can be driven by external stimuli, and the driving method depends on the combination of the surface materials [103]. An optically driven Janus particle in viscoelastic fluids exhibits a circular orbit [104]. On the other hand, a Janus particle driven by a chemical method exhibits the ballistic motion, which is the same as in Newtonian fluids [5]. Although the mechanical response of the viscoelastic fluids depends on the deformation rate, the range of the velocity in the two experiments is limited. The optically driven particle is not fast (typically a few µm/s in water-lutidine mixture) [105]. In the chemical method, the control of velocity is difficult because the velocity depends on the concentration of H_2O_2 in the surrounding solution, and the concentration changes with the particle driving. An AC electric field can drive a metal-dielectric Janus particle by induced-charge electrophoresis (ICEP) [20, 45].

Since velocity of ICEP is determined by an electric field, the control of the velocity is easy compared to the above two methods [103].

In this study, we investigated the effect of viscoelastic fluids on the motion of Janus particles driven by ICEP. Both translational and rotational motion of a Janus particle were observed with varying its translational velocity in polymer solutions. The experimental results are discussed considering the elastic force from the polymer network. Since the behavior of the viscoelastic fluids depends on the deformation rate, the relationship between the velocity and the motion of the Janus particle is studied. The difference between the motion of optically and chemically driven Janus particles is also discussed based on the relationship.

6.2 Materials and methods

6.2.1 Materials

Janus particles

A silica particle half-coated with chromium (Cr) was used as a Janus particle. The Janus particles were prepared in the following way.

1. Creation of monolayer
   Silica particles (Hyprecica, UEXC) with a diameter of 5 µm were soaked in butanol (Merck) for a few days. The density of the silica particles was approximately 0.1 g/ml.
   A container containing water, butanol and a glass slide was prepared. The soaked silica with butanol fell through the walls of the container to the surface of the solution, forming a monolayer at the air-water interface (Fig. 6.1 (a)) [106]. After the monolayer covered the entire surface, water was drained from the bottom of the container using a syringe pump at 60 ml/h, as shown in Fig. 6.1 (b).

2. Vapor deposition on a monolayer
   A 25-nm-thick Cr layer was formed on the monolayer by vacuum evaporation as shown in Fig. 6.1 (c). This Cr layer formed a hemispherical cap on the particle [107].

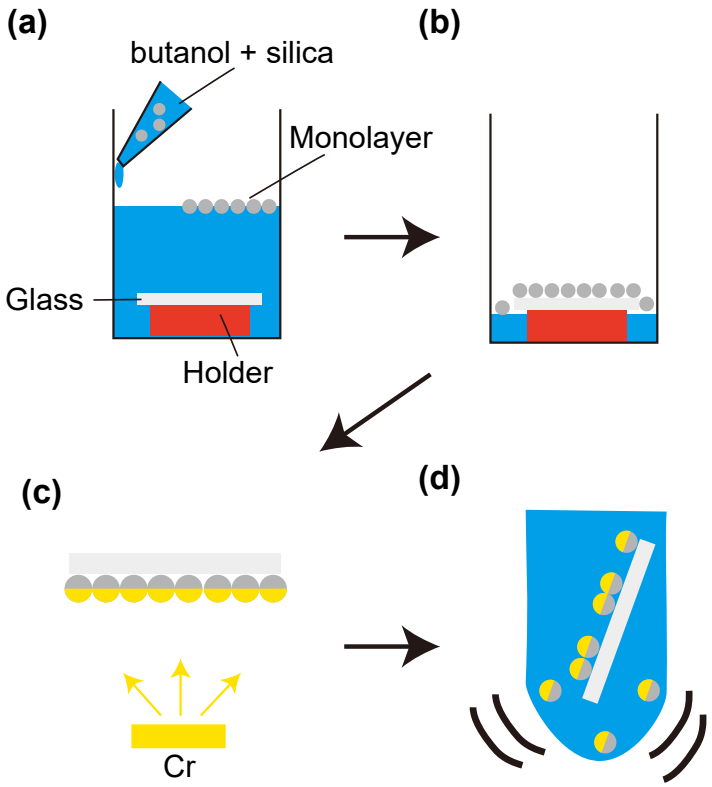

Figure 6.1. Schematic of Janus particle fabrication. (a) Formation of monolayer at an air-water interface. (b) Draining water from a container. (c) Vapor deposition of Cr on the monolayer. (d) The removal of Janus particles from a glass slide by sonication.

3. Collection of Janus particles from solutions

   The glass slide with the Janus particles was immersed in water, and the particles were removed by sonication as shown in Fig. 6.1 (d). After the removal of the Janus particles from the glass slide, the Janus particles were washed in water (three times) and ethanol (three times) with sonication.

Polyethylene oxide (PEO) solutions

Aqueous solutions of polyethylene oxide (PEO) (Sigma-Aldrich, $[\text{-}CH_2CH_2O\text{-}]_n$, molecular weight: 10^6) with mass concentration of PEO, c_m, were prepared. The overlap concentration of PEO c^* is 0.125 wt%. The PEO solutions were gently mixed

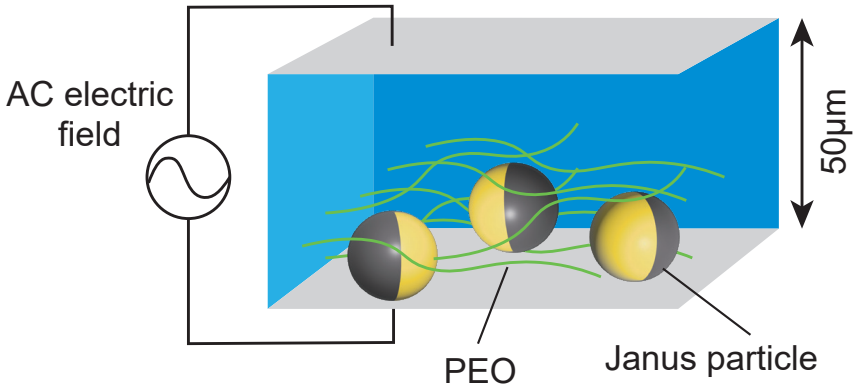

Figure 6.2. Schematic of the experimental system. The green line represents a polymer.

for a few days. After mixing, the prepared PEO and the Janus particles were gently mixed for a few hours. The temperature was set at 25^{o}C (298 K).

Sample cell

A Janus suspension was sandwiched between two transparent electrodes (ITO glass, GEOMATEC) coated with a 25-nm-thick SiO_2 layer to prevent the Janus particles from sticking to the cell bottom. The two electrodes were separated by double-sided tape whose thickness was 50 μm.

6.2.2 Methods

Experimental system

An AC electric field with maximum amplitude of 20 V_{pp} and frequency of 3 kHz was applied to the sample cell. Since Janus particles were heavier than the solution, they sedimented to the bottom and their motion was restricted to a two-dimensional plane perpendicular to the electric field as shown in Fig. 6.2.

The motion of the Janus particles was observed through the bottom electrode by an inverted optical microscope (Eclipse Ti, Nikon) with a ×10 (above 10 Vpp) or ×20 (below 10 Vpp) objective lens (Plan Fluor, Nikon). Images of the Janus particles were captured by a complementary metal-oxide-semiconductor (CMOS) camera (Orca-Flash 4.0, Hamamatsu, 2048 × 2048 pix^2). The exposure time of the CMOS

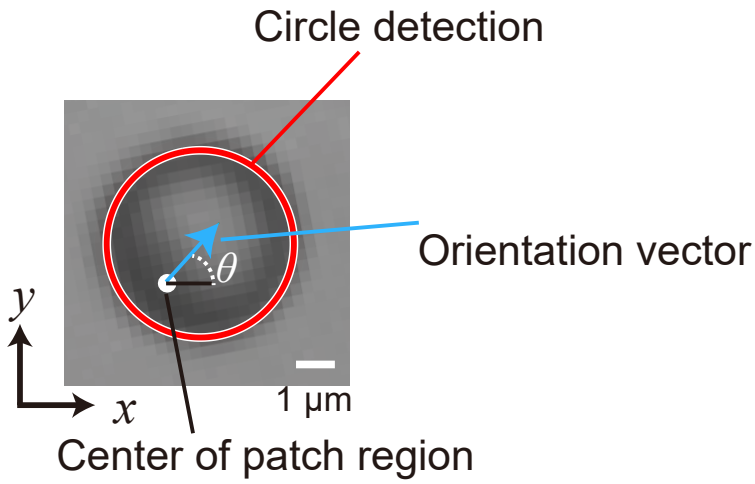

Figure 6.3. Detection of the center of a Janus particle and its patch region. The red circle represents the outline of the Janus particle. The white dot denotes the center of the patch region. The blue arrow represents the orientation vector of the particle. θ is the angle between the orientation vector and the x-axis.

camera varied according to the applied electric field: 50 msec for high voltage (above 10 Vpp) and 0.2 s for low voltage (below 10 Vpp).

Position and orientation detection of a single Janus particle

The two-dimensional position of the Janus particles was detected by circle detection using MATLAB as shown in Fig. 6.3. A center of the patch region (Cr cup) was also detected by binarizing the image of the Janus particle. The orientation vector of the particle was calculated by subtracting the center position of the particle from the center of the patch region as shown in the blue arrow in Fig. 6.3. θ is the angle between the orientation vector and the x-axis.

6.3 Trajectories of Janus particles

The trajectories of the Janus particles in water were almost straight at high propulsion velocity v as shown in Fig. 6.4(a). Figure 6.4(b) shows mean-squared displacement $\langle \Delta r^2 \rangle$ (MSD) of the two-dimensional trajectories of Fig. 6.4(a). In water, the slope was close to two, indicating that the Janus motion was ballistic, $\langle \Delta r^2 \rangle = (v\Delta t)^2$.

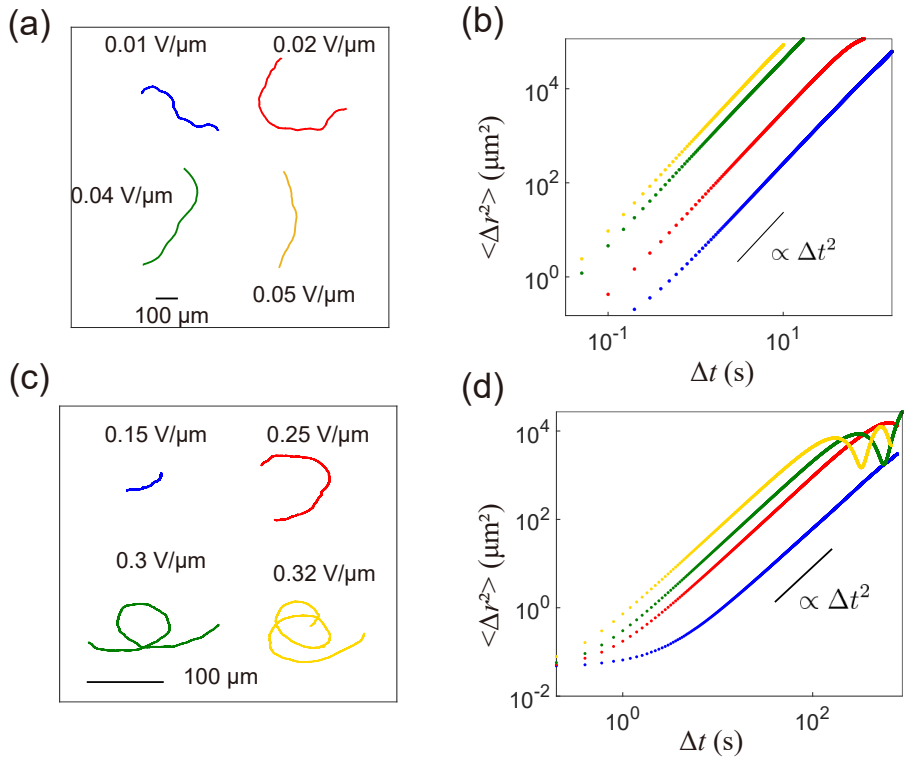

Figure 6.4. Motion of Janus particles in water (a,b) and 1 wt% PEO solution (c,d). (a) Two-dimensional trajectories in water at different electric fields (0.01-0.05 V/μm). The scale bar is 100 μm. (b) Mean-squared displacement (MSD) evaluated from the two-dimensional trajectories of (a). The colors respectively correspond the velocities in (a). MSD is proportional to Δt^2. (c) Two-dimensional trajectories in 1 wt% PEO solution at different electric fields (0.15-0.32 V/μm). The scale bar is 100 μm. (d) MSD in PEO solution. The colors respectively correspond the velocities in (a). MSD is proportional to Δt^2 at the middle time range.

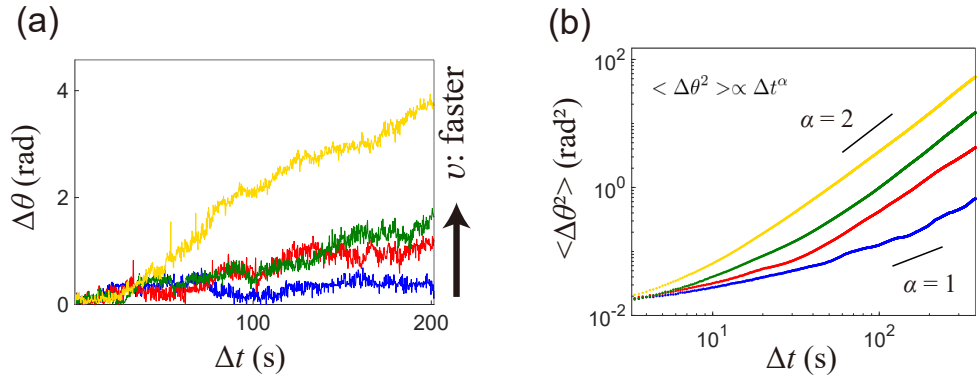

Figure 6.5. Rotation of a Janus particle in the 1wt% PEO solution. (a) Variation in θ with elapsed time Δt at different v(blue: 0.1 µm/s, red: 0.3 µm/s, green: 0.5 µm/s and yellow: 0.8 µm/s). (b) Mean-squared angular displacement $\langle \Delta\theta^2 \rangle$ of (a). The relationship between color and v is the same as in (a). The lower and upper solid lines are proportional to Δt and Δt^2, respectively.

Consequently, v was estimated from MSD. On the other hand, the trajectories of Janus particles in a 1 wt% PEO solution changed from a straight line to a circular orbit with the increase of E as shown in Fig. 6.4(c). MSD of the Janus particle in the PEO solution was proportional to Δt^2 in small v, whereas MSD exhibited oscillatory dependence on Δt in large v as shown in Fig. 6.4(d). The particle started to rotate when v exceeded a certain velocity in the PEO solution.

6.4 Rotation of a Janus particle in a PEO solution

Time evolution of the angler displacement $\Delta\theta$ of the Janus particle in the PEO solution was measured in several v as shown in Fig. 6.5(a). v was esitmated by the slope of $\langle \Delta r^2 \rangle$ in the region of $\langle \Delta r^2 \rangle \propto \Delta t^2$, $\langle \Delta r^2 \rangle = (v\Delta t)^2$. Although this estimation of v is affected by the curvature of a circular orbit, we consider that the error in the estimation is relatively small because the orbit radius is relatively large to the size of the Janus particle. $\Delta\theta$ increased with increasing v, indicating coupling between translational and rotational motion. Figure 6.5(b) shows mean-squared angular displacement $\langle \Delta\theta^2 \rangle$ (MSAD) at different v. In small v, the slope of $\langle \Delta\theta^2 \rangle$ was one, $\langle \Delta\theta^2 \rangle \propto \Delta t$, meaning that the rotation is diffusive. On the other

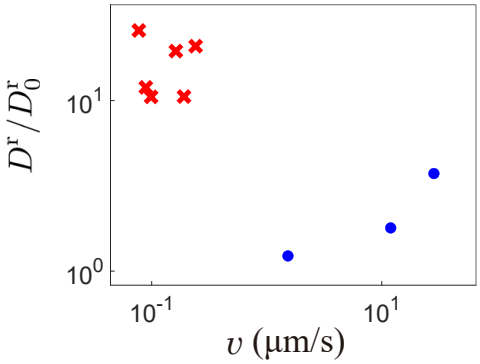

Figure 6.6. Ratio D^r/D_0^r in water and 1wt% PEO solution. The blue dots and red crosses are the ratios D^r/D_0^r in water and the PEO solution, respectively. D_0^r is calculated from Eq. (6.1) with $a = 2.5$ μm, $T = 298$ K, $\eta = 8.9 \times 10^{-4}$ Pa·s (water) and $\eta = 0.89$ Pa·s (1wt% PEO solution).

hand, in large v, the slope becomes two, indicating that the particle rotates at a constant angular frequency ω, $\langle \Delta\theta^2 \rangle \propto (\omega \Delta t)^2$.

In the region of $\langle \Delta\theta^2 \rangle \propto \Delta t$, the rotational diffusion coefficient D^r can be evaluated from $\langle \Delta\theta^2 \rangle$ with $\langle \Delta\theta^2 \rangle = 2D^r \Delta t$. The Stokes-Einstein relation also gives the rotational diffusion coefficient D_0^r as

$$D_0^r = \frac{k_B T}{8\pi\eta a^3}, \tag{6.1}$$

where k_B is the Boltzmann constant, T is the absolute temperature, η is the viscosity of a surrounding solution and a is the radius of the particle. Figure 6.6 shows the ratio of the estimated value of D^r from MSAD to the theoretical one of D_0^r, D^r/D_0^r. In water, the ratios D^r/D_0^r are close to unity, as shown in the blue dots of Fig. 6.6. On the other hand, in the PEO solution, D^r becomes approximately several ten times higher than D_0^r as shown in the red diamonds in Fig. 6.6.

In the region of $\langle \Delta\theta^2 \rangle \propto \Delta t^2$, estimated ω by MSAD increased with increasing v as shown in Fig. 6.7. In both regions, the translational motion of the Janus particle in the polymer solution enhanced its rotational motion.

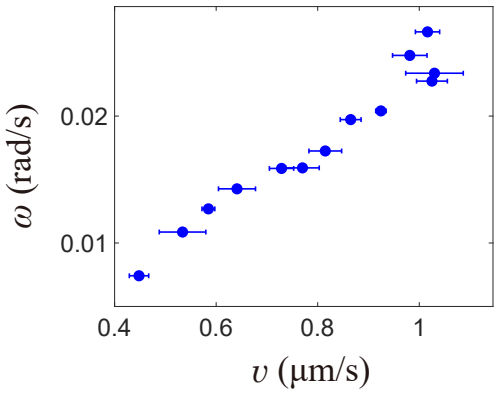

Figure 6.7. Variation in angular frequency ω with v.

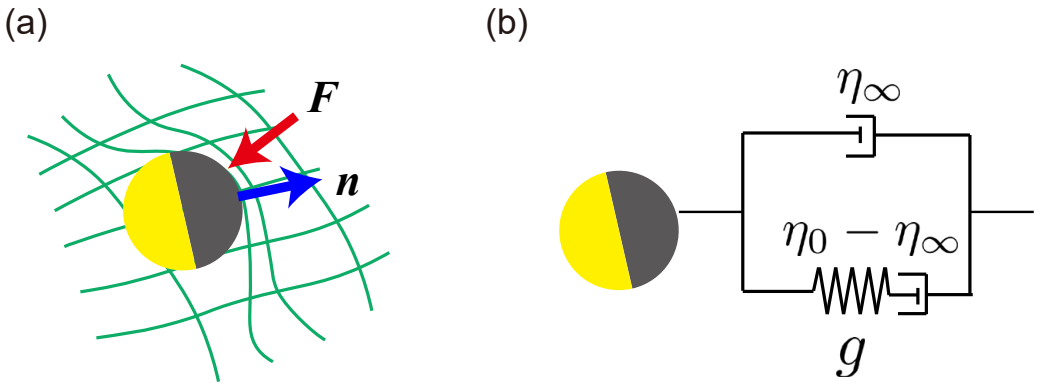

Figure 6.8. A moving Janus particle in a semidilute polymer solution. (a) Schematic of the polymer network deformed by a Janus particle. Blue and red arrows represent the instantaneous propulsion direction $\boldsymbol{n}$ and the friction force $\boldsymbol{F}$, respectively. (b) Model for mechanical representation of the solution. The model is composed of a dashpot (η_0) and a Maxwell combination in series of an elastic element (stiffness g) and a dashpot (viscosity $\eta_0 - \eta_\infty$) with relaxation time $\tau = \frac{\eta_0 - \eta_\infty}{g}$. η_0 and η_∞ are the zero-shear viscosity and the instantaneous viscous dissipation due to the solution, respectively.

6.5 Origin of torque

The enhancement of the rotational motion occured not in water but in a semidilute polymer solution. Although a moving particle experiences only viscous resistance in

Newtonian fluids, the particle in the semidilute polymer solution is subjected to an elastic force from the polymer network [3].

A stress-relaxation modulus $G(t)$ mimics the mechanical response of the viscoelastic fluids [104],

$$G(t) = 2\eta_\infty \delta(t) + [(\eta_0 - \eta_\infty)/\tau]\, e^{-(t/\tau)}. \tag{6.2}$$

The first term represents the instantaneous relaxation of the solution viscosity with η_∞. The second term expresses the time-delayed elastic response of the polymer solution with relaxation time τ and zero-shear viscosity η_0. The friction force $\boldsymbol{F}$ acting on a particle moving at propulsion velocity $\boldsymbol{v}$ is expressed as

$$\boldsymbol{F}(t) = v \int_{-\infty}^{t} \Gamma_{\mathrm{T}}(t - t')\boldsymbol{n}(t')dt', \tag{6.3}$$

where $\Gamma_{\mathrm{T}}(t) = 6\pi a G(t)$ is the memory friction kernel and we assume that the magnitude of $\boldsymbol{v}$ is constant, $\boldsymbol{v}(t) = v\boldsymbol{n}(t)$ [104]. The direction of $\boldsymbol{F}$ depends on all previous times. Since $\boldsymbol{n}(t)$ varies due to thermal fluctuation, the instantaneous propulsion direction $\boldsymbol{n}(t)$ is not always parallel to the direction of $\boldsymbol{F}(t)$, as shown in Fig. 6.8(a) (corresponding mechanical representation is Fig. 6.8(b)). This difference induces the torque. The torque $\boldsymbol{T}$ applied to the Janus particle is expressed by the cross product of lever arm $\boldsymbol{L}$ and $\boldsymbol{F}$ as

$$\boldsymbol{T} = \boldsymbol{L} \times \boldsymbol{F} = -\mu a v \int_{-\infty}^{t} \Gamma_{\mathrm{T}}(t - t')\boldsymbol{n}(t) \times \boldsymbol{n}(t')dt', \tag{6.4}$$

where the effective lever arm $\boldsymbol{L} = -\mu a \boldsymbol{n}$ is introduced, which mimics the spatial delay of $\boldsymbol{F}(t)$ relative to the center of the Janus particle (μ is a fitting paramter).

Since the boundary between Cr and silica was always in a plane parallel to the direction of $\boldsymbol{E}$, only rotation in the z-axis was considered. The Langevin equation for rotation in low-Reynolds region is expressed as

$$-\int_{\infty}^{t} \Gamma_{\mathrm{R}}(t - t')\dot{\theta}(t')dt' + T_z(t) + \zeta_{\mathrm{R}}(t) = 0, \tag{6.5}$$

where $\Gamma_{\mathrm{R}} = 8\pi a^3 G(t)$ is the memory kernel for angular friction, T_z is the z component of $\boldsymbol{T}$ and ζ_{R} is the orientational thermal fluctuations. On average for time, $\langle \zeta_{\mathrm{R}} \rangle_t = 0$, and Eq. (6.5) reduces to

$$\int_{\infty}^{t} \Gamma_{\mathrm{R}}(t - t')\dot{\theta}(t')dt' = T_z(t). \tag{6.6}$$

The balance between the viscous torque $\int_{\infty}^{t} \Gamma_{\mathrm{R}}(t-t')\dot{\theta}(t')dt'$ and the torque caused by time-delayed elastic force $T_z(t)$ determines ω. When we assume constant rotation ($\dot{\theta} = \omega$), the equation for ω is obtained from Eq. (6.6) as

$$\omega = \frac{3\eta v}{4a\tau}\left(1 - \frac{\eta_\infty}{\eta_0}\right)\frac{\omega}{\omega^2 + \frac{1}{\tau^2}}. \tag{6.7}$$

Three roots of Eq. (6.7) are given by

$$\omega = \begin{cases} 0, & (v < v_{\mathrm{c}}) \\ \pm\frac{1}{\tau}\sqrt{\frac{3\eta v\tau}{4a}\left(1 - \frac{\eta_\infty}{\eta_0}\right) - 1} & (v \geq v_{\mathrm{c}}). \end{cases} \tag{6.8}$$

The solutions of $\omega = 0$ corresponds to the straight motion, and this is consistent with the experimental observation at small v. On the other hand, two non-zero solutions become real values only if $\frac{3\eta v\tau}{4a}\left(1 - \frac{\eta_\infty}{\eta_0}\right) - 1 > 0$. This means that constant rotation occurs above critical velocity v_c, given by

$$v_c = \frac{4a}{3\eta\tau\left(1 - \frac{\eta_\infty}{\eta_0}\right)}. \tag{6.9}$$

Similar behavior was observed in our experiments: the constant rotation only occurred above certain v. Using v_c, ω for non-zero values (lower part of Eq. (6.8)) is rewritten as

$$\omega = \pm\frac{1}{\tau}\sqrt{\frac{v}{v_c} - 1}. \tag{6.10}$$

Since mechanical properties of the PEO solution characterized by η_0, η_∞ and τ determine ω, the parameters were estimated by MSD of a probe particle (Detailed method is presented in Appendix E). Self-propulsion velocity $\boldsymbol{v}_{\mathrm{self}}$ of a Janus particle is defined as the component of its instantaneous velocity vector $\boldsymbol{v}(t)$ parallel to the orientation vector $\boldsymbol{n}(t)$, $v_{\mathrm{self}}(t) = \boldsymbol{v}(t) \cdot \boldsymbol{n}(t)$. The variation of ω with v_{self} is well fitted by Eq. (6.10) where the fitting parameter is μ, as shown in the solid line in Fig. 6.9(a). The agreement supports that the origin of the torque is the time-delayed elastic force from the solution.

A deformable active particle shows similar behavior that the particle with velocity above a threshold rotates, which is described by Ohta-Ohkuma model [108]. In the Ohta-Ohkuma model, misalignment between the propulsion force and the major axis

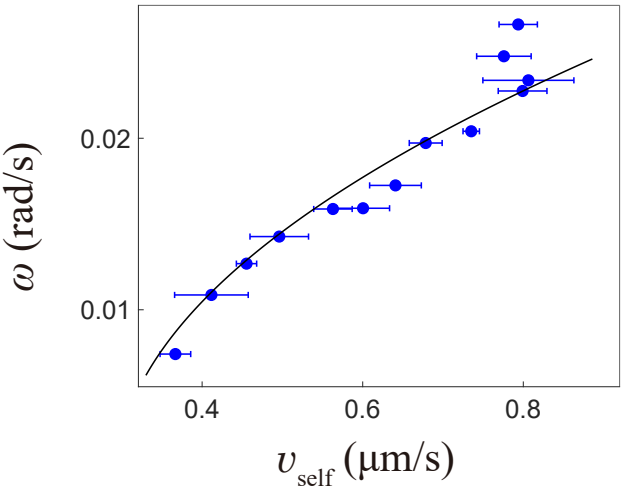

Figure 6.9. Variation in ω with v_{self} in the 1wt% PEO solution. The solid line represents the best-fitted curve of Eq. (6.10) where $\eta_0 = 0.18$ Pa·s, $\eta_\infty = 0.045$ Pa·s, $\tau = 57.8$ s and the fitting parameter is $\mu = 0.26$.

ellipse of the particle induces rotation. The misalignment is also an important factor for rotation of a deformable particle. Indeed, NLC droplet with above certain velocity exhibits a circular orbit [15]. For slow droplets, since viscous stress acting on the droplet surface is relatively small to the elastic force of the droplet, the droplet does not deform. While, as the velocity increases, the viscous stress becomes large and the droplet deforms, resulting in rotational motion.

6.6 Critical velocity

The dependence of v on E^2 was measured in water and a 1 wt% PEO solution, as shown in Figs. 6.10(a) and (b), respectively. In water, v is proportional to E^2 (Fig. 6.10(a)), which is consistent with previous studies [20]. On the other hand, in the PEO solution, the dependence of v on E^2 was different from that in water. For small v, $v \propto E^2$ and this is the same as in water as shown in the solid line of Fig. 6.10(b). The same dependence as for water indicated that the polymer solution behaved as a Newtonian fluid. Indeed, for a Janus particle with a small v, straight-line trajectories were observed. On the other hand, v gradually deviates from the line proportional

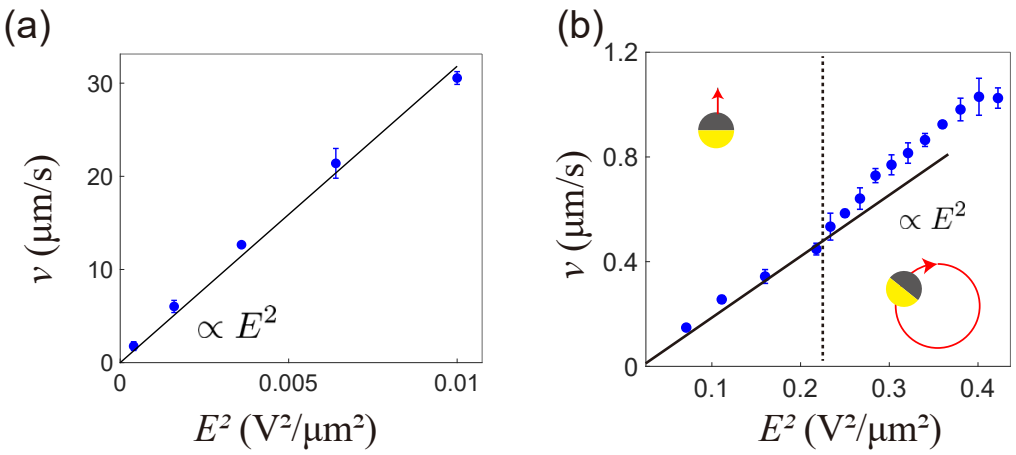

Figure 6.10. Dependence of v on E^2 in water (a) and a 1wt% PEO solution (b). The solid line is proportional to E^2. The dashed line represents the critical velocity obtaibed by Fig 6.9(a). Straight and circular motion were observed on the left and right sides of the dashed line, respectively.

to E^2 as v increases. This deviation means that the solution no longer behaves as a Newtonian fluid, indicating that elastic force appears. Indeed, many Janus particles with a large v exhibit circular orbits.

Two time scales are important for the mechanical response of viscoelastic fluids: traveling time $t_{2a} = 2a/v$ and relaxation time of a polymer network τ, as shown in Fig. 6.11(a). If $t_{2a} < \tau$, the Janus particle experiences the elastic force from the network because a polymer network remains for the traveling time, as shown in Fig. 6.11(b). On the other hand, if $t_{2a} > \tau$, the Janus particle is no longer subjected to the elastic force because elastic stress originated by the network is released for t_{2a}. As a result, only the viscous resistance acts on the particle, as shown in Fig. 6.11(c). Ratio of τ to t_{2a} defines as the Weissenberg number Wi,

$$Wi = \frac{\tau}{2a/v}. \tag{6.11}$$

In the conventional context, Wi is defined as $Wi \equiv \dot{\gamma}\tau$, where $\dot{\gamma}$ is the shear rate and τ is the relaxation time. In the present case, we regard $\dot{\gamma} = \frac{v}{2a}$. When $Wi \ll 1$, a Janus particle mainly experiences the viscous resistance. While, $Wi \gg 1$, the particle receives the elastic force from the solution. Wi can be controlled by changing c_{m}

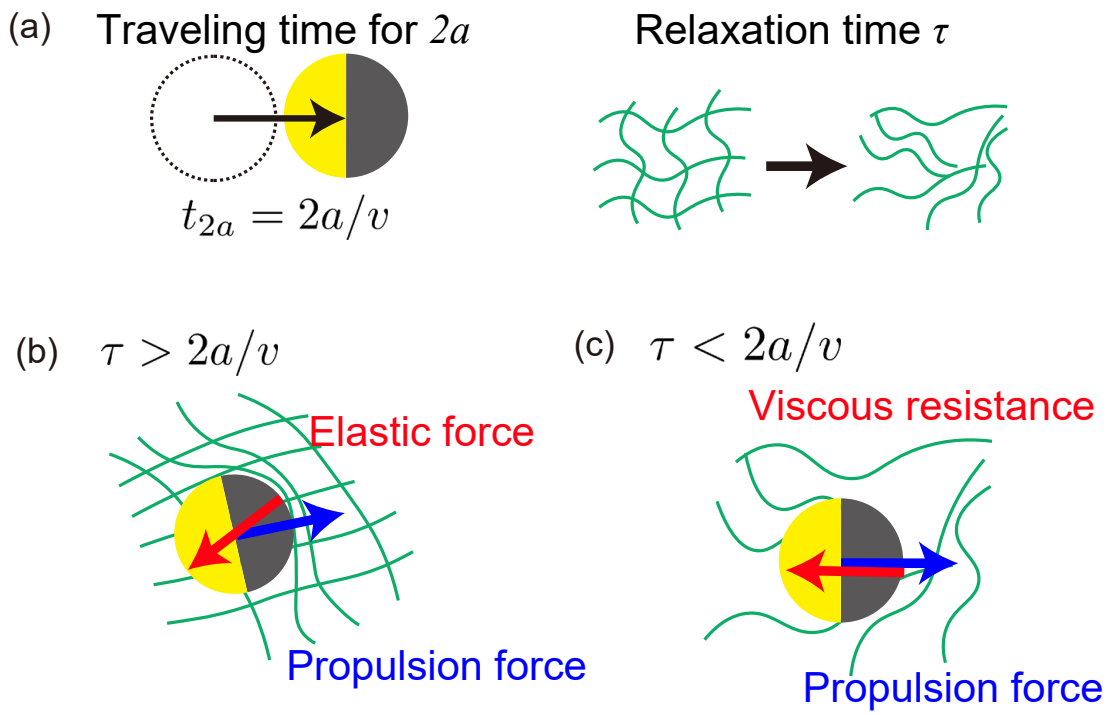

Figure 6.11. Traveling time of a Janus particle t_{2a} and relaxation time of a polymer solution τ. (a) Schematic of traveling time t_{2a} and relaxation time τ. The green lines represent polymers. (b, c) Schematic of the force acting on the Janus particle for $\tau > t_{2a}$ (b) and $\tau < t_{2a}$ (c). The blue arrow represents propulsion force. The red arrows in (b) and (c) represent elastic force and viscous resistance, respectively.

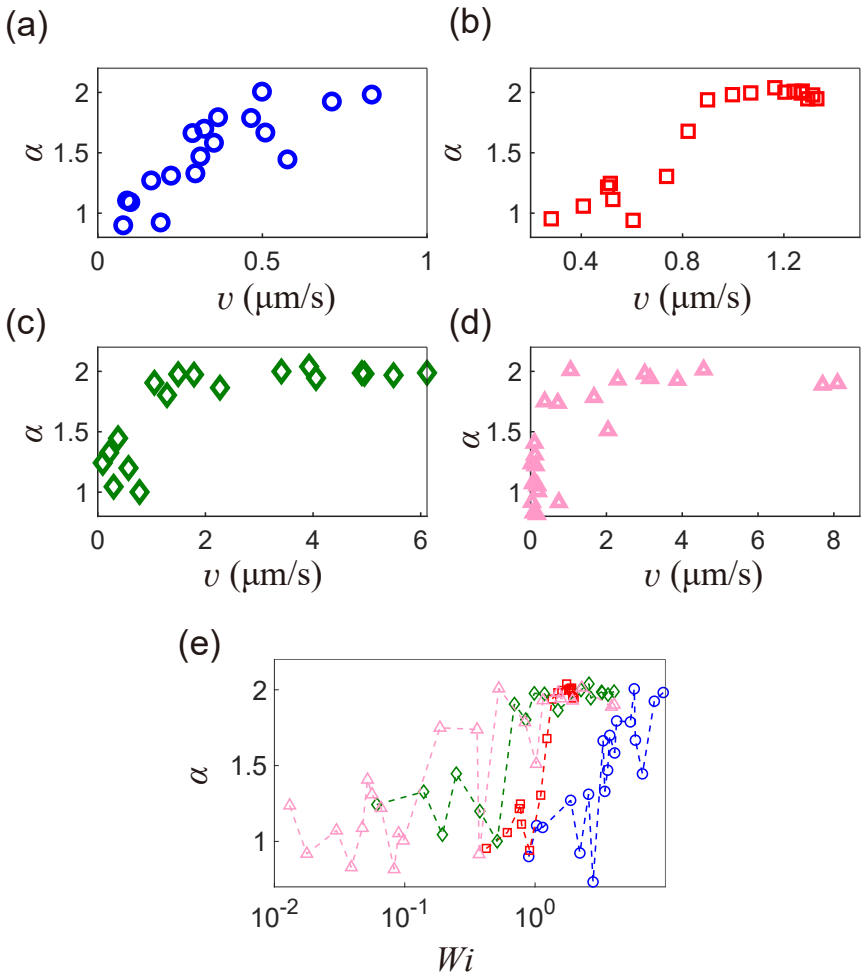

Figure 6.12. Rotational motion of Janus particles in several c_m. (a-d) Variation of α with v in (a) $c_m = 1$ wt%, (b) 0.75 wt%, (c) 0.5 wt% and (d) 0.25 wt%. α is the power index of Δt for $\langle \Delta\theta^2 \rangle \propto \Delta t^{\alpha}$. (e) Variation in α with Wi in several c_m (blue: 1 wt%, red: 0.75 wt%, green: 0.5 wt% and pink: 0.25 wt%)

because τ depends on c_{m} [109]. Indeed, measured τ estimated from MSD of a prove particle changed according to c_{m}, as presented in Appendix E. The transition between linear and circular motion can be evaluated from the slope in MSAD. The power index α of Δt for $\langle \Delta\theta^2 \rangle \propto \Delta t^{\alpha}$ was evaluated at several c_{m} as shown in Figs. 6.12(a)-(d). The rotational motion is diffusive in $\alpha = 1$, whereas the particle rotates at constant angular frequency in $\alpha = 2$. Figure 6.12(e) shows variation in α with Wi in several c_{m}. Rotation corresponding to $\alpha = 2$ occurs at the order of unity in each c_{m}, and this indicates that the emergence of elastic force causes the transition from linear to circular motion in viscoelastic fluids.

6.7 Conclusion

The rotational motion of Janus particles was studied in the PEO solutions with several c_{m}. The Janus particles were self-propelled via ICEP, and their translational velocity v was controlled by the amplitude of an applied AC electric field. At small v, the rotation of the Janus particle was diffusive, and its rotational diffusion coefficient increased as v increased. This enhancement of the rotational diffusion coefficient is also reported in the case of the optically and chemically driven Janus particle [5, 18, 104]. The Janus particle with v above a critical velocity exhibited a circular orbit, and its angular frequency increased as v increased. This behavior is consistent with the previous study of the optically driven Janus particle [104]. Since the rotation was always diffusive regardless of v in water, the enhancement of the rotation was due to the viscoelastic properties of the solution. The time-delayed elastic force, which expresses the mechanical response of viscoelastic fluids, explained our results. Since the circular motion is reported in the optically driven case [104], this study supports that such a behavior is ubiquitous for active particles in viscoelastic fluids.

Since the behavior of viscoelastic fluids depends on v or c_{m}, we control v and c_{m} over a wider range than those in previous studies [5, 104]. The experimental results reveal that two characteristic times are important for the motion of the particle in the viscoelastic fluids: the traveling time $2a/v$ and the relaxation time of a polymer network τ. The particle experiences viscous resistance if $2a/v > \tau$, whereas the particle is subjected to elastic force if $2a/v < \tau$. The ratio $\frac{\tau}{2a/v}$ defines the Weisenberg number Wi. The rotation of the Janus particle occurs when order of Wi is unity. This

indicates that the emergence of the elastic force induces the transition of the particle motion in viscoelastic fluids. We calculate Wi for the straight motion of a chemically driven Janus particle [5] and the circular motion of an optically driven Janus particle [104]. For the straight motion, the range of Wi is from 10^{-2} to 10^{-1}, and elastic force does not act on the particle. On the other hand, for the circular motion, the minimum value of Wi is approximately 1.8, and the particle receives elastic force. Our explanation based on Wi is consistent with other studies even if driving methods and the type of solutions are different.

Active particles usually exhibit spontaneous dynamic phase separation and giant number fluctuation [110]. In contrast to many active particles, rotating active particle, known as chiral active matter [111], exhibits the suppression of the density fluctuation at long-wavelength [112]. Our results predict that viscoelastic fluids induce the suppression of the density fluctuation of active particles with $Wi > 1$ even if the active particle has no chiral structure. Although detailed analysis has not been performed, the observation result implies the suppression of the density fluctuation (presented in Appendix F). The interaction between an active particle and a surrounding fluid could be important for understanding the collective motion in the viscoelastic fluids.

Chapter 7

Concluding remarks

In this thesis, we have studied the motion of active particles in viscous or viscoelastic fluids using NLC droplets and Janus particles. By controlling rotation (LC droplet) and translation (Janus particle) of the particle, we found characteristic rotational motion.

The energy efficiency of LC droplets is important to rotate the droplet in viscous fluids. Although studies on individual droplets have been conducted [14], it is unclear that which inner structure of LC droplet is more energy efficient. First, the driving mechanism and its energy efficiency are investigated using several types of LC (NLC and ChLC) droplets to find efficient droplets. Quantitative investigation based on the theory of waveplate effect, light-scattering and Bragg reflection reveals that a bipolar droplet has the highest energy transfer efficiency in the prepared droplets. The energy transfer efficiency of a bipolar droplet is approximately 9%. We compare this value (9%) with bipolar droplet reported by S. Juodkazis, *et al.* [56] and cylindrical calcite [9]. The energy efficiency of the droplet by S. Juodkazis, *et al.* is approximately 5%, and this value is roughly similar to our result. On the other hand, The energy efficiency of cylindrical calcite is approximately 22%, and this value is higher than that of the bipolar droplet. This comparison indicates the shape of a birefringent object is relevant to its energy transfer efficiency from light to kinetic energy. The insight obtained by this study gives a hint to design objects with high energy efficiency from light to kinetic energy.

Next, the flow field induced by the rotation of an NLC droplet is studied to understand the effect of the droplet rotation on viscous fluids. Our results reveal that the boundary condition changes depending on the surrounding solutions: the no-slip boundary condition in water and the slip boundary condition for glycerol solution. Although the disagreement between the calculated flow velocity (the no-slip boundary condition) by rotation of a ChLC droplet and the measured one is reported [87], the reason for the disagreement is unclear. Although the type of LC is different from our droplet, our results indicate that investigating the boundary condition for the ChLC droplet could give a clue to solve the disagreement. Our findings on the change of

the boundary condition will lead to the control of the boundary condition of objects, resulting in the efficient transportation of the objects in viscous fluids. Furthermore, we demonstrated the control of microscale flow with multi-droplet systems. As opposed to conventional microfluidics devices [97, 98], the multi-droplet systems can induce various flow patterns without changing microfluidics devices. This advantage is expected to reduce the time for designing the microfluidics devices.

We study the translational motion of Janus particles in polymer solutions to understand the effect of viscoelastic fluids on the motion. The motion of the a Janus particle differs between optically and chemically driven methods [5, 104]. Since the mechanical response of viscoelastic fluids depends on the velocity of the particle, we consider that velocity control over a wide range is important. For the above reason, we used electrically driven Janus particles. The Janus particle exhibits a straight trajectory in small v and a circular orbit in large v. The same behavior is reported in optically driven Janus particles. This agreement indicates that such a rotational behavior is ubiquitous for active particles in viscoelastic fluids. Furthermore, wide-range control of the velocity reveals that Wi is a key factor in determining the motion of the Janus particle in viscoelastic fluids. If $Wi < 1$, the particle experiences viscous resistance, resulting in linear motion. On the other hand, if $Wi > 1$, the elastic force acts on the particle, leading to circular motion. Our explanation based on Wi is consistent with optically and chemically driven Janus particles. Our results indicate that the characteristic time of a complex fluid and the velocity of an object are important for understanding the object motion regardless of driving methods. This insight may provide hints for understanding the movement of microscale objects in heterogeneous medium such as cells. Liquid-liquid phase separation induces heterogeneous distribution of the solution in a cell [113]. Selective aggregation or separation of substances might be induced by the change in the substance motion caused by the viscoelasticity of the surrounding solution.

As mentioned at the beginning of this thesis, localized non-thermal force caused by biomolecules changes viscosity in a cell [6]. This phenomenon indicates that the localized non-thermal force has the potential to control of macroscopic properties of soft matter as shown in Fig. 6.13. This thesis shows the motion of active particles is affected by surrounding solutions. Therefore, optimization not only for active particles but also for complex fluids is relevant to control the properties of complex fluids.

Complex fluids have characteristic time such as the relaxation time of a polymer network or characteristic direction of the structure such as LC. We consider that the characteristics are important to transmit the energy from the active particle to the surrounding fluids. Fusion of active particles and appropriate complex fluids will create novel materials with high-efficiency control.

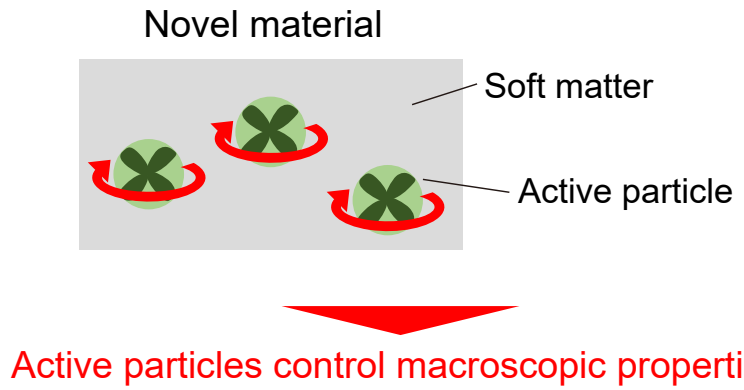

Figure 6.13. Locally driven soft matter composed of active particles.

Appendix

A Spin angular mometum of light

We consider spin angular momentum of light [114]. The density of linear $\boldsymbol{p}$ and angular $\boldsymbol{j}$ momentum for the electromagnetic field are expressed as

$$\boldsymbol{p} = \varepsilon_0 \boldsymbol{E} \times \boldsymbol{B}, \tag{A.1}$$

$$\boldsymbol{j} = \varepsilon_0 \boldsymbol{r} \times (\boldsymbol{E} \times \boldsymbol{B}), \tag{A.2}$$

where $\boldsymbol{E}$ is the electric field, $\boldsymbol{B}$ is the magnetic field and ε_0 is the permittivity in vacuum. Integrating $\boldsymbol{j}$ over all space gives the total angular momentum $\boldsymbol{J}$,

$$\boldsymbol{J} = \int dV \boldsymbol{j}. \tag{A.3}$$

We assume monochromatic fields and $\boldsymbol{E}$ and $\boldsymbol{B}$ are expressed as

$$\boldsymbol{E} = \frac{\boldsymbol{E}e^{-ift} + \boldsymbol{E}^* e^{ift}}{2}, \tag{A.4}$$

$$\boldsymbol{B} = \frac{\boldsymbol{B}e^{-ift} + \boldsymbol{B}^* e^{ift}}{2}, \tag{A.5}$$

where f is the frequency of light and the asterisk denotes complex conjugation. The Maxwell equation gives

$$i\omega \boldsymbol{B} = \nabla \times \boldsymbol{E}. \tag{A.6}$$

$\boldsymbol{J}$ is expressed as

$$\begin{aligned} \boldsymbol{J} &= \frac{\varepsilon_0}{2if} \int dV \boldsymbol{r} \times [\boldsymbol{E} \times (\nabla \times \boldsymbol{E})] \\ &= \frac{\varepsilon_0}{2if} \int dV \sum_{j=x,y,z} E_j^* (\boldsymbol{r} \times \nabla) E_j + \frac{\varepsilon_0}{2if} \int dV \boldsymbol{E}^* \times \boldsymbol{E}, \end{aligned} \tag{A.7}$$

where $\boldsymbol{E} \to 0$ at $\boldsymbol{r} \to 0$. The angular momentum is composed of two contributions. The first and second term on the right-hand side of Eq. (A.7) represent the contribution of the orbital and spin angular momenta, respectively [114].

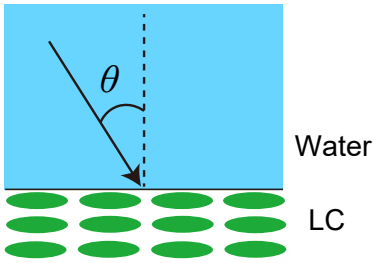

Figure B.1. Light incident from water to the LC phase with the angle of incidence θ. The black arrow represents the traveling direction of light. The green ellipses represent LC molecules. The direction of n_e is parallel to the major axis of the ellipse.

B Estimation of angle between Poynting vector and wave vector α

We estimated the angle between the Poynting vector and wave vector to determine the magnitude of the light-scattering process. In a uniaxial crystal, α is expressed as [115]:

$$\tan\alpha = \frac{1}{2} n_{\mathrm{eff}}(\theta) \left(\frac{1}{n_e^2} + \frac{1}{n_o^2} \sin 2\theta \right), \tag{B.1}$$

$$n_{\mathrm{eff}}(\theta) = \frac{1}{\sqrt{n_o^2 \sin^2\theta + n_e^2 \cos^2\theta}}, \tag{B.2}$$

where n_o is the ordinary refractive index, n_e is the extraordinary refractive index, and θ is the angle of incidence as schematically shown in Fig. B.1. In our case, θ ranged between 0 and 1.17 (rad) because we used focusing light with a numerical aperture of 1.4, and the refractive index of immersion oil is 1.518. Each α value for different incident angles ($0 < \theta < 1.17$) was calculated, and the average value of α was used to estimate the magnitude of the light-scattering process.

C Optical torque transmitted via reflection and transmission in a ChLC droplet

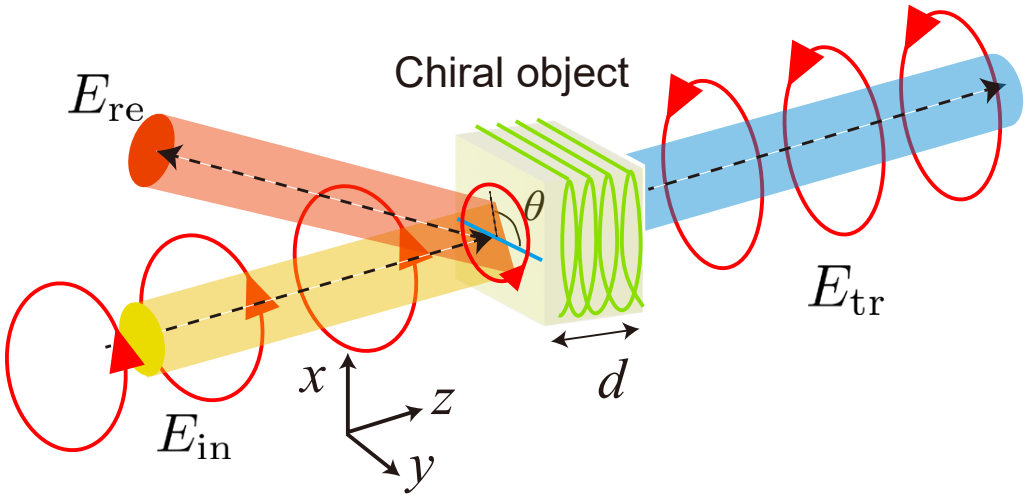

Figure C.1. Schematic of reflection and transmission through a birefringent object with chirality (thickness d). The red arrow represents the polarization of light. The blue line on the birefringent object represents the optical axis of the birefringent object. θ is the angle between the major axis of the polarization ellipse and the optical axis.

In a ChLC droplet, optical torque is transmitted via reflection and transmission [27]. An elliptically polarized incident plane wave is given by Eq. (3.1),

$$E_{\mathrm{in}} = E_0 \left(\cos\varphi \hat{\boldsymbol{x}} + i \sin\varphi \hat{\boldsymbol{y}}\right) e^{-ift}. \tag{3.1}$$

Further, Eq. (3.1) is rewritten with circular basis,

$$E_{\mathrm{in}} = \frac{E_0}{\sqrt{2}} \left[\left(\cos\varphi + \sin\varphi\right) \hat{\boldsymbol{e}}_+ + \left(\sin\varphi - \sin\varphi\right) \hat{\boldsymbol{e}}_-\right] e^{-ift} e^{ikz}, \tag{3.1}$$

where $\hat{\boldsymbol{e}}_+$ and $\hat{\boldsymbol{e}}_+$ are expressed as

$$\hat{\boldsymbol{e}}_+ = \frac{1}{\sqrt{2}} \left(\hat{\boldsymbol{x}} + i\hat{\boldsymbol{y}}\right), \tag{C.1}$$

$$\hat{\boldsymbol{e}}_- = \frac{1}{\sqrt{2}} \left(\hat{\boldsymbol{x}} - i\hat{\boldsymbol{y}}\right), \tag{C.2}$$

respectively.

Torque transmitted via reflection

A left-chiral object reflects left circularly polarized light as shown in Fig. C.1. The reflected field E_{re} is left circularly polarized and, its amplitude is equal to left circular polarization (LCP) component of the incident field multiplied by the reflection coefficient r_+,

$$\boldsymbol{E}_{\mathrm{re}} = \frac{E_0}{\sqrt{2}} r_+ \left[(\sin\varphi + \sin\varphi)\, \hat{\boldsymbol{e}}_+ \right] e^{-ift} e^{-ikz}. \tag{3.1}$$

The corresponding spin angular momentum $\boldsymbol{L}_{\mathrm{re}}$ is

$$\begin{aligned} \boldsymbol{L}_{\mathrm{re}} &= \frac{\varepsilon}{2if} \boldsymbol{E}^*_{\mathrm{re}} \times \boldsymbol{E}_{\mathrm{re}} \\ &= \frac{\varepsilon}{2if} \frac{E_0^2}{2} r_+^2 \left(\sin\varphi + \cos\varphi\right)^2 \hat{\boldsymbol{e}}^*_+ \times \hat{\boldsymbol{e}}_+ \\ &= -\frac{\varepsilon E_0^2}{4f} R^+ \left[(1 + \sin 2\varphi)\, \hat{\boldsymbol{z}} \right], \end{aligned} \tag{C.3}$$

where $R^+ = r_+^2$ is the reflectance of the LCP component of the incident field.

Torque transmitted via transmission

Let us consider the transmitted light E_{tr} in the same way as in an NLC droplet. To describe the dependence of θ, Eq. (3.11) is used,

$$\boldsymbol{E}_{\mathrm{in}} = E_0 e^{-ift} \left[(\cos\theta\cos\varphi - i\sin\theta\sin\varphi)\, \hat{\boldsymbol{x}} + (\sin\theta\cos\varphi + i\cos\theta\sin\varphi)\, \hat{\boldsymbol{y}} \right]. \tag{3.11}$$

In a left chiral object, right circularly polarized (RCP) light is transmitted through the object and LCP light is partly reflected due to the selective Bragg reflection. Using circular basis ($\hat{\boldsymbol{e}}_+$, $\hat{\boldsymbol{e}}_-$), the transmitted light E_{tr} is expressed as,

$$\begin{aligned} \boldsymbol{E}_{\mathrm{tr}} =& \frac{E_0}{\sqrt{2}} e^{-ift} \left(t_+ \hat{\boldsymbol{e}}_+ \left[(\cos\varphi\cos\theta - i\sin\varphi\sin\theta) - i\left(\cos\varphi\sin\theta + i\sin\varphi\cos\theta\right) \right] \right. \\ & \left. + \hat{\boldsymbol{e}}_- \left[(\cos\varphi\cos\theta - i\sin\varphi\sin\theta) + i\left(\cos\varphi\sin\theta + i\sin\varphi\cos\theta\right) \right] \right), \end{aligned} \tag{C.4}$$

where t^+ is Fresnel coefficient for LCP light. The transmitted field $\boldsymbol{E}$ is expressed in the cartesian basis,

$$\begin{aligned}\boldsymbol{E}_{\mathrm{tr}} = \frac{E_0}{2} e^{-ift} \Big\{ & \hat{\boldsymbol{x}} \big[t_+(\cos\theta\cos\varphi - i\sin\theta\sin\varphi) - it_+(\sin\theta\cos\varphi - i\cos\theta\sin\varphi) \\ & + (\cos\theta\cos\varphi - i\sin\theta\sin\varphi) + i(\sin\theta\cos\varphi - i\cos\theta\sin\varphi) \big] \\ & + \hat{\boldsymbol{y}} \big[t_+(\sin\theta\cos\varphi + i\cos\theta\sin\varphi) + it_+(\cos\theta\cos\varphi - i\sin\theta\sin\varphi) \\ & + (\sin\theta\cos\varphi + i\cos\theta\sin\varphi) - i(\cos\theta\cos\varphi - i\sin\theta\sin\varphi) \big] \Big\}. \end{aligned} \tag{C.5}$$

Here, we consider the birefringence. The extraordinary ray is directed along the x-axis, and the ordinary ray is directed along the y-axis. The phase shift due to passing through material of thickness d is kdn where k is the wavenumber and n is the refractive index. The transmitted field is expressed as

$$\begin{aligned}\boldsymbol{E}_{\mathrm{tr}} = \frac{E_0}{2} e^{-ift} \Big\{ & \hat{\boldsymbol{x}} e^{ikdn_{\mathrm{e}}} \big[(t_+ + 1)(\cos\theta\cos\varphi - i\sin\theta\sin\varphi) \\ & - i(t_+ - 1)(\sin\theta\cos\varphi - i\cos\theta\sin\varphi) \big] \\ & + \hat{\boldsymbol{y}} e^{ikdn_{\mathrm{o}}} \big[(t_+ + 1)(\sin\theta\cos\varphi - i\cos\theta\sin\varphi) \\ & + i(t_+ - 1)(\cos\theta\cos\varphi - i\sin\theta\sin\varphi) \big] \Big\}. \end{aligned} \tag{C.6}$$

The corresponding spin angular momentum $\boldsymbol{L}_{\mathrm{tr}}$ is

$$\begin{aligned}\boldsymbol{L}_{\mathrm{re}} &= \frac{\varepsilon}{2if} \boldsymbol{E}_{\mathrm{tr}}^* \times \boldsymbol{E}_{\mathrm{tr}} \\ &= \frac{\varepsilon E_0^2}{4f} \left[\left(T^+ - 1\right)\cos\Delta + \left(T^+ + 1\right)\cos\Delta\sin 2\varphi - 2t^+\sin\Delta\cos 2\varphi\sin\theta \right] \hat{\boldsymbol{z}}, \end{aligned} \tag{C.7}$$

where $\Delta = kd(n_e - n_o)$ is the optical retardance and $t_+^2 = T^+ = 1 - R^+$ is the transmittance of the material for LCP light.

Total reaction torque

Let us consider the density of the total reaction torque. The density of angular momentum for the incident field is given by Eq. (3.9),

$$\boldsymbol{L}_{\mathrm{in}} = \frac{\varepsilon E_0^2}{2f} \sin 2\varphi \hat{\boldsymbol{z}}. \tag{3.9}$$

The density of the total reaction torque $\Delta \boldsymbol{L}$ is expressed as

$$\begin{aligned}\Delta \boldsymbol{L} &= \boldsymbol{L}_{\rm in} - (\boldsymbol{L}_{\rm in} + \boldsymbol{L}_{\rm tr}) \\ &= \frac{\varepsilon E_0^2}{4f}\left[2\sin 2\varphi + R^+(1+\sin 2\varphi) - (T^+ - 1)\cos\Delta\right. \\ &\left. -(T^+ + 1)\cos\Delta\sin 2\varphi + 2t^+\sin\Delta\cos 2\varphi\sin 2\theta\right]\hat{\boldsymbol{z}} \end{aligned} \tag{C.8}$$

The torque exerted per unit time Δt on the sphere Γ is calculated by integrating on a volume element $Sc\Delta t$,

$$\begin{aligned}\boldsymbol{\Gamma} &= \frac{Sc\Delta t\Delta \boldsymbol{L}}{\Delta t} = Sc\Delta \boldsymbol{L} \\ &= \frac{P}{f}\left\{\frac{R^+}{2}(1+\cos\Delta)\right. \\ &+ \sin 2\varphi\left[(1-\cos\Delta) + \frac{R^+}{2}(1+\cos\Delta)\right] \\ &\left. + t_+\sin\Delta\cos 2\varphi\sin 2\theta\right\}\hat{\boldsymbol{z}}, \end{aligned} \tag{C.9}$$

where $P = \frac{c}{2}\varepsilon E_0^2 S$ [37]. Eq.(C.9) consist of three contributions. The first and second terms induce continuous rotation. The first term relates only to the reflectance of the particles, whereas the second term depends on the ellipticity of the light φ. The third term is alignment torque, which makes the object orient along the optical axis of the object with the major axis of the polarization ellipse. The total torque becomes maximum when $\varphi = \frac{\pi}{4}$.

Rotation frequency ν

A chiral particle continuously rotates under the irradiation of circularly polarized light ($\varphi = \frac{\pi}{4}$). At a steady state, the optical torque balances the viscous torque,

$$\begin{aligned}8\pi\eta a^3\omega = \frac{P}{f}\left\{\frac{R^+}{2}(1+\cos\Delta) + \sin 2\varphi\left[(1-\cos\Delta) + \frac{R^+}{2}(1+\cos\Delta)\right]\right. \\ \left. + t_+\sin\Delta\cos 2\varphi\sin 2\theta\right\}, \end{aligned} \tag{C.10}$$

where $\omega = 2\pi\nu$ is the angular frequency, η is the viscosity of a surrounding fluid and a is the radius of the particle. Since $\omega = \frac{d\theta}{dt}$, Eq. (C.10) is a differential equation for

the variable θ as the following form:

$$\dot{\theta} = A + B\sin 2\theta. \tag{C.11}$$

In this case, ω is expressed as [9, 37]

$$\omega = \mathrm{Re}\left[\sqrt{A^2 - B^2}\right]. \tag{C.12}$$

In the case of Eq. (C.10),

$$A = \frac{P}{8\pi f\eta a^3}\left\{\sin 2\varphi\left[\left(1+\frac{R^+}{2}\right) - \left(1-\frac{R^+}{2}\right)\cos\Delta + \frac{R^+}{2}\left(1+\cos\Delta\right)\right]\right\} \tag{C.13}$$

$$B = \frac{P}{8\pi f\eta a^3}\left(t_+ \sin\Delta\cos 2\varphi\right) \tag{C.14}$$

By substituting A and B into Eq. (C.12), ν is given as

$$\nu = \frac{P\lambda}{4\pi^3 c\eta d^3}\mathrm{Re}\left[\left\{\sin^2 2\phi\left[\left(1+\frac{R}{2}\right) - \left(1-\frac{R}{2}\right)\cos\Delta\right]^2 + R(1+\cos\Delta)\sin 2\phi \right.\right.$$
$$\left.\left.\times\left[\left(1+\frac{R}{2}\right) - \left(1-\frac{R}{2}\right)\cos\Delta\right] + \frac{R^2}{4}\left(1+\cos\Delta\right)^2 - (1-R)\cos^2 2\phi\sin^2\Delta\right\}^{\frac{1}{2}}\right], \tag{C.15}$$

where d is the diameter of the particle.

D Estimation of effective viscosity η_{eff} from Brownian motion near the cell bottom

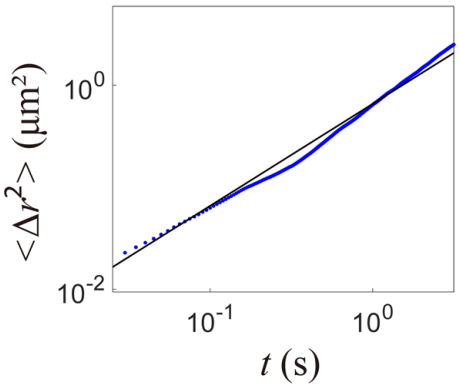

Figure D.1. Dependence of mean square displacement $\langle \Delta r^2 \rangle$ of a tracer particle on the elapsed time t in the aqueous glycerol solution of $C_{\mathrm{m}} = 50$ wt%. Blue dots: the measured values. Solid line: the best-fitted lines with Eq. (D.1).

We measured the Brownian motion of a tracer silica particle (radius $a = 500$ nm, Micromod) near the cell bottom. The mean squared displacement Δr^2 (MSD) was calculated from the two-dimensional trajectory of the particle as shown in Fig. D.1. The MSD for a freely diffusing particle is written as,

$$\langle \Delta r(t)^2 \rangle = 4Dt, \tag{D.1}$$

where D is the diffusion constant and t is the elapsed time. The estimated value of D is 8.9×10^{-2} μm^2/s at $C_{\mathrm{m}} = 60$ wt%. The effective viscosity η_{eff} is calculated by Stokes-Einstein equation as,

$$\eta_{\mathrm{eff}} = \frac{k_{\mathrm{B}}T}{6\pi Da}, \tag{D.2}$$

where k_{B} is the Boltzmann constant, T is the absolute temperature and a is the particle radius. The estimated value of η_{eff} is larger than the literature value η_0 due to the particle-wall interaction. The values of η_0 and η_{eff} are listed in Table D.1. The flow velocity measured by PIV was corrected by considering the reduction in velocity due to the wall effect.

C_{m} (wt%)	η_0 (mPa·s) at $T = 25°\mathrm{C}$ [83]	η_{eff} (mPa·s)
0	0.89	0.92
20	1.5	1.8
40	3.1	3.5
50	5.0	6.2
60	8.8	9.8

Table D.1. η_0 and η_{eff} at various C_{m}.

E Estimation of rheological parameters: η_0, η_∞ and τ

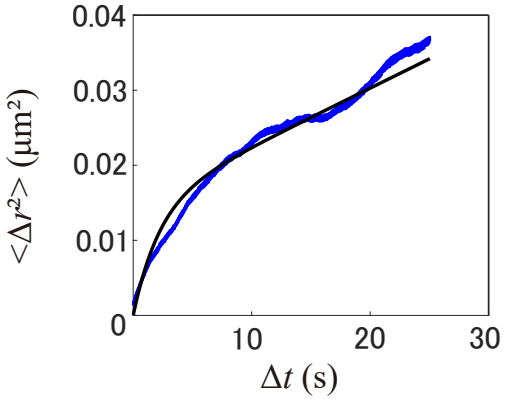

Figure E.1. Mean-squared displacement $\langle \Delta r^2 \rangle$ of a silica particle of 500 nm diameter in a 1 wt% PEO solution. The solid line was best-fitted curve from Eq. (E.1) where $\eta_\infty = 0.09$ Pa·s, $\eta_0 = 0.89$ Pa·s and $\tau = 20$ s.

We need rheological parameters (η_0, η_∞ and τ) of viscoelastic solutions to estimate ω of the Janus particle. The rheological parameters are derived from two-dimensional mean-squared displacement $\langle \Delta r(t)^2 \rangle$ (MSD) of a passive particle because the MSD is expressed as

$$\langle \Delta r(t)^2 \rangle = 4D_t^0 \left[t + \left(1 - \frac{\eta_\infty}{\eta_0} \right) \tau \left(1 - e^{\frac{t}{\lambda}} \right) \right], \tag{E.1}$$

where $D_t^0 = \frac{k_{\mathrm{B}}T}{6\pi a \eta_0}$ and $\lambda = \frac{\eta_\infty}{\eta_0}\tau$. Brownian motion of a silica particle of 500 nm

diameter dispersed in PEO solutions was observed, and its MDS were fitted by Eq. (E.1), as shown in Fig. E.1. The rheological parameters of solutions with PEO concentration c_{m} are summrized in Table E.2.

c_{m} (wt%)	η_∞ (Pa·s)	η_0 (Pa·s)	τ (s)
1	0.045	0.18	57.8
0.75	0.025	0.072	7.3
0.5	0.015	0.046	3.3
0.25	0.014	0.031	2.5

Table E.2. η_0, η_∞ and τ at various c_{m}.

F Collective motion of Janus particles

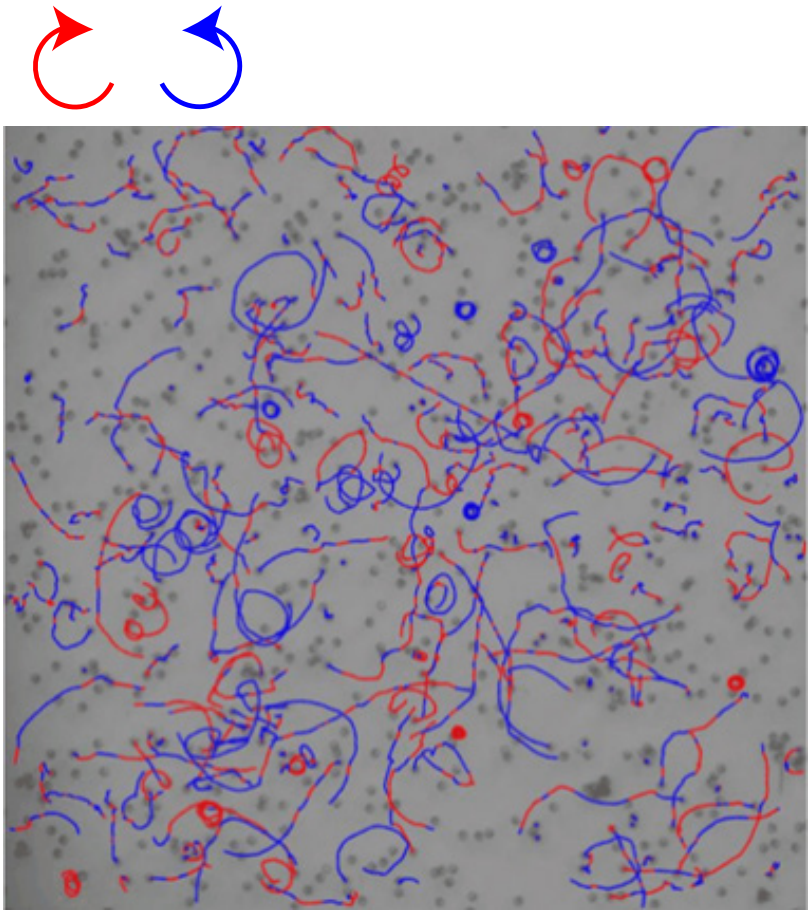

Figure F.1. The image of Janus particles in the 1 wt% PEO solution. The solid lines represent the trajectories of the Janus particles. Red and blue lines represent clockwise and counterclockwise rotation, respectively.

.

The motion of a single Janus particle in viscoelastic fluids was investigated, and the particle with v above a threshold velocity exhibited a circular orbit. This effect of viscoelastic fluids is expected to affect the collective motion of Janus particles. Here, the collective motion of Janus particles with circular orbits was observed.

Systems composed of active particles usually exhibit spontaneous dynamic phase

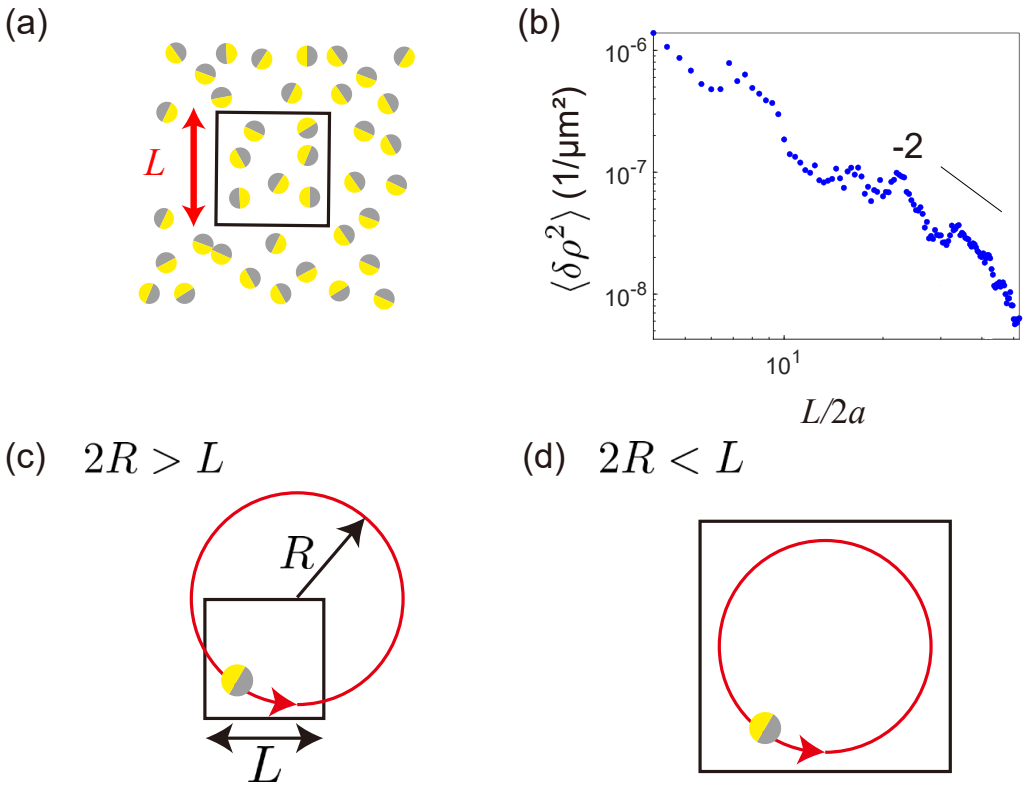

Figure F.2. Density fluctuations of Janus particles $\langle \delta\rho^2 \rangle$. (a) The particle number density $\rho(L)$ in a region with the window size L. (b) Variation of $\langle \delta\rho^2 \rangle$ with normalized widow size $L/2a$. The solid line is proportional to L^{-2}. (c, d) Relationship between $2R$ and L for $2R > L$ (c) and $2R < L$ (d). The red line represents a circular orbit of a Janus particle. The square denotes the window for calculating $\rho(L)$

separation and giant number fluctuation [110]. In contrast to many active particles, rotating active particle, known as chiral active matter [111], exhibits the suppression of the density fluctuation at long-wavelength [112]. Such a system called disordered hyperuniform state, which is the state with vanishing long-wavelength density fluctuations similar to perfect crystals but without long-range order [112]. The disordered hyperuniform state is reported in marine algae systems where they rotate with roughly the same radius in the same direction [116]. In contrast, the rotating direction and radius of the Janus particles were different for each particle as shown in Fig. F.1. The density fluctuation of the Janus particles $\langle \delta\rho^2 \rangle$ was calculated to investigate whether a hyperuniform state appears. The density fluctuation $\langle \delta\rho^2 \rangle$ is defined as

$\langle \delta\rho(L)^2 \rangle = \langle \rho(L)^2 \rangle - \langle \rho(L) \rangle^2$, where $\rho(L)$ is the particle number density in a region with the window size L, as shown in Fig. F.2(a). In small L, $\langle \delta\rho^2 \rangle \propto L^{-2}$, as shown in Fig. F.2(b). A variety of disordered system such as gases and liquids exhibit the same behavior $\langle \delta\rho^2 \rangle \propto L^{-2}$ [117]. On the other hand, in Fig. F.2(b), the slope in large L became smaller than that in small L. In the hyperuniform state, theoretical prediction gives $\langle \delta\rho^2 \rangle \propto L^{-3}$ at large L where the direction and the mean radius of each rotation are the same [112]. In our case, suppression of density fluctuations was observed at large L, but this is not $\langle \delta\rho^2 \rangle \propto L^{-3}$. A possible reason for the difference is that the radius of rotation were different for each particle.

Although our system does not show $\langle \delta\rho^2 \rangle \propto L^{-3}$, suppression of density fluctuations was observed. Two characteristic lengths are important for $\delta\rho$: the rotation radius R and window size L. In case of $2R > L$, the particle enters or leaves the window, causing ρ to vary with time as shown in Fig. F.2(c). In case of $2R < L$, the particle no longer escapes the window and the density variation is suppressed as shown in Fig. F.2(d). Change in slope in Fig. F.2(b) occurred at $L/2a \sim 40$ corresponding to $L \sim 200$ µm. In the single particle system, $2R$ was approximately 300 µm. This is roughly consistent, but the critical L is slightly smaller than $2R$ of the single particle system. Although particle-particle interactions may cause changes in R, the detailed reason is not clear at this stage.

References

[1] P. G. De Gennes, Science **256**, 495 (1992).

[2] L. S. Hirst, *Fundamentals of soft matter science* (CRC press, 2019).

[3] I. Teraoka, *Polymer Solutions: An Introduction to Physical Properties* (Wiley-Interscience, 2002).

[4] E. M. Furst and T. M. Squires, *Microrheology* (Oxford University Press, 2017).

[5] S. Saad and G. Natale, Soft Matter **15**, 9909 (2019).

[6] K. Nishizawa, K. Fujiwara, M. Ikenaga, N. Nakajo, M. Yanagisawa, and D. Mizuno, Sci. Rep. **7**, 15143 (2017).

[7] S. Suda, T. Suda, T. Ohmura, and M. Ichikawa, Phys. Rev. Lett. **127**, 088005 (2021).

[8] A. Bricard, J. B. Caussin, N. Desreumaux, O. Dauchot, and D. Bartolo, Nature **503**, 95 (2013).

[9] M. E. J. Friese, T. A. Nieminen, N. R. Heckenberg, and H. Rubinsztein-Dunlop, Nature **394**, 348 (1998).

[10] A. Walther and A. H. E. Muller, Chem. Rev. **113**, 5194 (2013).

[11] Z. Izri, M. N. Van Der Linden, S. Michelin, and O. Dauchot, Phys. Rev. Lett. **113**, 248302 (2014).

[12] S. Herminghaus, C. C. Maass, C. Krüger, S. Thutupalli, L. Goehring, and C. Bahr, Soft Matter **10**, 7008 (2014).

[13] G. Quincke, Ann. Phys. **295**, 417 (1896).

[14] E. Brasselet and S. Juodkazis, J. Nonlinear Optic. Mat. **18**, 167 (2009).

[15] M. Suga, S. Suda, M. Ichikawa, and Y. Kimura, Phys. Rev. E **97**, 062703 (2018).

[16] J. R. Melcher and G. I. Taylor, Annu. Rev. Fluid Mech. **1**, 111 (1969).

[17] C. Lozano, J. R. Gomez-Solano, and C. Bechinger, Nat. Mater. **18**, 1118 (2019).

[18] J. R. Gomez-Solano, A. Blokhuis, and C. Bechinger, Phys. Rev. Lett. **116**, 138301 (2016).

[19] A. Basset, *A treatise on Hydrodynamics* (Dover, 1961).

[20] T. M. Squires and M. Z. Bazant, J. Fluid Mech. **560**, 65 (2006).

[21] T. M. Squires and M. Z. Bazant, J. Fluid Mech. **509**, 217 (2004).

[22] M. Z. Bazant, M. S. Kilic, B. D. Storey, and A. Ajdari, Adv. Colloid Interface

Sci. **152**, 48 (2009).

[23] H. A. Stone and A. D. T. Samuel, Phys. Rev. Lett. **77**, 4102 (1996).

[24] C. Cohen-Tannoudji, J. Dupont-Roc, and G. Grynberg, *Photons and atoms-introduction to quantum electrodynamics* (John Wiley and Sons, 1997).

[25] L. Han, S. Liu, P. Li, Y. Zhang, H. Cheng, and J. Zhao, Phys. Rev. A **97**, 053802 (2018).

[26] G. R. Fowles, *Introduction to modern optics* (Dover, 1989).

[27] M. G. Donato, J. Hernandez, A. Mazzulla, C. Provenzano, R. Saija, R. Sayed, S. Vasi, A. Magazzù, P. Pagliusi, and R. Bartolino, Nat. Commun. **5**, 3656 (2014).

[28] D. Konopacka-Łyskawa, Crystals **9**, 223 (2019).

[29] P. S. Drzaic, *Liquid crystal dispersions* (World Scientific, 1995).

[30] X. Wang, E. Bukusoglu, and N. L. Abbott, Chem. Mater. **29**, 53 (2017).

[31] O. D. Lavrentovich, Liq. Cryst. **24**, 117 (1998).

[32] I. H. Lin, D. S. Miller, P. J. Bertics, C. J. Murphy, J. J. de Pablo, and N. L. Abbott, Science **332**, 1297 (2011).

[33] N. Murazawa, S. Juodkazis, S. Matsuo, and H. Misawa, Small **1**, 656 (2005).

[34] E. Brasselet, N. Murazawa, S. Juodkazis, and H. Misawa, Phys. Rev. E **77**, 041704 (2008).

[35] H. G. Lee, S. Munir, and S. Y. Park, ACS Appl. Mater. Interfaces **8**, 26407 (2016).

[36] M. Mosallaeipour, Y. Hatwalne, N. V. Madhusudana, and S. Ananthamurthy, J. Mod. Opt. **57**, 395 (2010).

[37] M. G. Donato, A. Mazzulla, P. Pagliusi, A. Magazzù, R. J. Hernandez, C. Provenzano, P. G. Gucciardi, O. M. Maragò, and G. Cipparrone, Sci. Rep. **6**, 31977 (2016).

[38] P. G. de Gennes and J. Prost, *The Physics of Liquid Crystals* (Oxford University Press, 1979).

[39] J. R. Howse, R. A. L. Jones, A. J. Ryan, T. Gough, R. Vafabakhsh, and R. Golestanian, Phys. Rev. Lett. **99**, 048102 (2007).

[40] J. L. Moran and J. D. Posner, J. Fluid Mech. **680**, 31 (2011).

[41] Y. Wang, R. M. Hernandez, D. J. Bartlett, J. M. Bingham, T. R. Kline, A. Sen, and T. E. Mallouk, Langmuir **22**, 10451 (2006).

[42] G. Volpe, I. Buttinoni, D. Vogt, H. J. Kümmerer, and C. Bechinger, Soft Matter **7**, 8810 (2011).

[43] F. A. Lavergne, H. Wendehenne, T. Bäuerle, and C. Bechinger, Science **364**, 70 (2019).

[44] T. Araki and A. Maciołek, Soft matter **15**, 5243 (2019).

[45] S. Gangwal, O. J. Cayre, M. Z. Bazant, and O. D. Velev, Phys. Rev. Lett. **100**, 058302 (2008).

[46] A. Boymelgreen, G. Yossifon, and T. Miloh, Langmuir **32**, 9540 (2016).

[47] K. Dholakia, P. Reece, and M. Gu, Chem. Soc. Rev. **37**, 42 (2008).

[48] Z. Zhang, X. Wang, J. Liu, C. Dai, and Y. Sun, Annu. Rev. Control Robot. Auton. Syst. **2**, 181 (2019).

[49] J. R. Moffitt, Y. R. Chemla, S. B. Smith, and C. Bustamante, Annu. Rev. Biochem. **77**, 205 (2008).

[50] D. G. Grier, Nature **424**, 810 (2003).

[51] S. Juodkazis, M. Shikata, T. Takahashi, S. Matsuo, and H. Misawa, Jpn. J. Appl. Phys. **38**, L518 (1999).

[52] C. Manzo, D. Paparo, L. Marrucci, and I. Janossy, Phys. Rev. E **73**, 051707 (2006).

[53] O. O. Prishchepa, V. Y. Zyryanov, A. P. Gardymova, and V. F. Shabanov, Mol. Cryst. and Liq. Cryst. **489**, 84 (2008).

[54] Y. Zhou, E. Bukusoglu, J. A. Martínez-González, M. Rahimi, T. F. Roberts, R. Zhang, X. Wang, N. L. Abbott, and J. J. De Pablo, ACS Nano **10**, 6484 (2016).

[55] A. Y. Savchenko, N. V. Tabiryan, and B. Y. Zeldovich, Phys. Rev. E **56**, 4773 (1997).

[56] S. Juodkazis, S. Matsuo, N. Murazawa, I. Hasegawa, and H. Misawa, Appl. Phys. Lett. **82**, 4657 (2003).

[57] T. A. Wood, H. F. Gleeson, M. R. Dickinson, and A. J. Wright, Appl. Phys. Lett. **84**, 4292 (2004).

[58] H. F. Gleeson, T. A. Wood, and M. Dickinson, Philos. Trans. A Math. Phys. Eng. Sci. **364**, 2789 (2006).

[59] G. Tkachenko, M. Rafayelyan, and E. Brasselet, Phys. Rev. A **95**, 053839 (2017).

[60] Y. Yang, P. D. Brimicombe, N. W. Roberts, M. R. Dickinson, M. Osipov, and

H. F. Gleeson, Opt. Express **16**, 6877 (2008).

[61] J. K. Gupta, S. Sivakumar, F. Caruso, and N. L. Abbott, Angew. Chem. Int. Ed. **48**, 1652 (2009).

[62] A. Ashkin, Phys. Rev. Lett. **24**, 156 (1970).

[63] A. Ashkin, J. M. Dziedzic, J. E. Bjorkholm, and S. Chu, Opt. Lett. **11**, 288 (1986).

[64] J. Happel and H. Brenner, *Low Reynolds number hydrodynamics: with special applications to particulate media* (Springer, 1983).

[65] W. Martienssen and H. Warlimont, *Springer handbook of condensed matter and materials data* (Springer, 2006).

[66] E. Santamato, M. Romagnoli, M. Settembre, B. Diano, and Y. R. Shen, Phys. Rev. Lett. **61**, 113 (1988).

[67] V. Tkachenko, G. Abbate, A. Marino, F. Vita, M. Giocondo, A. Mazzulla, F. Ciuchi, and L. D. Stefano, Mol. Cryst. Liq. Cryst. **454**, 263 (2006).

[68] M. N. Krakhalev, V. Y. Rudyak, O. O. Prishchepa, A. P. Gardymova, A. V. Emelyanenko, J. H. Liu, and V. Y. Zyryanov, Soft Matter **15**, 5554 (2019).

[69] L. Tortora and O. D. Lavrentovich, Proc. Natl. Acad. Sci. U. S. A. **108**, 5163 (2011).

[70] E. Lauga and T. R. Powers, Rep. Prog. Phys. **72**, 096601 (2009).

[71] E. Lauga, Annu. Rev. Fluid Mech. **48**, 105 (2016).

[72] P. Sajeesh and A. K. Sen, Microfluid. Nanofluidics **17**, 1 (2014).

[73] J. S. Park and H. I. Jung, Anal. Chem. **81**, 8280 (2009).

[74] N. T. Nguyen and Z. Wu, J. Micromech. Microeng. **15**, R1 (2004).

[75] J. Elgeti, R. G. Winkler, and G. Gompper, Rep. Prog. Phys. **78**, 056601 (2015).

[76] L. Lanotte, J. Mauer, S. Mendez, D. A. Fedosov, J. M. Fromental, V. Claveria, F. Nicoud, G. Gompper, and M. Abkarian, Proc. Natl. Acad. Sci. U. S. A. **113**, 13289 (2016).

[77] J. E. Curtis, B. A. Koss, and D. G. Grier, Opt. Commun. **207**, 169 (2002).

[78] M. Padgett and R. Di Leonardo, Lab. Chip **11**, 1196 (2011).

[79] P. H. Jones, O. M. Maragò, and G. Volpe, *Optical tweezers: Principles and applications* (Cambridge University Press, 2015).

[80] W. Thielicke and R. Sonntag, J. Open Res. Softw. **9** (2021).

[81] L. D. Landau and E. M. Lifshitz, *Fluid Mechanics* (1959).

[82] I. Pala Rosas, J. L. Contreras, J. Salmones, C. Tapia, B. Zeifert, J. Navarrete, T. Vázquez, and D. C. García, Catalysts **7**, 73 (2017).

[83] N. S. Cheng, Ind. Eng. Chem. Res. **47**, 3285 (2008).

[84] J. Yoshioka and F. Araoka, Sci. Rep. **10**, 17226 (2020).

[85] E. Guyon, J. P. Hulin, L. Petit, and C. D. Mitescu, *Physical hydrodynamics* (Oxford, 2015).

[86] P. Joseph, C. Cottin-Bizonne, J. M. Benoit, C. Ybert, C. Journet, P. Tabeling, and L. Bocquet, Phys. Rev. Lett. **97**, 156104 (2006).

[87] K. Nishiyama, S. Bono, Y. Maruyama, and Y. Tabe, J. Phys. Soc. Jpn. **88**, 063601 (2019).

[88] R. Tuinier and T. Taniguchi, J. Phys. Condens. Matter **17**, L9 (2004).

[89] S. G. Hatzikiriakos, Prog. Polym. Sci. **37**, 624 (2012).

[90] J. Koplik and J. R. Banavar, Phys. Rev. Lett. **96**, 044505 (2006).

[91] P. Poulin, H. Stark, T. C. Lubensky, and D. A. Weitz, Science **275**, 1770 (1997).

[92] R. Zibaei, M. S. Zakerhamidi, S. Korram, and A. Ranjkesh, J. Mater. Chem. C **9**, 14908 (2021).

[93] S. Granick, Y. Zhu, and H. Lee, Nat. Mater. **2**, 221 (2003).

[94] B. Weber, Y. Nagata, S. Ketzetzi, F. Tang, W. J. Smit, H. J. Bakker, E. H. G. Backus, M. Bonn, and D. Bonn, J. Phys. Chem. Lett. **9**, 2838 (2018).

[95] Z. Wang, Q. Xu, L. Wang, L. Heng, and L. Jiang, J. Mater. Chem. A **7**, 18510 (2019).

[96] T. Amann and A. Kailer, Tribol. Lett. **37**, 343 (2010).

[97] B. K. Gale, A. R. Jafek, C. J. Lambert, B. L. Goenner, H. Moghimifam, U. C. Nze, and S. K. Kamarapu, Inventions **3**, 60 (2018).

[98] K. Ward and Z. H. Fan, J. Micromech. Microeng. **25**, 094001 (2015).

[99] C. Bechinger, R. Di Leonardo, H. Löwen, C. Reichhardt, G. Volpe, and G. Volpe, Rev. Mod. Phys. **88**, 045006 (2016).

[100] G. Li, E. Lauga, and A. M. Ardekani, J Nonnewton Fluid Mech **297**, 104655 (2021).

[101] D. Yuan, Q. Zhao, S. Yan, S.-Y. Tang, G. Alici, J. Zhang, and W. Li, Lab Chip **18**, 551 (2018).

[102] A. Patteson, A. Gopinath, M. Goulian, and P. Arratia, Sci. Rep. **5**, 15761 (2015).

[103] W. Wang, X. Lv, J. L. Moran, S. Duan, and C. Zhou, Soft Matter **16**, 3846

(2020).

[104] N. Narinder, C. Bechinger, and J. R. Gomez-Solano, Phys. Rev. Lett. **121**, 078003 (2018).

[105] I. Buttinoni, G. Volpe, F. Kümmel, G. Volpe, and C. Bechinger, J. Phys.: Condens. Matter **24**, 284129 (2012).

[106] G. D. Moon, T. I. Lee, B. Kim, G. Chae, J. Kim, S. Kim, J. M. Myoung, and U. Jeong, ACS nano **5**, 8600 (2011).

[107] S. Jiang, Q. Chen, M. Tripathy, E. Luijten, K. S. Schweizer, and S. Granick, Adv. Mater. **22**, 1060 (2010).

[108] T. Ohta and T. Ohkuma, Phys. Rev. Lett. **102**, 154101 (2009).

[109] P. C. Sousa, E. J. Vega, R. G. Sousa, J. M. Montanero, and M. A. Alves, Rheol. Acta. **56**, 11 (2017).

[110] M. C. Marchetti, J. F. Joanny, S. Ramaswamy, T. B. Liverpool, J. Prost, M. Rao, and R. A. Simha, Rev. Mod. Phys. **85**, 1143 (2013).

[111] B. Liebchen and D. Levis, Europhys. Lett. **139**, 67001 (2022).

[112] Q. L. Lei, M. P. Ciamarra, and R. Ni, Sci. Adv. **5**, eaau7423 (2019).

[113] A. A. Hyman, C. A. Weber, and F. Jülicher, Annu. Rev. Cell Dev. Biol. **30**, 39 (2014).

[114] S. M. Barnett and L. Allen, Opt. Commun. **110**, 670 (1994).

[115] A. Yariv and P. Yeh, *Optical waves in crystal propagation and control of laser radiation* (Wiley-Interscience, 1983).

[116] M. Huang, W. Hu, S. Yang, Q. X. Liu, and H. P. Zhang, Proc. Natl. Acad. Sci. U. S. A. **118**, e2100493118 (2021).

[117] S. Torquato, Proc. Natl. Acad. Sci. U. S. A. **118**, e2107276118 (2021).

Acknoeledgements

I would like to express my deepest gratitude to my supervisor, Prof. Yasuyuki Kimura. He warmly welcomed me to his laboratory. His considerable encouragement helped me to pursue my interest. His insightful comments from a broader perspective lead to fascinating results in my research. This thesis would not have been possible without his tremendous support.

I am greatly indebted to Prof. Shio Inagaki not only for warm support and valuable comments but also for inviting me to her English class. I would like to thank Dr. Fumiaki Kobayashi for useful advice regarding the experimental system.

I would like to offer my special thanks to my assistant supervisor, Prof. Yusuke Maeda, for reviewing my thesis and teaching me professional attitude toward research. I would like to express my special thanks to Prof. Jun-ichi Fukuda for reviewing my thesis and incisive comments on liquid crystal droplets. I would like to express my special thanks to Prof. Daisuke Mizuno for reviewing my thesis and for insightful comments on viscoelastic property of polymer solutions.

I am thankful to Prof. Yasutaka Iwashita for teaching me the fabrication of Janus particles, and to Prof. Yuki Uematsu for incisive comments on my research and warm welcome. I would like to express my appreciation to Prof. Takashi Taniguchi for his valuable comments on my research. I am thankful to all the past and current members of Kimura Laboratory for sharing wonderful time with me. I am grateful to my former colleague for giving me a push in the back.

Lastly, I would like to express my gratitude to my family for supporting and encouraging me throughout my life.

Publication list

Related papers

Papers listed below include the main contents of this thesis.

- Keita Saito and Yasuyuki Kimura, Optically driven liquid crystal droplet rotatort, *Scientific Reports* **12**, 16623 (2022).
- Keita Saito and Yasuyuki Kimura, Slip of a liquid crystal droplet rotator in viscous fluids, *Soft matter*, published online (2024).
- Keita Saito, Yasutaka Iwashita and Yasuyuki Kimura, Rotational motion of electrically driven Janus particles in polymer solution, to be submitted.

Reference paper

- Keita Saito, Shogo Okubo and Yasuyuki Kimura, Change in collective motion of colloidal particles driven by an optical vortex with driving force and spatial confinement, *Soft matter* **14**, 6037 (2018).